Study on *pep* and CNO solar neutrino interaction rates in Borexino

Alvaro Eugenio Chavarria

A Dissertation
Presented to the Faculty
of Princeton University
in Candidacy for the Degree
of Doctor of Philosophy

Recommended for Acceptance
by the Department of
Physics

Advisor: Cristiano Galbiati

September 2012

Abstract

We observed, for the first time, solar neutrinos in the 1.0–1.5 MeV energy range. We determined the rate of *pep* solar neutrino interactions in Borexino to be $3.28\pm0.56_{\mathrm{stat}}\pm 0.26_{\mathrm{syst}}$ $\mathrm{day}^{-1}(100\,\mathrm{ton})^{-1}$. Assuming the *pep* neutrino flux predicted by the Standard Solar Model, we obtained a constraint on the CNO solar neutrino interaction rate of $<8.3\,\mathrm{day}^{-1}(100\,\mathrm{ton})^{-1}$ (95% C.L.). The absence of the solar neutrino signal is disfavored at 99.99997% C.L., while the absence of the *pep* neutrino signal is disfavored at 98% C.L. The necessary sensitivity was achieved due to the extremely low levels of radioactive contamination in Borexino and by adopting data analysis techniques for the rejection of cosmogenic ^{11}C, the dominant background in the 1–2 MeV region. Assuming the LMA-MSW solution to solar neutrino oscillations, these values correspond to solar neutrino fluxes of $(1.7\pm0.3)\times10^{8}\,\mathrm{cm}^{-2}\mathrm{s}^{-1}$ and $<7.9\times10^{8}\,\mathrm{cm}^{-2}\mathrm{s}^{-1}$ (95% C.L.), respectively, in agreement with both the High and Low Metallicity Standard Solar Models. These results represent the first direct evidence of the *pep* neutrino signal and the strongest constraint of the CNO solar neutrino flux to date [1].

“We are damned and we are dead
all god’s children to be sent
to our perfect place in the Sun
and in the dirt.” [2]

Contents

Chapter 1

Introduction

This could be called “normal science” [3] – a failure in the Popperian sense: this thesis falsifies nothing! I wanted a revolution, to encounter the unexpected, perhaps an anomaly in neutrino oscillations, or the flux of a yet unknown particle, maybe even electron decay. Alas, I got yet another positive instance for the success of science.

This is a first-hand account of the human struggle to see the Sun against the glare of dirt. I present one of the analyses considered for the publication “First Evidence of *pep* solar neutrinos by Direct Detection in Borexino” [1]. Further details on the other analysis and the final, published result can be found in [4, 5]. All results are in agreement.

Although every datum necessary to reach the conclusions is given in the thesis (i.e. it is self-contained), I have attempted to stay strictly on-topic and much of the behind-the-scenes effort to lead to our exquisite understanding of the detector has been omitted. Ample documentation exists on these matters in the form of internal documents, presentations, theses and publications. I have provided detailed and specific references in every case, and I have assured that every unpublished cited document can be found in the Borexino website [6].

Chapter 2

Solar neutrinos

It was until the beginning of the 20th century, with the advent of relativity, that a method of solar energy production, consistent with the billion-year timescale of geological processes and biological evolution[1], was proposed [7]. This method relies on the 26.7 MeV of energy released[2] by the fusion of four protons into a helium nucleus:

$$4\,p \longrightarrow {}^{4}\mathrm{He} + 2\,e^{+} + 2\,\nu_e \tag{2.1}$$

Considering that hydrogen is the main component of the Sun, and the solar parameters given in Table 2.1, we can see that under such process there is enough energy to sustain the star for $>10^9$ y. This also implies that solar fusion is a extremely slow process, where the mean life of a proton in the Sun is $\sim 10^{10}$ y. This is because fusion occurs by the low-probability process of quantum tunneling of keV-scale protons (Table 2.1) through the ~550 keV Coulomb barrier between them [8].

It has been observed [12] (and it is a fundamental part of the Standard Model of particle physics [13]) that transmutations between protons and neutrons are always

---

[1] The half-lives of the primordial isotopes of natural radioactivity (Section 5.1) are also suggestive of such timescale.

[2] This is approximately the mass difference between four ^{1}H atoms and one ^{4}He atom.

Solar parameter	Value
Luminosity ($L_\odot$)	3.8418×10^{26} W
	2.3977×10^{39} MeV/sec
Radius ($R_\odot$)	6.9598×10^{10} cm
Mass ($M_\odot$)	1.9884×10^{33} g
Core temperature	$\sim 1.55 \times 10^{7}$ K
	~ 1.34 keV
Core density	~ 153 g/cm^3
Surface heavy element to hydrogen ratio (Z/X)	0.0229 (GS98)
	0.0178 (AGSS09)
Mean distance to Earth (AU)	1.49598×10^{13} cm
Solar constant ($K_\odot = L_\odot/4\pi(\mathrm{AU})^2$)	8.5339×10^{11} MeV/cm^2/sec

Table 2.1: Relevant solar parameters of the Sun as well as the Sun-Earth system. The solar constant is defined here as the mean solar photon flux on Earth. Values taken from [8–10]. This is Table 1.1 in [11].

associated with the emission or absorption of neutrinos (νs). Therefore, for every four-proton fusion (Equation 2.1), two νs are produced.

It is clear from Equation 2.1 and charge conservation that neutrinos are neutral (hence, their name). As such, they do not interact with electromagnetic fields and can only lose energy through "weak" nuclear interactions. These interactions can be either "charged-current (CC)," where transmutations occur (e.g. Equation 2.1 and radioactive β decay), or "neutral-current (NC)," where energy is transferred to another particle without changing its physical nature. The ν interaction probability is so small that the mean-path of a solar ν in lead is ~1 light-year. Therefore, solar νs will travel directly from their production point in the Sun to (and through) the Earth. Nevertheless, due to the large flux of solar neutrinos (Table 2.2), some will interact in a detector on Earth, leading to a particle signal that encodes key information about the fusion process in the Sun and the properties of neutrinos as they travel through matter (Section 2.2.1).

2.1 The Standard Solar Model

Figures 2.1 and 2.2 show the details of the sequence of nuclear processes that can happen in the Sun to fuse four protons into a ^{4}He nucleus (Equation 2.1). The energy spectra of the produced νs is shown in Figure 2.3.

To estimate the relative probability of the different processes and, consequently, predict the fluxes of the different solar νs (Table 2.2), we rely on the Standard Solar Model (SSM) (Chapter 4 of [14]).

The rate of a particular nuclear reaction depends on: i) the number densities of the reactants, ii) the kinetic energy of the reactants, and iii) the probability for their interaction (nuclear cross-section) at those energies. The first two components are determined by the density and temperature of the Sun, while the reaction cross-sections are obtained from a combination of laboratory experiments and nuclear theory.

The SSM is a computer simulation that solves for the spatial profiles of the temperature and density of the Sun as a function of time, under the following assumptions and constraints:

- The Sun is in hydrostatic equilibrium: the radiative and particle pressures exactly balance gravity.
- The equation of state of the solar plasma determines the temperature and density from the radiative and particle pressures.
- The energy is produced by nuclear fusion processes (Figures 2.1 and 2.2), and flows through the solar plasma by photon transport and convection.
- The Sun was chemically homogeneous when it arrived at the main sequence (i.e. the beginning of the simulation).
- The local element abundances change only by nuclear reactions i.e. diffusion is not considered. This also implies that the abundances of elements at least

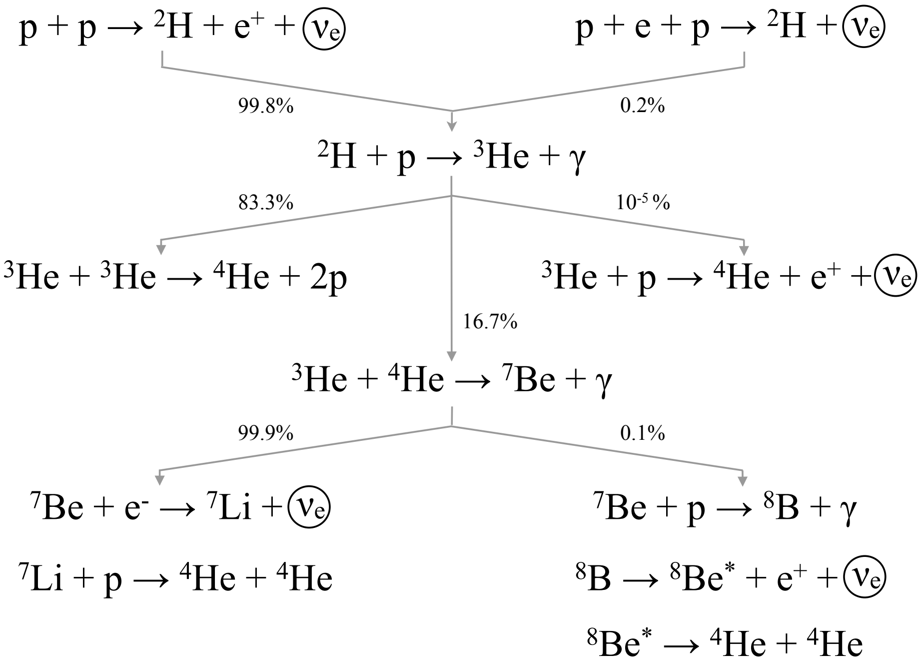

Figure 2.1: The *p-p* fusion chain, responsible for >99% of the energy produced in the Sun. This is Figure 1.1 in [11].

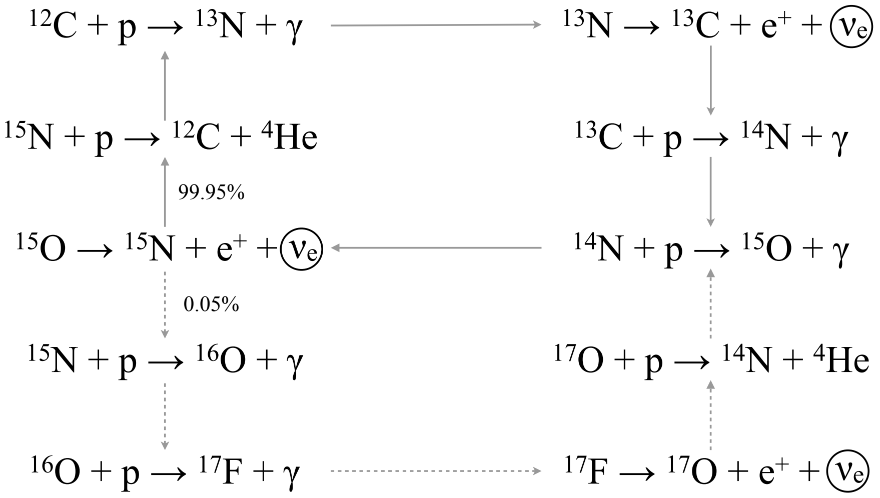

Figure 2.2: The CNO cycle, where carbon, nitrogen and oxygen serve as catalysts in the fusion process. In <0.2% of the decays electron capture occurs instead of β^{+} decay [15], leading to the faint mono-energetic lines seen in Figure 2.3. This is Figure 1.3 in [11].

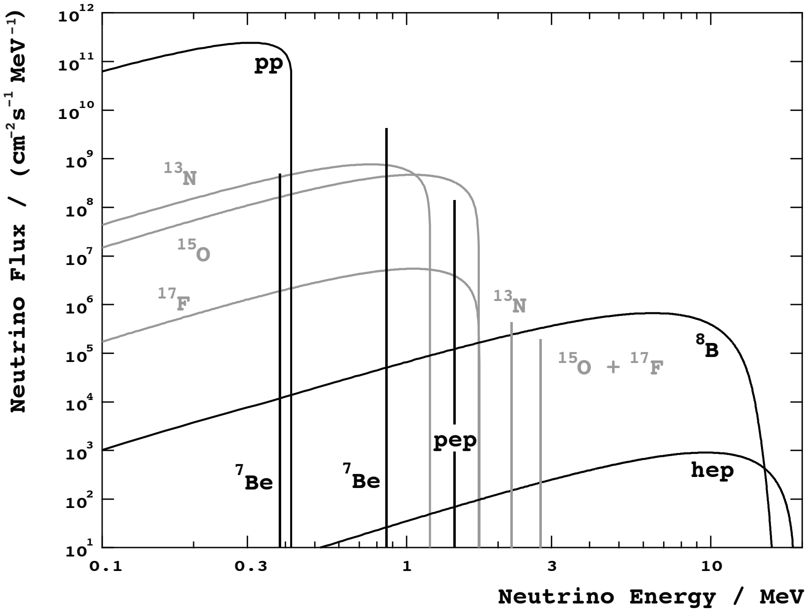

Figure 2.3: Energy spectra and fluxes of νs produced in the Sun. The black-lines show the ν species produced in the *p*-*p* fusion chain (Figure 2.1), while the gray lines are those produced in the CNO cycle (Figure 2.2). This is Figure 1 in [15].

as heavy as carbon, which are not produced by the processes in Figures 2.1 and 2.2, are constant throughout solar history.

- The model is constrained to match the present properties of the Sun (Table 2.1).

The latest elemental abundance measurements (AGSS09 [16]) give Z/X values that spoil the agreement between the SSM and helioseismology [17]. Therefore, flux results are also given (Table 2.2) for the old, higher Z/X values (GS98 [18]). The lower abundance of the heavy element catalysts in the CNO cycle (Figure 2.2) lead to smaller ν fluxes from this process. Furthermore, the smaller Z/X also decreases the radiative opacity (i.e. it is easier for energy to flow out of the inner regions of the Sun), leading to a decrease in the predicted value for the solar core temperature, lowering the ^{7}Be and ^{8}B ν fluxes (Section 6.2 of [14]).

The correlations between the different ν fluxes in the SSM are shown in Table 2.3. The radial profiles of the production of the different ν species in the Sun are shown

Solar ν species	Flux at Earth (Φ) / ($10^8\,\mathrm{cm}^{-2}\,\mathrm{s}^{-1}$)	
	High Z (GS98)	Low Z (AGSS09)
pp	598±4	603±4
^{7}Be	50.0±3.5	45.6±3.2
pep	1.44±0.02	1.47±0.02
^{8}B	0.056±0.008	0.046±0.006
He*p*	$(8.0\pm2.4)\times10^{-5}$	$(8.3\pm2.5)\times10^{-5}$
^{13}N	2.96±0.41	2.17±0.30
^{15}O	2.23±0.33	1.56±0.23
^{17}F	0.055±0.009	0.034±0.005
CNO	5.23±0.73	3.73±0.52

Table 2.2: Solar ν fluxes on Earth predicted by the SSM with two different inputs for the heavy element abundances or "metallicity" (Z). This is Table 2 in [9].

	pp	^{7}Be	*pep*	^{8}B	He*p*	^{13}N	^{15}O	^{17}F
pp	1	-0.819	0.954	-0.720	0.082	-0.349	-0.381	-0.319
^{7}Be	-0.819	1	-0.780	0.887	-0.062	0.154	0.204	0.332
pep	0.954	-0.780	1	-0.730	0.087	-0.407	-0.439	-0.369
^{8}B	-0.720	0.887	-0.730	1	-0.086	0.269	0.333	0.486
He*p*	0.082	-0.062	0.087	-0.086	1	-0.052	-0.058	-0.076
^{13}N	-0.349	0.154	-0.407	0.269	-0.052	1	0.991	0.172
^{15}O	-0.381	0.204	-0.439	0.333	-0.058	0.991	1	0.219
^{17}F	-0.319	0.332	-0.369	0.486	-0.076	0.172	0.219	1

Table 2.3: Correlation coefficients (Section 9 of [19]) between the different ν fluxes in the High Z SSM. The results for the Low Z SSM exhibit similar relationships (Table 17 in [19]). Note the strong correlation between the ^{13}N and ^{15}O ν fluxes.

in Figure 2.4.

2.2 Neutrino oscillations

The neutrinos produced in nuclear fusion are electron-neutrinos (ν_e). This label is associated with the charged lepton that is produced in the nuclear transmutation. Two other types of neutrinos are known to exist, ν_μ and ν_τ, which may interact with nuclei to produce the heavier μ (m=105.7 MeV) and τ (m=1777 MeV) charged leptons. As the masses of these leptons are larger than the energy released in nuclear

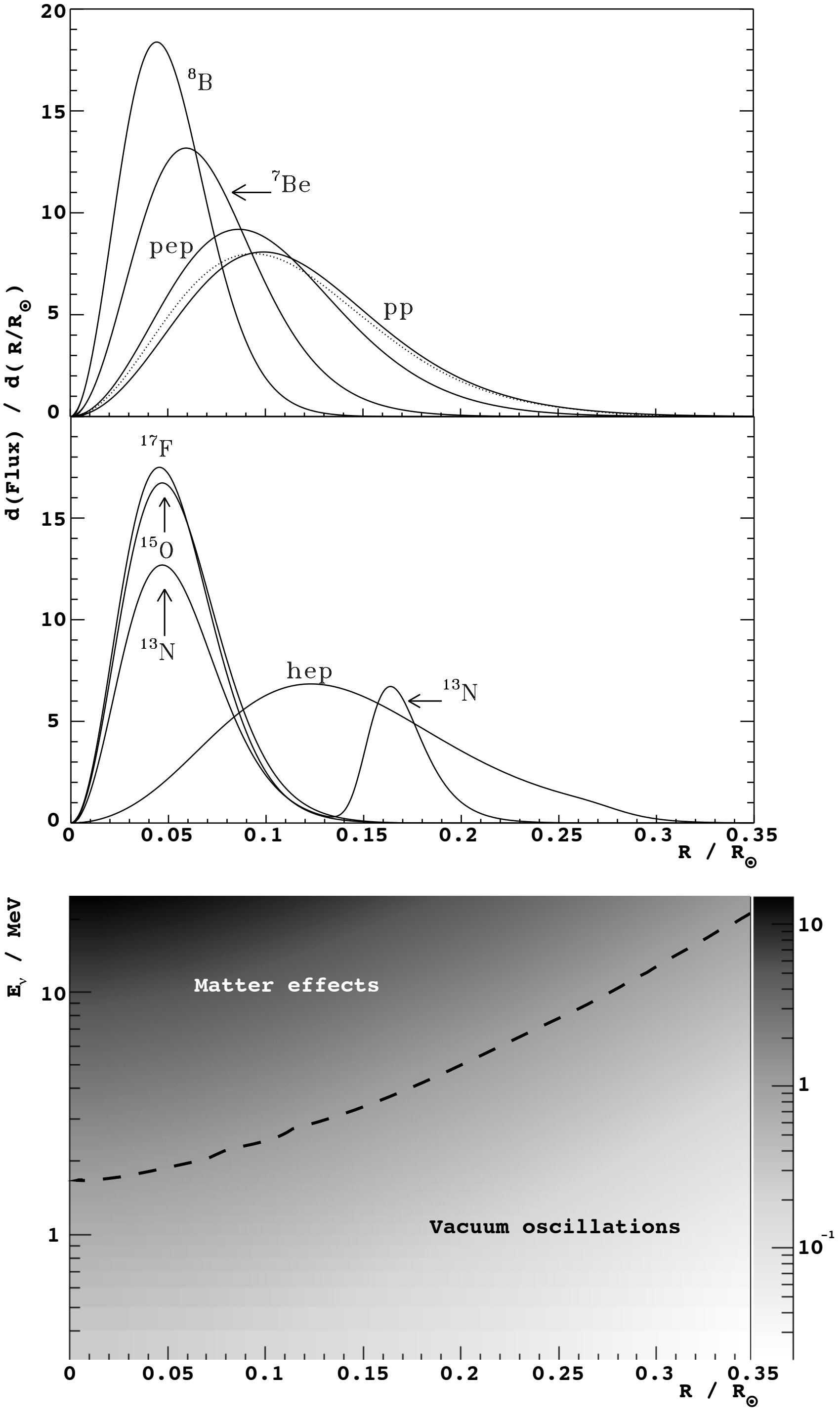

Figure 2.4: The top two panels show the production regions of the ν species, as given by the SSM [19]. The dotted line shows the profile of the energy production in the Sun. The bottom panel shows the region of parameter space where matter effects are important and where vacuum oscillations dominate. E_ν and R are the energy and radial position of the produced ν. The gray axis is the quantity $L_V/(L_e \cos\theta_{12})$. The dashed boundary is defined by the condition $L_V/(L_e \cos\theta_{12})$=1.

fusion and radioactive decay, CC interactions of ν_μ and ν_τ with matter do not occur at the energy scale of solar νs. Therefore, we consider these neutrinos together as ν_x, i.e. νs that only have NC interactions. Furthermore, these neutrinos may only arise through a phenomenon known as "neutrino oscillations".

Unlike the charged leptons, νs have masses <eV [20]. Furthermore, the ν mass eigenstates do not coincide with the flavor eigenstates [21], and their relationship can be parametrized with the mixing angle θ_{12} in an orthogonal matrix:

$$\begin{pmatrix} \nu_e \\ \nu_x \end{pmatrix} = \begin{pmatrix} \cos\theta_{12} & \sin\theta_{12} \\ -\sin\theta_{12} & \cos\theta_{12} \end{pmatrix} \begin{pmatrix} \nu_1 \\ \nu_2 \end{pmatrix} \tag{2.2}$$

where ν_e and ν_x are the flavor eigenstates, and ν_1 and ν_2 are the mass eigenstates. For a produced ν_e where the ν_1 and ν_2 components propagate with the same momentum, the time evolution of ν_e is

$$|\nu_e\rangle_t = \cos\theta_{12}\exp(-iE_1t)\,|\nu_1\rangle + \sin\theta_{12}\exp(-iE_2t)\,|\nu_2\rangle \tag{2.3}$$

where E_1 and E_2 are the energies of the different components, and t is the time since emission. We may also write the probability of having the emitted ν still interacting like a ν_e at time t after emission as

$$|\,\langle\nu_e\,|\,\nu_e\rangle_t\,|^2 = 1 - \sin^2 2\theta_{12}\sin^2\left[\frac{1}{2}(E_2 - E_1)t\right] \tag{2.4}$$

As long as the ν_1 and ν_2 masses (m_1 and m_2) are different (hence, $E_1 \neq E_2$), the two components will interfere, leading to the emergence of the ν_x flavor component of a ν originally emitted as a ν_e. The argument in Equation 2.4 may be more conveniently expressed as

$$\frac{1}{2}(E_2 - E_1)t = \frac{1}{2}\left(\frac{m_2^2 - m_1^2}{2E}\right)t \equiv \frac{\Delta m_{21}^2 t}{4E} \equiv \frac{\pi D}{L_V} \tag{2.5}$$

where D is the distance from the emission point and L_V is the vacuum oscillation length, which for solar νs has a value $L_V{<}0.002\,R_\odot$. As solar νs are produced over spatial regions that are much larger than L_V (Figure 2.4), for νs detected outside the Sun, the second $\sin^2$ term in Equation 2.4 averages such that [22]

$$|\langle \nu_e \,|\, \nu_e \rangle_t|^2 = 1 - \frac{1}{2}\sin^2 2\theta_{12} \tag{2.6}$$

2.2.1 Matter effects

Equation 2.6 gives the probability of detecting a ν that was produced in the Sun as a ν_e on Earth. In such case we have not considered the effects of the dense solar matter in the propagation of νs. Mikheyev, Smirnov and Wolfenstein (MSW) [23,24] demonstrated that such effects could have a significant impact on the oscillations.

The propagation of ν_e in matter is different than ν_x, as the forward scattering probability between ν_e and e^- is larger than between ν_x and e^- due to CC interactions (Figure 4.1). This results in a different mixing angle for νs traveling through matter (θ_M), i.e.

$$\tan 2\theta_M = \frac{\tan 2\theta_{12}}{1 - L_V/(L_e \cos 2\theta_{12})} \tag{2.7}$$

The ν_e-e interaction length (L_e) is inversely proportional to the strength of the interaction (Fermi's constant, G_F) and the electron number density (n_e):

$$L_e = \frac{\sqrt{2}\pi\hbar c}{G_F n_e} \tag{2.8}$$

In the case of νs produced in regions of very high n_e, $L_e{\ll}L_V$ and $\theta_M{\rightarrow}\pi/2$ (Equation 2.7). In such case, $|\nu_e\rangle{\sim}|\nu_2\rangle$ (Equation 2.2). As a ν propagates through the Sun, from dense matter to vacuum, the adiabatic approximation holds (Section 7.4 of [25]). This condition implies that no transitions between mass eigenstates occur, while their corresponding flavor composition changes with varying n_e. Therefore, for

Parameter	Value	
Δm^2_{21}	$(7.59\pm0.20)\times10^{-5}$ eV^2	
$\sin^2(2\theta_{12})$	0.87 ± 0.03	$(33^\circ < \theta_{12} < 36^\circ)$
$\sin^2(2\theta_{13})$	0.09 ± 0.02	$(8^\circ < \theta_{13} < 10^\circ)$

Table 2.4: Current best estimates for the parameters relevant for solar ν oscillations. Taken from the 2010 Particle Data Group [26] and the recent measurement of θ_{13} [27]. The combination of values for Δm^2_{21} and $\sin^2(2\theta_{12})$ are referred to as the Large Mixing Angle (LMA) solution.

a ν created in high e^- density and then propagates into the vacuum, the probability of it being detected as a ν_e outside the Sun is

$$|\langle \nu_e \,|\, \nu_2 \rangle|^2 = \sin^2\theta_{12} \tag{2.9}$$

On the other hand, for $L_e \gg L_V$, the vacuum oscillation result (Equation 2.6) applies. Evidently, there is a transition region between these two cases. The probability of a solar ν being detected as a ν_e on Earth (i.e. the survival probability, P_{ee}) can be approximated as [28] as

$$P_{ee} = \frac{\cos^4\theta_{13}}{2}\left(1 + \frac{\cos 2\theta_{12} - (\cos^2\theta_{13} L_V)/L_e}{\sqrt{(\cos 2\theta_{12} - (\cos^2\theta_{13} L_V)/L_e)^2 + \sin^2 2\theta_{12}}}\cos 2\theta_{12}\right) \tag{2.10}$$

where the θ_{13} terms arise from the consideration of the three flavor ν mixing matrix (not the two flavor approximation presented here (Equation 2.2)). The current best values for the parameters are shown in Table 2.4.

P_{ee} depends on L_V/L_e for the particular ν species. L_V is dependent on the ν energy, while L_e is dependent on where the ν is produced. Figure 2.4 shows the regions in the parameter space where matter effects are important and where vacuum oscillations take place. Figure 2.5 shows the computed P_{ee} for the different solar ν species. This prediction is known as the LMA-MSW solution to solar ν oscillations.

In terms of the particle physics parameters, θ_{12} determines the P_{ee} extremes, while the position of the transition region is given by Δm^2_{21}.

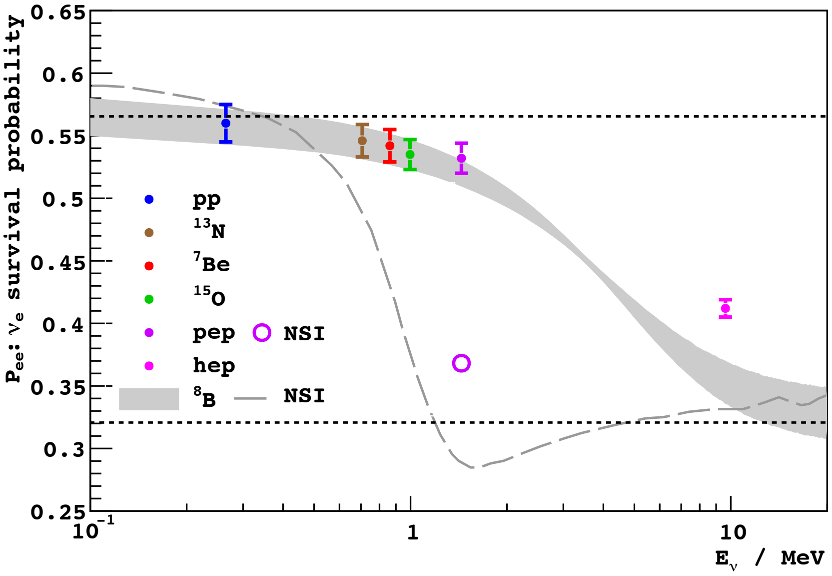

Figure 2.5: P_{ee} predictions for the solar ν species. The gray band and colored-filled markers show the predictions of LMA-MSW (Equation 2.10). A single, characteristic, mean energy is considered for *pp*, ^{13}N, ^{15}O and Hep νs. The higher P_{ee} for Hep νs is due to their production in the outer regions of the Sun, where matter effects are weaker due to lower e^- density (Figure 2.4). The gray dashed line and hollow marker show a prediction for *pep* and ^{8}B νs when non-standard matter interactions (NSI) are included. The dashed horizontal lines show the extreme cases (Equations 2.6 and 2.9). This is Figure 1.8 in [11] with NSI data from Figure 3 in [29].

The precise measurement of the ^{8}B ν survival probability for $E_\nu > 5$ MeV by SNO and Super-Kamiokande determined θ_{12} [30, 31], while KamLAND measured Δm^2_{21} from reactor $\bar{\nu}_e$ data [32].

Borexino (Chapter 3) is the only detector capable of detecting solar νs with $E_\nu < 3$ MeV. The successful detection of ^{7}Be νs [33] was the confirmation of the existence of the vacuum oscillation region below 1 MeV.

In this thesis we present the first attempt of the measurement of *pep* νs, which, at $E_\nu = 1.44$ MeV, are sensitive probes for ν interactions with matter, as non-standard models may have a large effect in the P_{ee} transition region [29, 34, 35]. Due to their similar energy and flux (Figure 2.3), solar νs from the CNO cycle will also be encountered in this search. The measurement of their flux may help shed light to the controversy regarding the heavy element abundances in the Sun (Table 2.2).

Chapter 3

Borexino

The Borexino detector [36] was designed with the main goal of measuring the interaction rate of the 0.86 MeV ^{7}Be solar νs via ν-e elastic scattering. The expected maximum electron recoil energy from these neutrinos is 0.67 MeV and their interaction rate is $<100\,\mathrm{day}^{-1}(100\,\mathrm{ton})^{-1}$. Therefore, the detector should be sensitive to sub-MeV electron recoil signals, large enough to accumulate the necessary statistics, and the backgrounds should be sufficiently low for the spectral features of the electron recoil spectrum from solar νs to be observable.

3.1 General setup

Borexino is located in Hall C of the Gran Sasso National Laboratories (LNGS) in central Italy. This underground site offers an average rock overburden of 1300 m (3800 m water equivalent), stopping most cosmic rays from reaching the detector. The residual cosmic ray flux is at the level where the associated backgrounds are sufficiently low for the detection of solar νs (Section 5.3).

Organic liquid scintillator was chosen as the active target in Borexino due to its high light yield ($\sim 10^4$ photons are produced for every MeV of deposited energy by an electron) and the possibility to produce a large, high-purity, unsegmented target mass.

Scintillation light is emitted isotropically and, therefore, it does not provide information about the direction of the recoiling particle, but its energy may be reconstructed from the detected number of photons (Section 6.5). Below 5 MeV, electron, positron and α recoils from the decay of natural radioactive isotopes are the dominant source of background. α and, to a certain extent, positron recoils can be discriminated by relying on differences in the time profile of the scintillation light (Section 6.4), while individual electron recoils from radioactive decay are indistinguishable from those from ν interactions. Thus, the solar ν signal has to be extracted from the features of the total electron recoil spectrum. In order for the statistical methods used to extract the signal to succeed, the total number of background events in the final spectrum needs to be as small as possible. Electron recoils may be produced in the active target not only by β decays of isotopes present in the scintillator (either from the long-lived chains of natural radioactivity (Section 5.1) or produced in situ by cosmic muons) but also by γ-rays from radioactive decays in the peripheral structure containing the scintillator. Therefore, an unsegmented, high-purity inner volume, capable of self-shielding and where the individual electron recoils may be localized, is desired.

Figure 3.1 is a schematic of the Borexino detector. The active target consists of 278 tons of organic liquid scintillator, surrounded by 889 tons of non-scintillating buffer fluid (Section 3.2). The innermost region of the active target, where backgrounds from external γ-rays are lowest, is known as the fiducial volume (FV) and is defined by an analysis cut on the reconstructed position of the scintillation events. The fluids are kept separate by an inner nylon vessel (IV) (Section 3.3). A second outer vessel (OV) divides the buffer region in two, serving as a barrier to prevent the diffusion of the radioactive gas, radon, into the active target. The scintillator and buffer fluids are inside a stainless steel sphere (SSS), on which most of the light detectors (photomultiplier tubes (PMTs), Section 3.4) are mounted. The SSS is housed within a tank containing 2100 tons of ultra-pure water, which serves as a veto for cos-

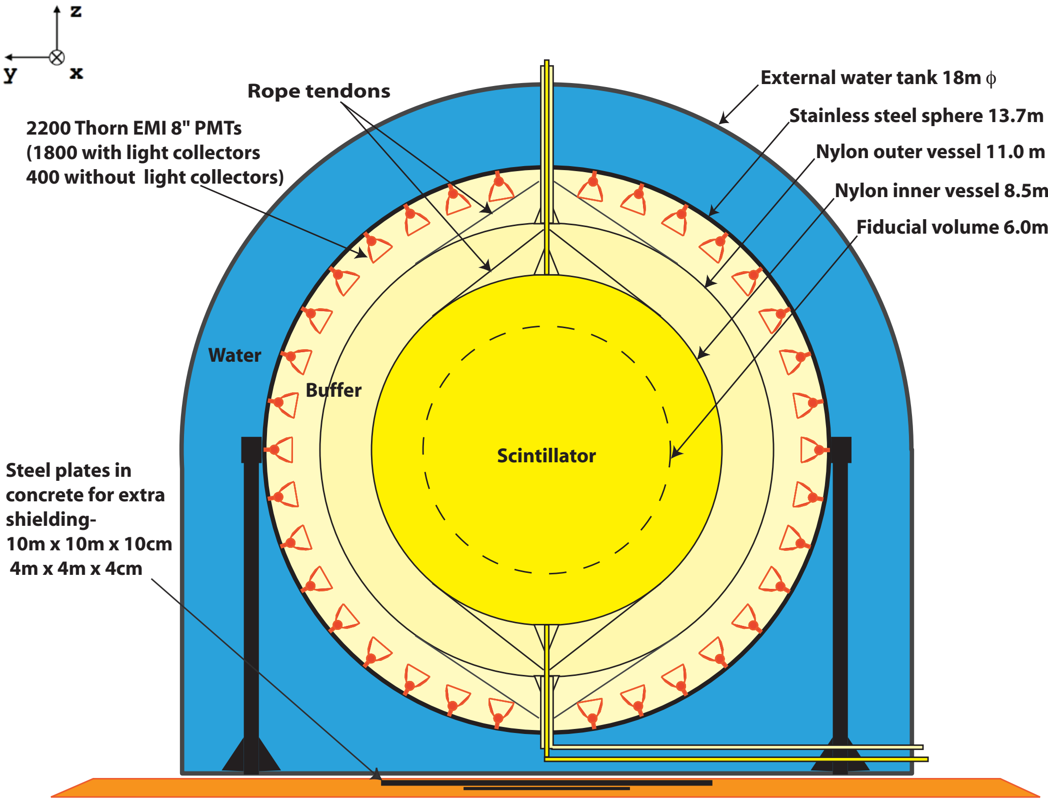

Figure 3.1: The Borexino detector [36]. It was designed to detect sub-MeV solar νs. It features a high light-yield, ultra-pure liquid scintillator target. A non-scintillating buffer region serves as shielding for external γ-rays. Its location at a deep underground site and its muon veto suppress cosmic backgrounds.

mic muons via the detection of Cherenkov light [37] produced as the muons traverse the water. The scintillator detector within the SSS is the inner detector (ID), while the water Cherenkov detector surrounding the SSS is the outer detector (OD).

3.2 Scintillator and buffer

In order to achieve a low background rate in the active target, it is important for both the scintillator and the buffer to be very low in radioactivity. It is simplest to produce both fluids from the same basic material that may be purified in large quantities [38–40]. This leads to several additional benefits, as the scintillator and buffer are very similar physically and chemically. For example, the differences in density are small enough (Table 3.1) to allow for the use of low mass, transparent, non-rigid nylon vessels (Section 3.3). Also, the almost identical optical properties greatly simplify the algorithm to reconstruct the position of the electron recoils in the active target (Section 6.3).

The scintillator and the buffer are pseudocumene-based fluids. The scintillator has the fluor 2,5-diphenyloxazole (PPO) as an additive at a concentration of $1.5\,\mathrm{g}/\ell$. Even though pseudocumene (PC) itself scintillates, when the fluor is added, 95% of the time excited PC molecules transfer their energy to PPO molecules via sub-ns non-radiative mechanisms [41]. The time profile of the PPO scintillation light has a 3 ns decay, smaller than PC's [42], and is, therefore, better suited for event position reconstruction (Section 6.3). Also, the fluorescence quantum efficiency is higher for PPO [42] and the peak emission wavelength is at 360 nm, near the point of maximum quantum efficiency of the PMTs (Figure 3.2), leading to an improved detected light yield. The PPO concentration was chosen as to maximize the photon yield (11500 photons/MeV for electron recoils [42, 43]), considering that at higher concentrations the fluor begins to re-absorb its scintillation light.

The photon yield and time profile of the scintillation light depend on the rate of energy loss of the charged particle in the scintillator. Therefore, α particles from radioactive decay produce less light (1000 photons/MeV) and have a mean photon emission time that is larger than electron recoils [42, 43]. The optical properties of the scintillator in the context of light yield and time distribution of the detected light will be briefly reviewed in Chapter 6. For a more detailed discussion on the chemistry of PC scintillation see Section 3.1 of [44].

The buffer fluid has the light quencher dimethylphthalate (DMP), originally at $5\,\mathrm{g}/\ell$, although its concentration was decreased to $2\,\mathrm{g}/\ell$ throughout the year 2009. This was done to reduce the buoyant force on the scintillator volume and, consequently, decrease the rate of a leak of scintillator into the buffer that appeared in the IV in April, 2008 (Section 2.3 of [11], and [45]). Even at $2\,\mathrm{g}/\ell$, the presence of DMP in the PC decreases the photon yield sufficiently (Table 3.1), such that interactions from external γ-rays in the buffer do not trigger the detector, keeping the data acquisition rates manageable, and do not constitute a background for solar ν spectroscopy [46]. Furthermore, DMP has a low light absorption in the wavelength range of the PPO scintillation spectrum (Table 3.1) and, therefore, its presence in the buffer has no detrimental effect to the detected light yield from electron recoils in the active target.

Fluid	Density	Scintillation yield	Index of	Mean Path Length / m	
	g/cm^3	photons/MeV	refraction	$\lambda = 350\,\mathrm{nm}$	$\lambda = 400\,\mathrm{nm}$
Scintillator	0.8802	11500 [43]	1.533 [47]	2×10^{-4} [43]	50 [43]
Buffer 1	0.8810	200 [48]	1.532 [47]	50 [48]	300 [48]
Buffer 2	0.8803	400 [48]	1.532 [47]	50 [48]	300 [48]

Table 3.1: Summary of the physical properties of the scintillator and buffer fluids. Buffer 1 corresponds to the composition of the buffer at filling, with a DMP concentration of $5\,\mathrm{g}/\ell$. Buffer 2 corresponds to the buffer after the DMP concentration was decreased to $2\,\mathrm{g}/\ell$. The density values are at $T = 15°\mathrm{C}$. The smaller difference in density between the scintillator and buffer led to a considerably smaller scintillator leak rate through the IV [49]. The scintillation yield for both buffer compositions is lower than the Cherenkov photon yield ($\sim$500 photons at 1 MeV). The index of refraction was measured at a wavelength of 405 nm. The mean path length of the scintillation light includes the effects of both absorption and scattering, which are relevant for the reconstruction of the energy and position of particle recoils, respectively. The very small attenuation length in the scintillator at 350 nm is due to radiative transport, which effectively shifts the scintillation light to longer wavelengths within a few cm of the emission point [42]. The mean path length of the buffer was measured at a DMP concentration of $1\,\mathrm{g}/\ell$.

Target	e^-	^{1}H	^{12}C	^{13}C	^{2}H	^{14}N	^{16}O
Abundance / (10^{29}/ton)	3.307	0.60	0.45	5×10^{-3}	10^{-4}	4×10^{-5}	4×10^{-5}

Table 3.2: Abundance in the scintillator of electrons and the most common nuclear targets. The e^- abundance determines the ν-e scattering rate (Chapter 4), the ^{1}H abundance determines the $\bar{\nu}_e$ interaction rate [50] and the free n capture time [51], and the abundances of the heavier isotopes determine the production yields of cosmogenic isotopes (Section 5.3). The ^{13}C and ^{2}H abundances also determine charged-current solar ν interaction rates (Chapter 4).

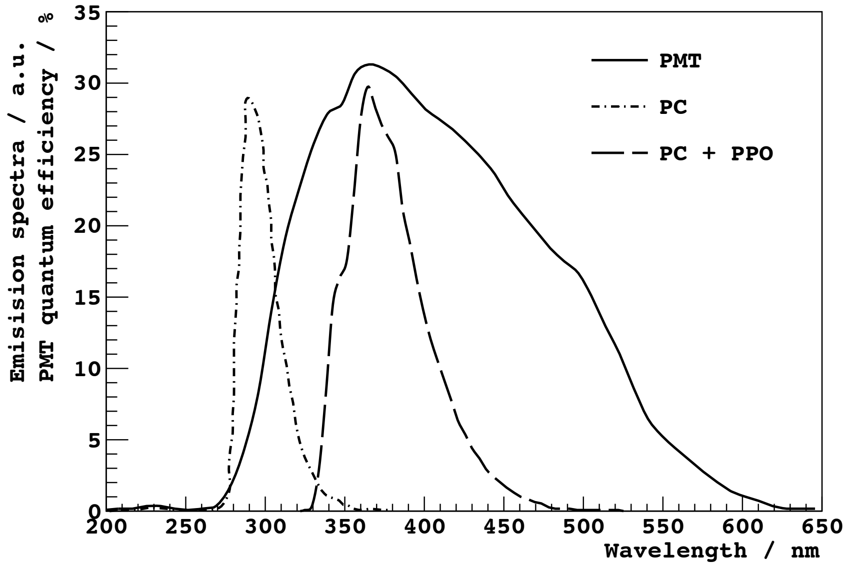

Figure 3.2: PMT quantum efficiency as a function of wavelength, compared to the normalized scintillation emission spectrum of pure PC and PC with PPO at 1.5 g/ℓ. Even though the detected light from PC+PPO in a large volume detector will be shifted to higher wavelengths due to radiative transport, this solution leads to a higher photon detection efficiency than pure PC. Additionally, the PC+PPO solution has a higher photon yield due to PPO's higher fluorescence quantum efficiency. This is a modified version of Figure 2.2 in [52].

3.3 Nylon vessels

The nylon vessels containing the scintillator and the inner buffer have the most stringent radioactive requirements after PC. Bulk contamination in the nylon leads to γ-ray background and the emanation of radon and thoron into the scintillator, while surface contamination can be washed off, affecting the scintillator's radio-purity. $125\,\mu$m thick nylon film allows for a containment vessel that meets the mechanical and transparency requirements with a relatively small mass, limiting the total bulk contamination. Assembly of the vessels in a low-radon environment assures low surface backgrounds. The vessels are held in place by two end caps at the top and the bottom of the ID (Figure 3.3). Pipes run through the end caps for filling the vessels and to accommodate the source insertion system (Section 3.6). Due to their large mass and vicinity to the scintillator, the vessel end caps are one of the largest sources of γ-ray background in the scintillator (Figure 7.1).

Details on the design, assembly and radioactivity of the vessels may be found in [40, 53]. The filling procedure of the vessels is described in [54].

3.4 Photomultiplier tubes

There are 2212 inward-facing PMTs installed on the inner surface of the SSS to detect the scintillation light produced in the active volume. Another 208 PMTs are installed in the water tank, as part of the Cherenkov veto [51]. In order to increase the light collection from events in the active volume and decrease the detection of light from the buffer regions, 1839 of the ID PMTs have conical light concentrators installed on the front of the PMT glass [55]. Some photomultipliers were left without the concentrators, as this may help in the identification of cosmic muons traversing only the buffer. Table 3.3 summarizes the instrumental properties of the PMTs and the acceptance criteria to select those to be used in Borexino's ID. These criteria were chosen as to guarantee a light yield and energy resolution that is sufficient to detect sub-MeV interactions and a timing response that will allow to reconstruct reliably the position of interactions in the active target [56, 57]. Data on the radioactivity of the PMT components may be found in [58, 59], and the corresponding γ-ray contribution to the count rate in the active target is shown in Table 5.4.

Photomultiplier tube parameter	Nominal value	Acceptance criterion
Quantum efficiency (420 nm)	26.5%	$> 21\%$
Rise time	0.67 ns	–
Transit time spread (FWHM)	2.8 ns	< 1.3 ns
S.P.E. peak-to-valley ratio	2.5	> 1.5
Dark current at 10^7 gain	25 nA	–
Dark count rate	–	$< 2 \times 10^4$ Hz

Table 3.3: Parameters for 8″ ETL 9351 photomultiplier tubes used Borexino's ID. The second column gives the nominal values from the manufacturer while the third column gives the criteria used to accept or reject tubes. The tubes are operated at a nominal gain of 10^7. This is Table 2.1 in [11], with values taken from [36].

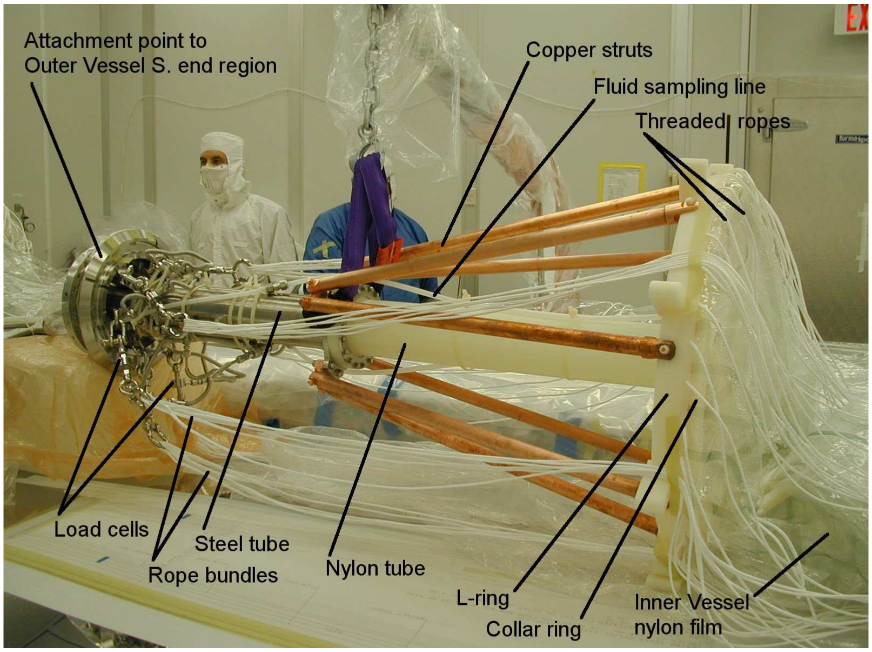

Figure 3.3: This is the bottom end region of the IV during construction. It is now installed in the bottom of the ID, with the left end pointed downward. The nylon ropes offer mechanical support for the vessel. Due to their significant mass and vicinity to the scintillator, the nylon, copper and steel in the end caps are a major source of γ-ray background in the active volume. This is Figure 3.7 in [44].

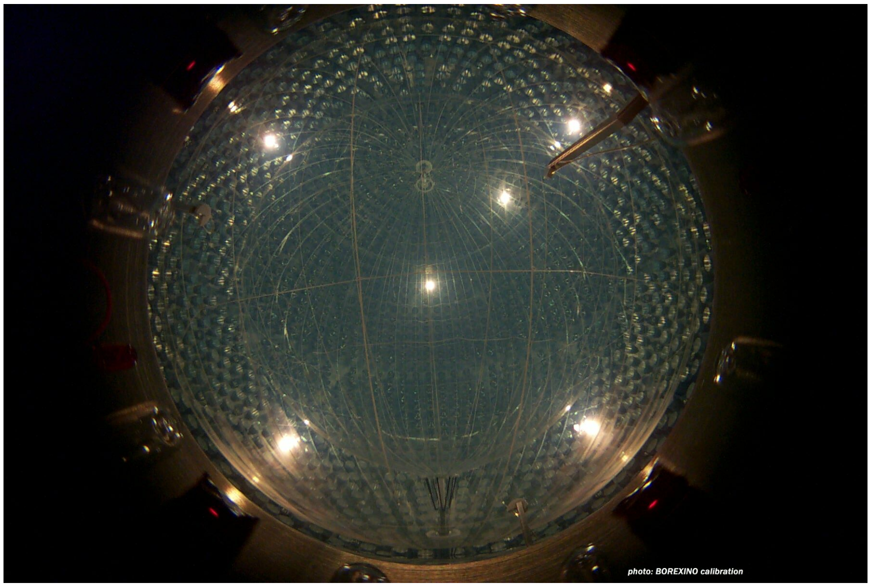

Figure 3.4: Borexino's ID, photographed by one of the cameras installed on the SSS. The end region shown in Figure 3.3 may be observed at the bottom, below the IV. The inward-facing PMTs installed on the SSS may be seen in the background. The transparency of the scintillator, buffer and nylon vessels is noticeable.

3.5 Electronics and data acquisition (DAQ)

The Borexino ID electronics were designed to have sub-ns precision on the relative time of the first photoelectron (pe) produced by every PMT from a single scintillation event. Considering that the mean number of pe produced by a PMT is <1 for most of the energy range of solar ν spectroscopy (Section 6.5), recording the time of every pe is not crucial for reliable event position reconstruction (Section 6.3) and pulse shape discrimination (Section 6.4). On the other hand, the total charge (or total number of pe) produced by the PMT from the scintillation event is recorded, as this information is valuable for event energy reconstruction (Section 6.5), particularly for high energy events (>1 MeV).

Figure 3.5 is a schematic of the Borexino electronics. The Borexino PMTs are AC coupled, i.e. both the HV supply and the PMT signal are on the same cable. The decoupling of the signal is performed by the front-end electronics [60], which provide, from every ID PMT, an amplified signal for the evaluation of the PMT hit time and an integrated signal [61] for the evaluation of the total charge. Additionally, the front-end also provides the total analog sum of the signals from all ID PMTs to a parallel DAQ system (Section 3.5.1).

The digitizers that sample every PMT signal from the front-end are the Laben boards [63]. The amplified signal goes through a dual discriminator and triggers the channel if the signal is above the high (0.25 pe) threshold. At the point when the amplified signal surpassed the low (0.1 pe) threshold and 80 ns later, a 10 MHz triangular wave running in phase with an external clock is sampled to obtain the time of the first pe. The integrated signal is also sampled at these points in time to obtain the charge output by the PMT within 80 ns of the first pe. This information is stored in a local memory buffer. To allow for the data to be read out by the MVME 2302 computer in the event of a system-wide trigger, the discriminator is disabled for 140 ns after the channel triggers. A software veto of an additional 40 ns is also

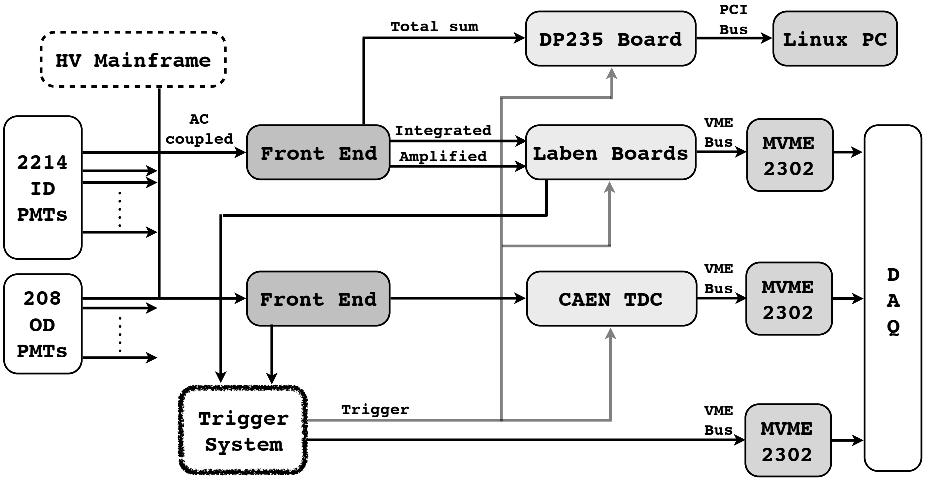

Figure 3.5: Schematic of the DAQ electronics. The front-end electronics decouple the PMT output and forward signals from every channel to the digitizers, i.e. the 280 Laben boards (14 racks with 20 boards each) and the CAEN TDCs. The ID front-end also provides the analog sum of all ID PMTs to the DP235 board (Section 3.5.1). The data from both the Laben and OD digitizers are read out by the MVME 2302 computers after every trigger, while the DP235 board is only read out after the MTB trigger (Table 3.4). An on-line system manages the data acquisition from the Laben boards, CAEN TDCs and trigger system, while the data from the DP235 board are read independently by another PC. This is a modified version of Figure 4.1 in [62].

enforced to avoid false retriggers. Thus, the channel can accept at most one hit in 180 ns and the charge arriving between 80 ns and 180 ns after the first pe is never recorded. More information about the ID electronics may be found in Section 5.2 of [36] and Section 4.2 of [62][1].

Similarly, the OD electronics are responsible for measuring the time of the first pe and the charge output by every PMT from an event in the water tank. A detailed description of the OD electronics is present in Section 2.3 of [51] and Section 4.3 of [62].

The trigger system evaluates signals from the ID and OD, and determines when to issue different triggers to acquire data from the digital boards. When a trigger

---

[1] Even though [62] is the most detailed reference for the DAQ electronics, it dates from 2006, before certain features had been implemented and before many of the parameters were set. Wherever conflicts between [62] and [36], or between [62] and this text are found, the latter two should be trusted.

Trigger	Condition	Comments
ID	25 ID PMTs hit in 60 ns	<100 keV threshold for electron recoils in the active target.
MTB	6 OD PMTs hit in 150 ns	To tag cosmic muons. For efficiency, see "MTF" in Table 3 in [51]. Also triggers Princeton 1-channel system.
128	MTB triggered	For the acquisition of cosmogenic neutrons. Introduced in December 2007.
Pulser	Every 0.5 s	Electronic pulse sent to every channel to check its status.
Laser	Every 0.5 s	ID PMTs are illuminated with a laser via an optical fiber [64] to calibrate the timing and charge response of every channel.
Random	Every 0.5 s	Not in coincidence with any signal. To evaluate the dark noise of the channel.

Table 3.4: The different types of triggers issued in Borexino. The first three are those to acquire data from particle interactions in the detector, while the last three (the "service triggers") are used to calibrate the channels. At the beginning of the experiment, data were acquired for 6.9 μs in response to any trigger except 128. This window was later increased to 16.5 μs. There is a delay, such that the trigger time falls ~0.4 μs after the beginning of the acquisition. Trigger 128 opens a 1.6 ms data acquisition window 140 ns after the acquisition from the previous MTB trigger, in order to register cosmogenic neutrons. The conditions given are nominal (and most common) and may be changed by the user, e.g. the service triggers are issued at higher rates during the "electronics calibration" runs that are done on a weekly basis.

is released, data within a set time window about the trigger time are read out from the Laben boards and CAEN TDCs (OD digitizers). Table 3.4 lists the different type of triggers and their causes. For every trigger issued, a GPS time stamp with a precision of ~100 ns is assigned to it and the information is read out by a MVME 2302 computer. Another on-line computer runs the general DAQ software that, after every trigger, handles the data from the Laben, OD and trigger systems and writes them to disk. For more information about the trigger system see Section 7 of [36] and Section 4.4 of [62], while for the on-line system that manages the data acquisition see Chapter 5 of [62].

As the CAEN TDCs can hold at most four events in their internal buffers, a veto is enforced to prevent a third trigger in less than 100 μs [62], assuring enough time for data readout and preventing buffer overload. Even though this limitation is generally not a problem, neutrons produced by cosmic muons will capture in the scintillator within a few ms of the primary muon shower (Section 5.3.1), producing a high rate of γ-ray events, most of which would be missed under regular triggering conditions. The detection of these events is crucial for the suppression of certain cosmogenic backgrounds (Section 7.3). Thus, trigger 128 was implemented, which fires immediately after a muon crosses the detector and opens a 1.6 ms data acquisition window, in which most of the neutron capture γ-rays fall. To evaluate the performance of the electronics in these circumstances, two parallel data acquisition systems were installed (Section 3.5.1 and [65]).

3.5.1 Princeton 1-channel system

The Princeton 1-channel system consists of an Acqiris DP235 PCI board, which is a 500 MHz, 8-bit digitizer. The input signal to the board is the total sum of the output from all ID PMTs, which is provided by the ID front-end electronics (Figure 3.5). Data are read out by a Linux PC in a 1.6 ms data acquisition window in response to the MTB trigger. This window overlaps with the data acquisition by the Laben system following trigger 128 and, therefore, provides a high-resolution copy of the total detector signal after a muon shower, which can be used to evaluate the performance of the Laben system. The 1-channel system took data from June, 2007 to November, 2009. The initial results, performance and comparison to the Laben system may be found in [66].

It was found that a large number of PMT hits within the 1.6 ms acquisition window are lost by the Laben system. The effect is more pronounced for higher energy muon showers, in which more neutrons are produced. This is because the Laben board memory can hold at most $\sim$2000 hits after a trigger, and if the memory is filled, the data are lost. Some muons may produce hundreds of neutrons in the active target

(Figure 5.5), leading to $>10^6$ pe produced within 1.6 ms, which fill up the memory of most boards and thus, a large fraction of the data are lost. In the worst cases, individual identification of the neutron capture γ-rays is impossible in the Laben system. For this reason, it is important to use data from the 1-channel system for the effective suppression of cosmogenic backgrounds (Section 7.3).

The success of this setup in identifying the production of free neutrons in the scintillator led to the design and installation of a similar system for the prompt detection of galactic supernovas [67].

3.6 Internal source calibration apparatus

In order to quantify how well Borexino has met its design specifications in terms of the reconstruction of the energy and position of particle recoils in the active target, and to evaluate the associated systematic uncertainties, calibration of the detector with internal radioactive sources must be performed. To place the sources within the active target, the Virginia Tech group has developed an internal source calibration system that does not compromise the scintillator's radio-purity (Chapter 6 of [68]). This system consists of a series of 1 m long rods that may be attached one after another. A special hinge rod (Figure 3.6), which can be rotated up to 90° from the vertical, may also be installed, allowing to reach any point within the IV. The rods are inserted from the top of Borexino and the source position may be obtained, with a nominal uncertainty of ±1.1 cm (Section 6.6 of [69]), by comparing photographs taken by the seven cameras installed on the SSS (Chapter 5 of [68]).

Most of the sources deployed in the active target consist of a 1 inch diameter vial (Figure 3.6) filled with a radioactive solution. A source made from Borexino's scintillator fluid with dissolved ^{222}Rn gas and ^{14}C-enriched toluene was deployed in a large number of positions in the active target to evaluate the performance of the event

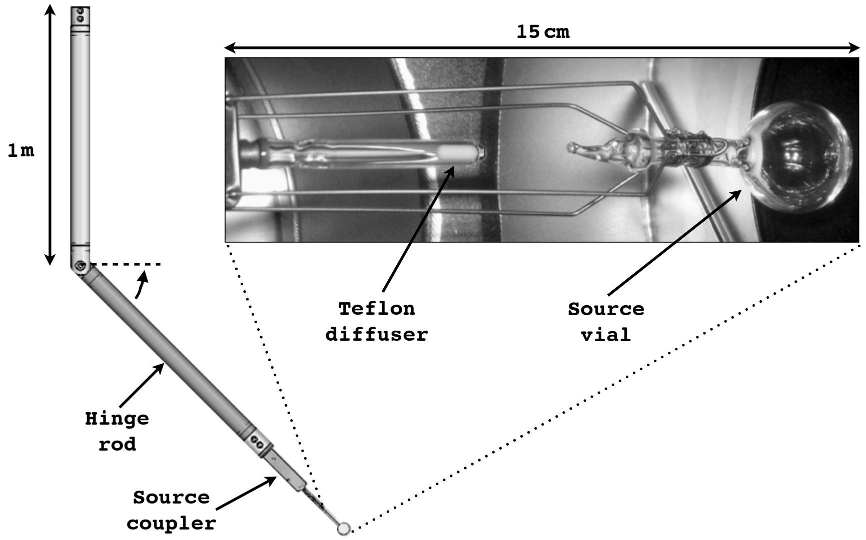

Figure 3.6: Schematic of the source insertion system. The rods and the source are placed inside the active target from the top of Borexino. The hinge rod may be rotated up, to access off-axis positions. The radioactive sources are kept in a solution within the transparent vial, except for the ^{241}Am-^{9}Be neutron source, which has a special delrin holder with lead shielding (not shown, Figure 7.7 in [68]). The teflon diffuser is illuminated with a red laser via an optical fiber so that the source may be located by the camera system.

position reconstruction. Multiple γ-ray sources in a non-scintillating solution were used to calibrate the energy response of the detector (Section 6.5). Additionally, an ^{241}Am-^{9}Be neutron source was placed in multiple locations to evaluate the detector's response to the 2.22 MeV γ-ray from n capture on ^{1}H, particularly relevant for the detection of $\bar{\nu}_e$ [50, 70]. The procedures for the production of the different radioactive sources may be found in Chapter 7 of [68], while the details of the four internal source calibration campaigns are in Appendices D–F of [68].

3.7 External source calibration apparatus

Borexino was designed such that for the measurement of the ^{7}Be solar ν interaction rate, the background rate of external γ-ray interactions whose position is reconstructed within the FV is negligible [53]. Yet, this background needs to be considered for the measurement of the *pep* and CNO solar ν interaction rates, which are expected to be ten times lower.

In order to understand the detector's response to external γ-rays, a 5 MBq ^{228}Th source was developed [71]. This source leads to an intense flux of 2.6 MeV γ-rays from the decay of ^{208}Tl, which are also produced in the decay chain of natural ^{232}Th (Figure 5.2), and constitute a dominant source of external γ-ray background in the active target from the peripheral structure (Table 5.4).

The calibration source may be placed at multiple locations in either the water tank or the buffer, inside tubes that pierce through the OD and SSS and extend 0.5 m into the buffer. For details on the source insertion and the calibration campaign see Section 5.3 of [72].

3.8 Detector history and stability

In the extraction of the solar ν signal (Chapter 8) we assume that Borexino is, to first-order, stable i.e. that the response of the detector to particle interactions is time-indepedent. Figures 3.7 and 3.8 summarize the stability of the inner detector and the electronics, respectively.

Figure 3.7 shows the volume of the inner vessel, which is a good representation of the status of the active target as it is sensitive to changes in temperature (density of the scintillator), vessel shape (the volume changes with deviations from sphericity) and leak of scintillator into the buffer. Figure 3.8 is the number of PMT channels from which data is considered for the analysis. Their number represents well the status of the PMTs and the electronics. Changes in the figures are often associated with detector operations. A detailed schedule of these may be found in [73].

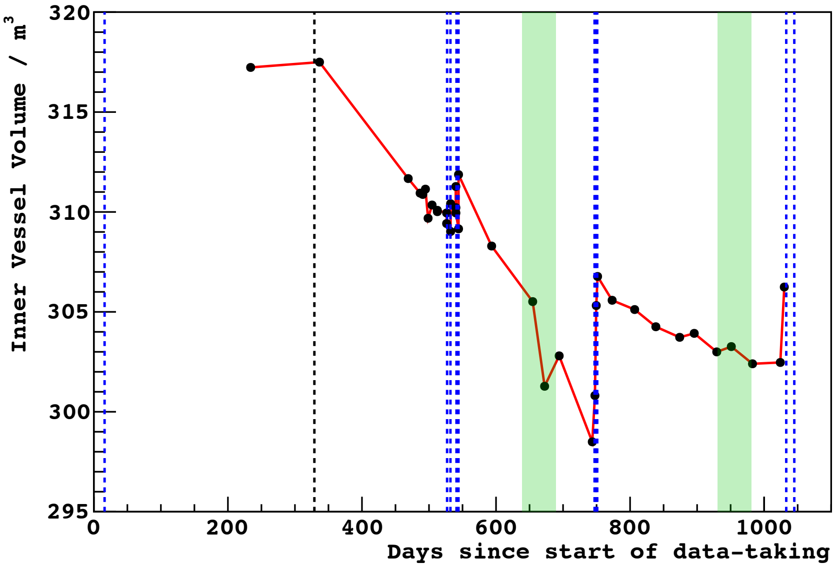

Figure 3.7: Volume of the inner nylon vessel as a function of time. The black points indicate the vessel volume as calculated from pictures of the inner detector by the CCD cameras [49]. The red line is a simple linear interpolation between each set of pictures. The dashed black line marks the best estimate for the start of the leak in the inner nylon vessel. The blue lines indicate refilling of the inner vessel scintillator and the green shaded areas designate buffer purifications and DMP removal. This is Figure 2.8 in [11].

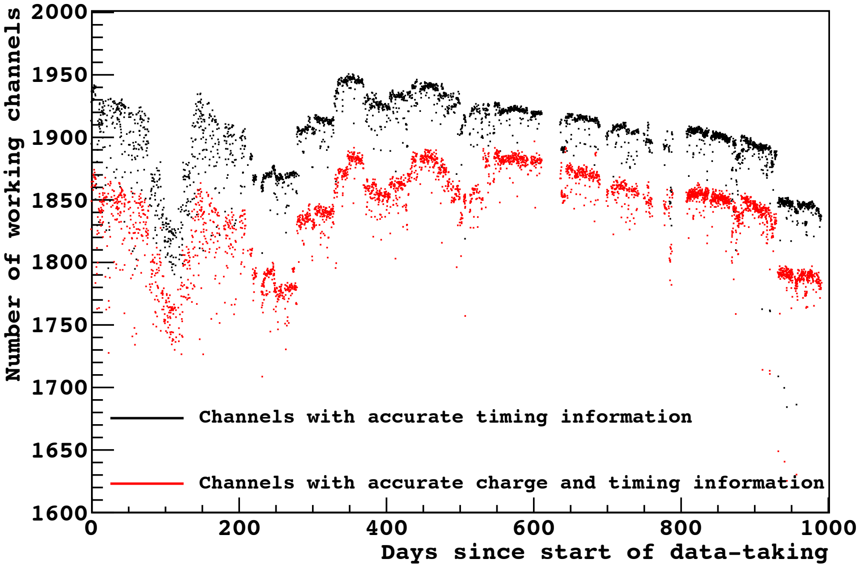

Figure 3.8: Number of working channels as a function of time. The number of channels with reliable timing information is shown in black, while the number of channels with reliable timing and charge information is shown in red. The exact criteria for selecting the reliable channels is not available in written form (ask L. Ludhova), although many of the factors considered may be found in A.1.3 of [74]. This is Figure 4.2 in [11].

Chapter 4

Solar Neutrino Signal

The dominant solar ν interaction in Borexino is elastic scattering with electrons. Table 4.1 shows the expected interaction rates assuming the SSM fluxes (Table 2.2) and neutrino oscillation parameters (Table 2.4). The maximum kinetic energy, T_{max}, of a recoiling particle when scattered elastically by a neutrino of energy E_ν occurs in the case of maximum momentum transfer, i.e. when the neutrino is scattered 180° backward:

$$T_{\text{max}} = \frac{2E_\nu^2}{2E_\nu + mc^2} \tag{4.1}$$

The maximum energy of the recoiling electrons from the different solar ν species is also given in Table 4.1. Elastic scattering with nuclei in the scintillator also occurs, but in this case the recoil energy is $<0.7\,\text{MeV}$ and, considering the lower light yield for protons than for electrons in the liquid scintillator (Section 6.5), the intensity of the light signal from the recoiling nuclei is below the analysis threshold ($0.3\,\text{MeV}$).

The rate of inelastic interactions (i.e. charge-current and nuclear excitation or breakup) of ^{8}B and Hep νs with ^{13}C [75,76] and ^{2}H [77] nuclei are $<0.01\,\text{day}^{-1}(100\,\text{ton})^{-1}$. Inelastic interactions between Hep νs and ^{12}C are also kinematically possible but the rates are even lower. It should be noted, though, that for the detection of other cosmic signals (e.g. the neutrino burst from a core collapse supernova), inelastic interactions

Solar ν species	E_ν/MeV	T_{max}/MeV	$R_0/(\text{day}^{-1}(100\,\text{ton})^{-1})$	
			High Z	Low Z
pp	<0.420	0.261	133.0±0.8	134.1±0.8
^{7}Be	0.384	0.231	1.9±0.1	1.8±0.1
^{7}Be	0.862	0.665	47.6±3.4	43.4±3.1
pep	1.442	1.225	2.80±0.04	2.86±0.04
^{8}B	<15.0	14.5	0.46±0.06	0.38±0.05
^{13}N	<1.199	0.988	2.5±0.4	1.8±0.3
^{15}O	<1.732	1.509	2.8±0.4	2.0±0.3
^{17}F	<1.740	1.517	0.07±0.01	0.04±0.01
CNO	<1.740	1.517	5.4±0.8	3.8±0.6

Table 4.1: The predicted ν-e scattering interaction rates (R_0) and the maximum kinetic energy of the recoiling electron (T_{max}) from the relevant solar ν species in Borexino. Predictions by the high and low metallicity SSMs are presented. The neutrino energy of each solar species (E_ν) is also given. The CNO species is the total contribution from ^{13}N, ^{15}O and ^{17}F νs, which may be treated as a single species due to the strong correlation between their fluxes (Table 2.3). The interaction rates of He*p* νs and of the mono-energetic νs from the EC decay of ^{13}N, ^{15}O and ^{17}F in the Sun (Figure 2.3) have interaction rates that are $<0.05\,\text{day}^{-1}(100\,\text{ton})^{-1}$, and are excluded from the table.

with ^{12}C [78] and elastic scattering with nuclei [79, 80] may contribute significantly to the total observed yield.

To obtain the predicted rate of ν-e interactions, as well as the energy distribution (spectral shape) of the recoiling electrons to be used for the signal extraction (Chapter 8), we need to consider that both ν_e and ν_x may scatter elastically with electrons in the scintillator. The differential cross-section for this process is [81]

$$\frac{d\sigma}{dT}(T, E_\nu) = \frac{\sigma_0}{m_e c^2}\left[g_L^2 + g_R^2\left(1 - \frac{T}{E_\nu}\right)^2 - g_L g_R\left(\frac{m_e c^2}{E_\nu}\frac{T}{E_\nu}\right)\right] \tag{4.2}$$

$$\text{where } \sigma_0 = 8.81\times10^{-45}\text{cm}^2,\ g_L = \pm0.5 + g_R,\ \text{and } g_R = 0.2317 \tag{4.3}$$

The upper sign in g_L applies to ν_e-e scattering, while the lower sign to ν_x-e scattering. This result arises by considering the two interaction channels shown in Figure 4.1. By integrating Equation 4.2 from T=0 to T_{max} we obtain the total interaction cross section (σ_ν). Figure 4.2 shows σ_ν as a function of E_ν.

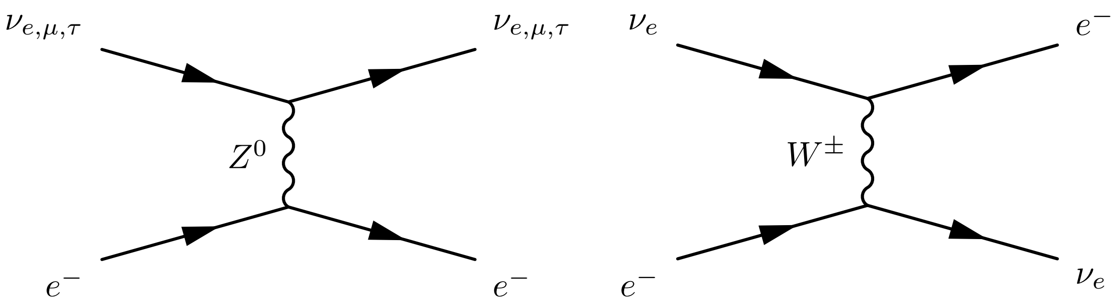

Figure 4.1: First-order Feynman diagrams of the possible weak interactions between neutrinos and electrons. Left: neutral current (NC) interaction between a neutrino and an electron via the exchange of a Z boson. This interaction is the same regardless of the ν flavor (ν_e or $\nu_{\mu,\tau} \equiv \nu_x$). Right: charge current (CC) interaction, exclusively between ν_e and an electron, where a charged W boson is exchanged.

In absolute terms, σ_ν is very small, e.g. the mean path length for a $\sim$MeV solar ν in ordinary matter is $\sim 10^{18}$ m. Thus, the solar ν flux is constant throughout the spatial extension of Borexino and, consequently, solar ν interactions should be distributed uniformly in the active target.

The time dependence of the solar ν signal should feature an annual modulation associated with the changing distance between the Earth and the Sun, being 7% larger at perihelion than aphelion[1]. According to LMA-MSW (Section 2.2.1), no measurable daily variations in the ν interaction rates are expected, a prediction that has been confirmed by a previous Borexino analysis [82].

4.1 ^{7}Be and *pep*

^{7}Be and *pep* solar νs are mono-energetic (Table 4.1) and their ν-e scattering rates are given by

$$R = \Phi \left(P_{ee}\sigma_{\nu_e} + (1 - P_{ee})\sigma_{\nu_x} \right) n_e \tag{4.4}$$

where Φ is the total flux of the solar neutrino species (Table 2.2), P_{ee} is the ν_e survival probability (Figure 2.5), σ_{ν_e} and σ_{ν_x} are the ν_e-e and ν_x-e scattering cross-

---

[1] For the data considered in this analysis (Table 7.1) the average Earth-Sun distance is 1.002 AU.

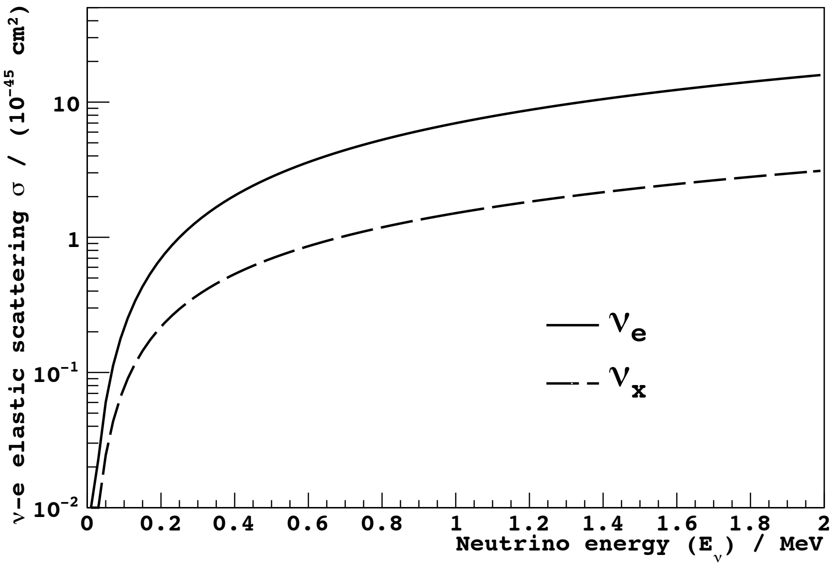

Figure 4.2: ν-e elastic scattering cross-section as a function of incident neutrino energy. As ν_e can couple to e^- via the CC interaction, in addition to the flavor insensitive NC interaction (Figure 4.1), its total interaction probability is larger. Interaction probabilities increase with energy and are 4–5 times larger for ν_e than ν_x in the considered energy region. For this graph we have taken into account the ∼2% effect from radiative corrections [83].

sections, respectively (Figure 4.2), and n_e is the electron density of the scintillator (Table 3.2). The terms $P_{ee}\sigma_{\nu_e}$ and $(1 - P_{ee})\sigma_{\nu_x}$ are evaluated at E_ν and correspond to the contributions from ν_e and ν_x, respectively.

The normalized electron recoil spectra from ν_e and ν_x for *pep* and 0.86 MeV ^{7}Be νs are shown in Figure 4.3. The observed species spectra in Borexino are a linear combination of the recoil spectra from the different ν flavors, weighted according to their contribution to the the total interaction rate. As the differences between the electron recoil spectra from ν_e and ν_x for mono-energetic species are small, the extraction of the interaction rate from ^{7}Be and *pep* νs is largely independent on the assumed flavor composition of the incident flux and, therefore, on the oscillation model.

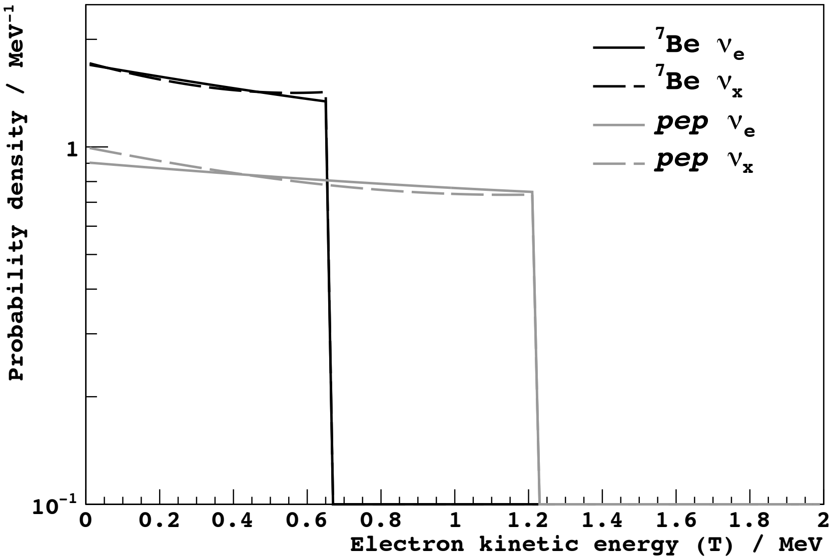

Figure 4.3: Normalized electron recoil spectra, as given by Equation 4.2, from the ^{7}Be (E_ν=0.86 MeV) and *pep* (E_ν=1.44 MeV) mono-energetic solar ν lines. The characteristic box shape with a sharp cut-off at T_{max} is evident for recoils from both ν_e and ν_x.

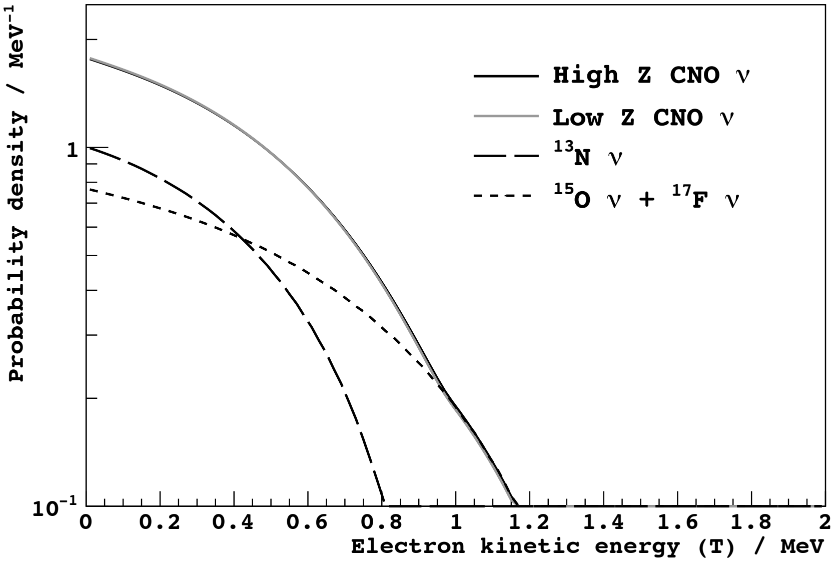

Figure 4.4: Electron recoil spectra from neutrinos produced in the CNO cycle. The solid lines are normalized to unity and show the cumulative spectrum from all CNO νs, with the fluxes given by the high and low metallicity (Z) SSMs. The dashed lines are the relative contributions from the individual species. In constructing these spectra we use Equation 4.5, with the P_{ee} profile given by LMA-MSW (Figure 2.5). The total CNO spectral shape is insensitive to changes, within uncertainty, of the parameters in the SSM and LMA-MSW (Chapter 2).

4.2 CNO

The energy spectra of neutrinos from the β-decay (Table 5.1) of ^{13}N, ^{15}O and ^{17}F in the Sun are continuous, with maximum energies, E_{max}, given in Table 4.1. To calculate the energy spectra of the elastically scattered electron recoils, we integrate over the incident neutrino energy spectrum, i.e.

$$\frac{dR}{dT}(T) = n_e \int_0^{E_{\text{max}}} \frac{d\Phi}{dE_\nu}(E_\nu) \left(P_{ee} \frac{d\sigma_{\nu_e}}{dT}(T, E_\nu) + (1 - P_{ee}) \frac{d\sigma_{\nu_x}}{dT}(T, E_\nu) \right) dE_\nu \tag{4.5}$$

where dR/dT is the differential rate, $d\Phi/dE_\nu$ is the neutrino differential flux (i.e. total flux × normalized energy spectrum [84]) and $d\sigma/dT$ is given by Equation 4.2. Integration of Equation 4.5 from T=0 to T_{max} leads to the total interaction rates of these species.

As is the case for mono-energetic νs, the difference between the normalized electron recoil spectrum from a continuous pure ν_e (P_{ee}=1) and pure ν_x flux (P_{ee}=0) is small (Figure 7 in [85]). Nevertheless, as P_{ee} depends on E_ν (Figure 2.5), and the absolute magnitude of σ_{ν_e} and σ_{ν_x} are significantly different (Figure 4.2), changes in P_{ee} throughout the energy range of the continuous spectrum can lead to spectral distortion. An example of this phenomenon is the expected "upturn" with decreasing energy in the electron recoil spectrum from ^{8}B νs due to the increase in P_{ee} with decreasing E_ν [86]. For CNO νs, whose energy range is mostly within the vacuum-oscillation region, the uncertainties in P_{ee} within LMA-MSW lead to <1% changes in the normalized electron recoil energy spectra. We stress, though, the significant dependence of the recoil spectra, which are used to extract the corresponding interaction rates (Chapter 8), on the oscillation model.

Figure 4.4 shows the electron recoil spectra from ^{13}N, ^{15}O and ^{17}F νs. As the β-decay of ^{15}O and ^{17}F are allowed nuclear transitions, with almost identical Q-values (Table 4.1), and daughter nuclei that are very close in atomic number, their emitted neutrino energy profiles are very similar. Therefore, the contribution of the ^{17}F νs can be considered as a few % increase in the ^{15}O ν flux. Furthermore, there is a strong correlation between the ^{13}N and ^{15}O ν fluxes predicted by the SSMs (Table 2.2), i.e. under the change of the solar model parameters within uncertainty, and even under the change of solar model (high or low metallicity), the ratio between these fluxes changes by $<$2%. Figure 4.4 illustrates the magnitude of this difference in the total electron recoil spectrum from CNO νs.

4.3 Other

The electron recoil spectra and rates from *pp* neutrinos can be computed from Equation 4.5 (Figure 5 in [85]), while the 0.38 MeV ^{7}Be νs should lead to a box-shaped electron recoil spectrum characteristic of a mono-energetic species (Figure 6 in [85]). In both cases, T_{max} is below the energy threshold of this analysis (0.3 MeV) and, therefore, their contribution to the count rate in the relevant energy range is negligible.

The ^{8}B electron recoil spectrum may also be computed from Equation 4.5 (Figure 3 in [85] and Table IV in [83]), although due to its large T_{max} and low rate (Table 4.1) its magnitude is small and relatively constant throughout the relevant energy range, with a value of $\sim$0.07 day^{-1}(100 ton)$^{-1}$ MeV^{-1}, at least an order of magnitude lower than the differential rate from the other solar ν species (Table 8.1).

Chapter 5

Physical Backgrounds

As discussed in Chapter 4, the signal from solar νs in Borexino is the energy spectrum of the elastically scattered electrons. To identify this signal, it is necessary for the rate of particle recoils from other sources to be smaller than those from solar νs in the energy region of interest, i.e. $<$10–100 $\mathrm{day}^{-1}(100\,\mathrm{ton})^{-1}\,\mathrm{MeV}^{-1}$ below 3 MeV. Decays from natural radioactivity are the same physical process that produces neutrinos in the Sun. Therefore, they emit particles with similar energies and thus are the most dangerous background for solar ν spectroscopy.

Radioactive decay is the spontaneous transmutation of an atom into another. The probability of any atom to transmute is constant over time and independent of any environmental factor. Therefore, a particular radioactive process may be characterized by the time it takes for half of the atoms in a large sample to decay, i.e. its half-life ($\tau_{1/2}$). The total mass difference between the initial and final atomic states corresponds to the total energy released in the process (Q-value).

Table 5.1 summarizes the most common radioactive processes. For the radioactivity of a particular isotope to be a potential background in Borexino, its half-life and abundance in the detector need to be such as to lead to a sufficiently large decay rate.

Type	Decay process	E_{dep} probability density =
α	${}^{m}_{n}\mathrm{C} \rightarrow {}^{m-4}_{n-2}\mathrm{A}^{2-} + {}^{4}\mathrm{He}^{2+} \rightarrow {}^{m-4}_{n-2}\mathrm{A} + {}^{4}\mathrm{He}$	$\delta(Q - E_{\mathrm{dep}})$
EC	${}^{m}_{n}\mathrm{C} \rightarrow {}^{m}_{n-1}\mathrm{B}^{*} + \nu_e \rightarrow {}^{m}_{n-1}\mathrm{B} + \nu_e$	$\delta(E_\gamma - E_{\mathrm{dep}})$
β^+	${}^{m}_{n}\mathrm{C} \rightarrow {}^{m}_{n-1}\mathrm{B}^{-} + e^{+} + \nu_e \rightarrow {}^{m}_{n-1}\mathrm{B} + \nu_e$	$\left\{ S^{m}_{n\mp1}(T)F(n, \pm e, T)K(Q', T) \right.$
β^-	${}^{m}_{n}\mathrm{C} \rightarrow {}^{m}_{n+1}\mathrm{D}^{+} + e^{-} + \bar{\nu}_e \rightarrow {}^{m}_{n+1}\mathrm{D} + \bar{\nu}_e$	$T = E_{\mathrm{dep}} - E_\gamma, Q' = Q - E_\gamma$

Table 5.1: The most common types of natural radioactivity. The initial, intermediate and final states are given in every case. The daughter nucleus in the intermediate state may be excited, promptly decaying to its ground nuclear state by electromagnetic processes, e.g. the emission of γ-rays. α decay and electron capture (EC) are two-body processes, in which the emitted particles are mono-energetic. Neutrinos are emitted in EC, β^+ and β^- decay modes and due to their very small interaction cross-sections do not deposit any energy in the target, i.e. their kinetic energy may be considered to be lost. As $\beta^\pm$ decay is a three-body process, the kinetic energy (T) spectrum of the emmitted $e^\pm$ is continuous. The spectrum (probability density) of the energy deposited in the target is given in the last column. Q is the difference in rest mass-energy between the initial and final states. E_γ is the energy, if any, emitted in the de-excitation of the daughter atom, and, in the case of β^+ decay, it also includes the energy released by e^+-e^- annihilation ($2m_ec^2$). The deposited energy from β^+ and β^- decay can be described by the same expression, where K is a statistical kinematic factor, and F is the coulomb factor, due to the electromagnetic repulsion (attraction) between the emitted e^+ (e^-) and the daughter nucleus. S is the shape factor for the particular decay, which is constant except for forbidden decays, where the emitted $e^\pm$ and neutrino carry non-zero orbital angular momentum. The deposited energy spectrum from $\beta^\pm$ decays will extend from E_γ to Q. Figure 5.1 gives examples of the energy spectra from $\beta^\pm$ decays observed in Borexino.

5.1 Primordial radioactivity

Certain radioactive isotopes produced in past supernovas, whose remnants are an important constituent of the Earth, have long enough half-lives to persist since the planet's formation, yet sufficiently short to lead to measurable radioactivity. These primordial isotopes have half-lives that are of the same scale as the age of the Solar System (Table 5.2). The dominant isotopes are ^{40}K, ^{232}Th and ^{238}U. The last two are the initial step in decay sequences of multiple isotopes (Figure 5.2) and, therefore, the total radioactive intensity induced by them is >10 times their individual decay rates.

As Borexino is constructed from materials that were extracted from the Earth's

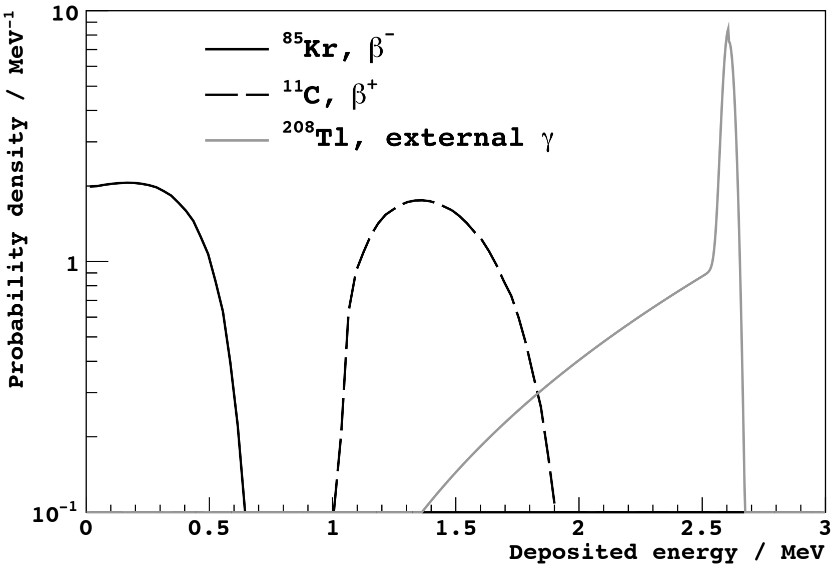

Figure 5.1: Characteristic deposited energy spectra of some backgrounds observed in Borexino. β emitters will deposit a range of energies, with the probability distribution given in Table 5.1. ^{85}Kr is a β^- synthetic isotope, whose Q-value (0.687 MeV) is close to T_{max} from ^{7}Be solar νs (Table 4.1). β^+ emitters, e.g. cosmogenic ^{11}C, will always deposit at least $2m_ec^2 = 1.022\,\text{MeV}$ from the e^+-e^- annihilation γ-rays, leading to the observed offset. Mono-energetic γ-rays produced by ^{208}Tl decays in the SSS and PMTs can deposit energy within the FV. As the attenuation length of γ-rays increases with increasing energy (Figure 5.4), γ-rays that have not lost any energy are the most penetrating, leading to the prominent full-energy peak at 2.615 MeV. The decreasing low-energy tail is due to those γ-rays that have lost some energy on their path to the active target.

crust, radioactivity from primordial isotopes is omnipresent. Thus, great care was taken in the selection of materials for the detector's construction and in the purification of the scintillator (Sections 3.1, 3.2 and 3.3). Radioactivity from these isotopes may be found within the scintillator or may be the source of γ-rays from the peripheral structure that penetrate into the active target[1] (Table 5.4). Even the flux of $\bar{\nu}_e$ produced by the decays of these isotopes in the Earth can be measured in Borexino [50].

---

[1] Charged particles emitted in radioactive decay, i.e. αs and βs, have ranges in scintillator that are <1 mm and ~cm, respectively, too small to constitute any background whose origin is external to the active target and IV.

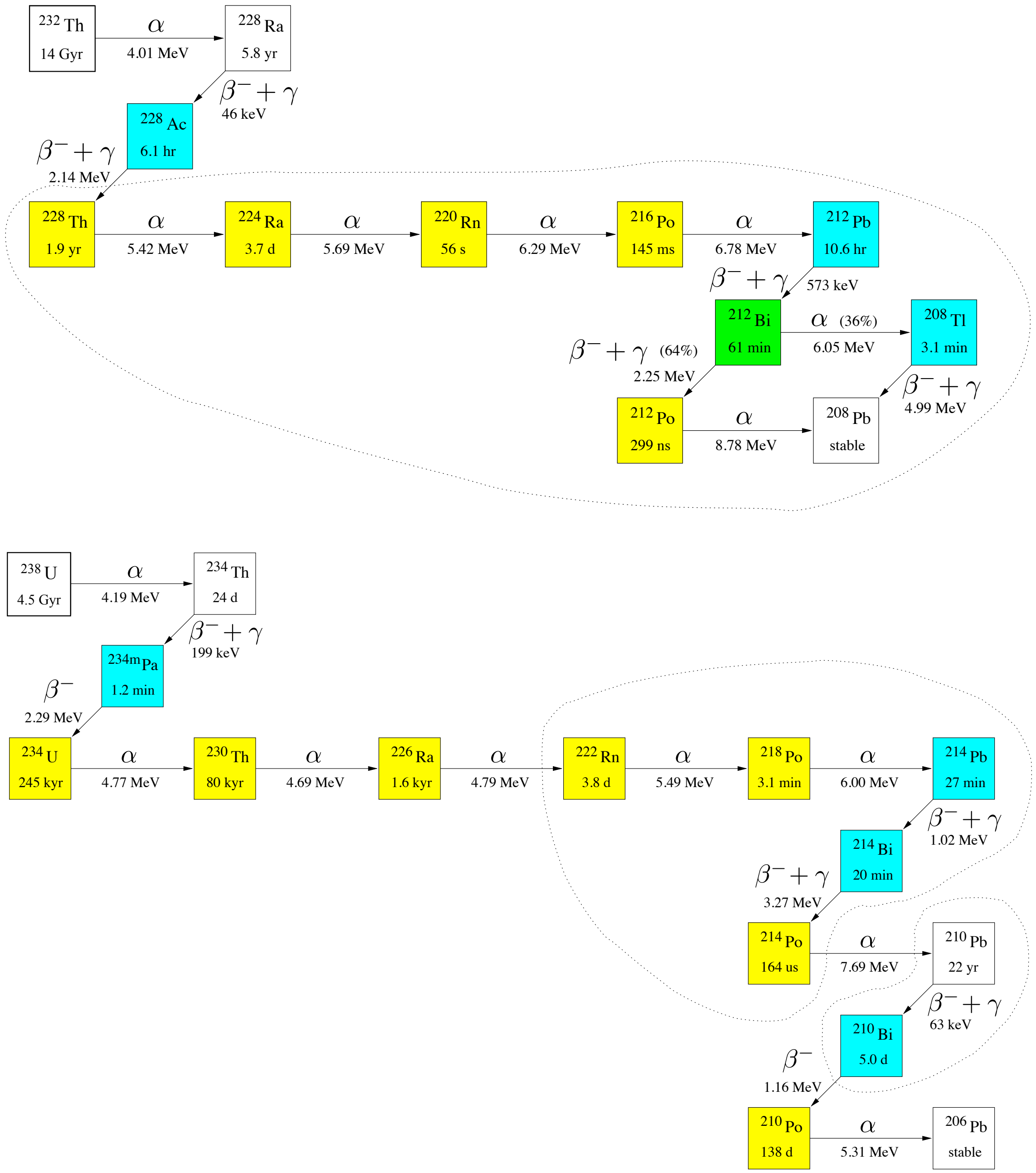

Figure 5.2: Radioactive decay chains of ^{232}Th and ^{238}U. Isotopes whose decay energy is below the analysis region are colored white. Energies shown are Q-values for β emitters (blue) and α kinetic energy for α emitters (yellow). Times shown are half-lives. Secular equilibrium is likely to hold only within the set of isotopes grouped by dotted lines. Adapted from Figures 3.9 and 3.13 in [11].

Isotope	$\frac{\tau_{1/2}}{\text{Gy}}$	Fraction of crustal mass / 10^{-6}	Decay intensity in the crust / Bq/kg	Decay intensity in BX / day^{-1}(100 ton)$^{-1}$
^{40}K	1.28	2.6	700	<0.4 (Table 9.1)
^{87}Rb	47.5	25	84	–
^{138}La	105	0.035	0.03	–
^{147}Sm	106	1.1	1.0	–
^{176}Lu	37.8	0.013	0.03	–
^{187}Re	43.5	4.4×10^{-4}	7×10^{-4}	–
^{232}Th	14.1	9.6	41	0.16±0.03 [5]
^{235}U	0.704	0.019	1.6	0.05±0.04 [5]
^{238}U	4.47	2.7	35	0.60±0.06 [87]

Table 5.2: Known isotopes with $\tau_{1/2}$ between 0.2 and 500 Gy (10^9 years). The third column shows the fractional contribution of the isotope to the mass of the Earth's crust [88]. These are the main sources of natural radioactivity that persist since the Earth's formation. ^{232}Th and ^{238}U are the first isotopes of long chains of successive decays (Figure 5.2). ^{40}K and ^{87}Rb decay to stable isotopes. The Q-value ^{40}K depends on its decay mode (1.31 MeV for β^- and 1.50 MeV for EC). Decays from ^{87}Rb (Q=0.28 MeV) are below the analysis threshold (0.3 MeV). The fourth column shows the average decay intensity in the crust. The last column shows the decay intensity in Borexino's scintillator after initial purification. For ^{232}Th, ^{238}U and ^{235}U, the estimates were obtained from counting time coincidences in the decay chain (Table 5.3) and assuming secular equilibrium. The limit on ^{40}K is a result of this analysis.

5.1.1 ^{232}Th, ^{238}U and ^{235}U

Figure 5.2 shows the segments of the ^{232}Th and ^{238}U decay chains that are expected to be in secular equilibrium, i.e. the decay rates in the target of all the isotopes in the segment are expected to be the same. This occurs when there is a set of isotopes whose abundance is dominated by radioactive decay, and whose production rate (determined by the decay rate of the heaviest isotope in secular equilibrium) is much smaller than their probability of decay ($\ln 2/\tau_{1/2}$).

As some isotopes in the decay chain have half-lives that are much smaller than the mean time between uncorrelated decays in the active target, the coincidence between the energy deposited by its decay and the decay of its parent can be identified with high efficiency. By measuring the rate of these time coincidences (Table 5.3), it is possible to obtain the decay rate of all isotopes that are expected to be in secular

Coincidence	Source	Type	$\tau_{1/2}$ ms	E_{prompt} MeV	E_{delay} MeV
^{214}Bi-^{214}Po	^{238}U, ^{222}Rn, ^{226}Ra	$(\beta^-\gamma)$-α	0.164	<3.27	*7.69*
^{220}Rn-^{216}Po	^{232}Th	α-α	145	*6.29*	*6.78*
^{212}Bi-^{212}Po	^{232}Th	$(\beta^-\gamma)$-α	2.99×10^{-4}	<2.25	*8.78*
^{219}Rn-^{215}Po	^{235}U	α-α	1.8	*6.82*	*7.39*
^{85}Kr-^{85m}Rb	0.43% of ^{85}Kr decays	β^--γ	1.01×10^{-3}	<0.173	0.514
e^+-n	$\bar{\nu}_e+p$	β^+-γ	0.177	$E_{\bar{\nu}_e}-0.782$	2.22

Table 5.3: Sequences (coincidences) that can be identified with high efficiency due to the time and space correlation between successive nuclear processes. From these we obtain samples of decays from different radioactive processes and with different energies. The energy deposited by α decays (in italics) produce considerably less light than β decays due to the lower scintillation efficiency (Section 6.5). In the first five cases, $\tau_{1/2}$ is set by the half-life of the second isotope in the sequence (Figure 5.2). The e^+-n coincidence is a product of interaction between $\bar{\nu}_e$ and protons in the target [50]. The produced e^+ will deposit its energy and annihilate with a bulk electron promptly, while the neutron will most likely react (capture) with ^{1}H in the scintillator, with a characteristic time $\tau_{1/2}$, to produce an excited state of ^{2}H, which decays by the emission of a 2.22 MeV γ-ray.

equilibrium with them, and to provide an estimate for the radioactive contamination in the target (Table 5.2). These studies suggest that the radioactivity in Borexino's scintillator from the isotopes in the decay chains of ^{232}Th and ^{235}U, and from those in the decay chain of ^{238}U before ^{222}Rn (whose chemical properties allow it to enter the active target through different mechanisms), are $<1\,\text{day}^{-1}(100\,\text{ton})^{-1}$, lower than the interaction rates from ^{7}Be, *pep* and CNO solar νs (Table 4.1). This conclusion is supported by an independent analysis of the α energy spectrum (Figure 6.17 of [11]).

5.1.2 ^{214}BiPo

The time coincidence between the decays of ^{214}Bi and ^{214}Po is useful for detector calibration. It is a product of ^{222}Rn, which is a gas that is constantly being emanated by materials due to contamination from ^{238}U and its daughters. As ^{222}Rn has a relatively long half-life, ^{214}BiPo coincidences are common ($>10^4$ in the IV over 3 y, Figure 3.10 in [11]) and distributed within the active target (Figure 3.11 in [11]).

^{214}Bi can β^- decay into many different excited states, producing a large variety

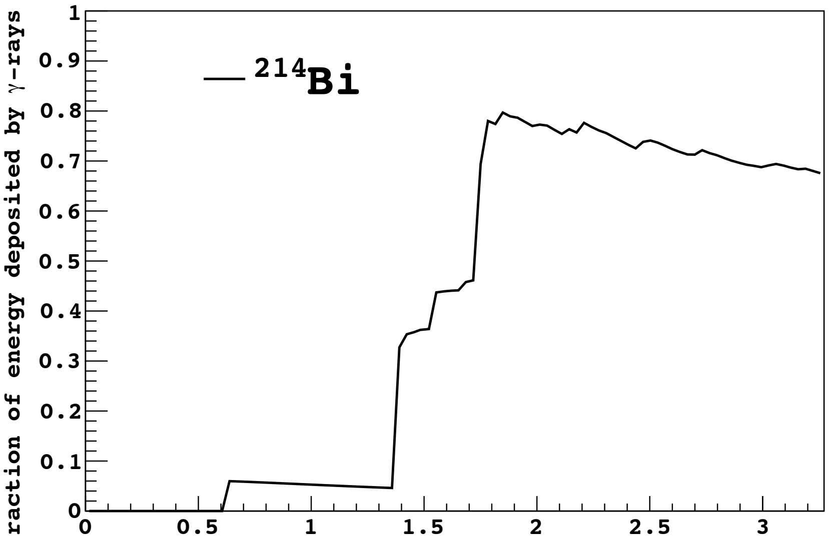

Figure 5.3: Average fraction of the energy deposited by ^{214}Bi decays in the active target that is deposited by the γ-rays from the de-excitation of the daughter nucleus. For deposited energy below 1.4 MeV, <5% of the energy is deposited by γ-rays. Therefore, low-energy ^{214}Bi decays are a sample of mostly pure β^- decays.

of γ-rays. For ^{214}Bi decays in the active target, the average fraction of the energy deposited by γ-rays depends on the total energy deposited from the decay (Figure 5.3). As ^{214}Bi is the most intense source of γ-rays from the ^{238}U chain, it is an important contributor to the external background from the peripheral structure (Table 5.4).

5.1.3 ^{210}Bi and ^{210}Po

^{210}Pb is an isotope in the ^{238}U decay chain whose half-life ($\tau_{1/2}$=22 y) is the longest of all the daughters of ^{222}Rn. As a material is exposed to ^{222}Rn, contamination from ^{210}Pb and its daughters, ^{210}Bi and ^{210}Po, remains[2]. In the case of liquids (e.g. the scintillator itself or the water used for its purification [39]), this leads to bulk contamination, while for solids (e.g. the nylon vessels or the liquid handling system), exposure to ^{222}Rn gas leads to surface contamination, which may then wash off into

---

[2] The Rn isotopes and their daughters produced in the ^{232}Th and ^{235}U decay chains are short-lived. Therefore, no significant radioactivity is expected in the target from them due to gas emanation or surface contamination.

the scintillator. As the ^{210}Bi half-life is considerably shorter than both ^{210}Pb's half-life and the timescale of the experiment, it is expected to be in secular equilibrium with ^{210}Pb, while ^{210}Po's half-life is long enough for it to be found out of secular equilibrium. The Q-value of ^{210}Pb (0.063 MeV) is below the detector threshold, but ^{210}Bi and ^{210}Po have proven to be two dominant backgrounds in the target ($>$10 day^{-1}(100 ton)$^{-1}$).

^{210}Bi decays by a forbidden β^- process with a Q-value of 1.16 MeV, which is close to the maximum kinetic energy of recoiling electrons from *pep* and CNO solar νs. Small differences in its spectral shape may have a large systematic effect in the extraction of the faint *pep* and CNO solar ν signals. Thus, special care was taken in understanding its spectral shape (Section 8.2.5 of [5]).

The spatial distribution of radioactive backgrounds that are introduced into the active target depends on their chemical form (e.g. in solution with the scintillator, as a particulate, etc.). Although the nature of ^{210}Pb in the detector is unknown, ^{210}Bi rates in the FV have increased throughout the data used for this analysis (Figure 6.25 in [11]), presumably introduced mostly from the top of the IV by detector operations. Therefore, the spatial distribution of ^{210}Bi decays is not expected to be constant nor uniform.

^{210}Po is the most prominent background of primordial origin in the scintillator. Its signal is a monoenergetic peak that falls in the neutrino energy region, due to the low scintillation efficiency of α decays (Section 6.5.3). Fortunately, as the scintillation time profile of αs is different from the one of electron recoils (Section 6.4.1), ^{210}Po can be effectively removed from the energy spectrum (Section 8.1). Both its time (Figure 3.8 in [11]) and space (Figures 12 and 13 in [89]) distributions have been highly unstable throughout the history of the experiment, as its decay rate is shorter than the time scale of the experiment and it is readily introduced into the active target by refilling operations.

Isotope	Source	F_γ	Highest energy γ		Highest intensity γ		Rate in FV day^{-1}
			E_γ / MeV	I_γ	E_γ / MeV	I_γ	
^{40}K	^{40}K	0.11	1.461	0.11	1.461	0.11	$\sim$0.5
^{60}Co	^{60}Co	1.00	2.505	2×10^{-8}	1.332+1.173	1.00	<0.1
^{208}Tl	^{232}Th	1.00	2.615	0.99	2.615	0.99	$\sim$10
^{212}Bi	^{232}Th	0.09	1.806	9×10^{-4}	0.727	0.07	–
^{214}Bi	^{238}U	0.82	3.270	6×10^{-7}	0.609	0.46	$\sim$10
^{228}Ac	^{232}Th	1.00	2.029	2×10^{-5}	0.911	0.26	–

Table 5.4: Greatest sources of external γ-rays. F_γ is the fraction of decays that emit γ-rays, while I_γ is the fraction of decays in which a particular γ-ray is emitted. ^{40}K decays by EC 11% of the time, with the emission of a γ-ray. ^{60}Co is a relatively short-lived ($\tau_{1/2}$=5.27 y) anthropogenic isotope commonly found in steel. The heavier isotopes are those from the ^{238}U and ^{232}Th decay chains that produce γ-rays with energies >1 MeV. As the extinction coefficient of γ-rays decreases with increasing energy (Figure 5.4), higher energy γ-rays are the dominant source of external background. The last column shows the expected rate in the FV from the dominant species, as obtained for Table 5 in [5] using the measured radioactive contamination of peripheral materials [53, 58]. A low rate (0.5±0.1 day^{-1} in the IV) of external γ-rays with energies >5 MeV has been observed (Section 4.3.1 of [90]), possibly from neutron captures in the peripheral structure. Figure 5.1 shows the deposited energy spectrum in Borexino's FV by an external mono-energetic γ-ray (^{208}Tl).

5.2 Anthropogenic radioactivity

Radioactive isotopes that are artificially produced by humans can be a source of background in Borexino. ^{60}Co, a γ-emitter (Table 5.4), was measured in the steel of the nylon vessel end-caps [53]. ^{137}Cs is the dominant isotope from nuclear fallout on the surface, which is relatively high near the laboratory following Chernobyl [92, 93]. Only one dust sample from Borexino's experimental hall in 2002 showed evidence of ^{137}Cs, at 2±1 Bq/kg, ~0.2% of the radioactivity from ^{40}K [94].

^{85}Kr (Figure 5.1, $\tau_{1/2}$=10.8 y) is a fission product that has been released by nuclear testing and power plans into the atmosphere, leading to a decay rate in air of 1 Bq/m^3 [95, 96]. It is efficiently removed from the scintillator by nitrogen stripping [39, 87]. Unfortunately, a small air leak during filling introduced a significant about of ^{85}Kr into the active target. Its rate in Borexino can be measured independently from the spectral analysis to be 30±5 day^{-1}(100 ton)$^{-1}$ [97], by relying on its unlikely decay

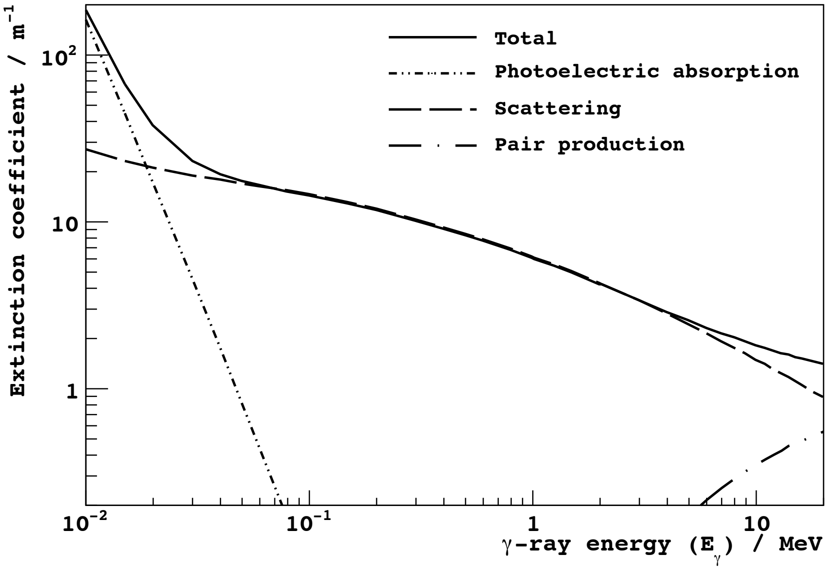

Figure 5.4: Extinction coefficient of γ-rays in Borexino's scintillator. The contributions from the different physical processes are shown. For the energy range of γ-rays from natural radioactivity (<3 MeV) and above the analysis threshold (0.3 MeV), Compton scattering dominates. The attenuation length is the inverse of the extinction coefficient. Values obtained from [91].

to an excited state of ^{85}Rb (Table 5.3).

The ^{85}Kr decay rate has been stable within the FV for the data used in this analysis (Figure 6.25 in [11]), consistent with the ^{85}Kr contamination occurring at filling, and suggesting that there has been no significant change in its spatial distribution.

5.3 Cosmogenic radioactivity

Cosmic rays can interact with nuclei in the atmosphere and produce radioactive isotopes. ^{39}Ar (Q=0.57 MeV, $\tau_{1/2}$=269 y) has an activity in air of 13 mBq/m^3 and should be removed efficiently by nitrogen stripping [98]. From the air leak that introduced ^{85}Kr, we expect 0.4 day^{-1}(100 ton)$^{-1}$ of ^{39}Ar in the active target.

^{14}C ($\tau_{1/2}$=5.7 ky, Q=0.16 MeV) is produced by cosmic ray interactions with nitrogen in the atmosphere, and through carbon dioxide it is absorbed into the Earth's biosphere, constituting 10^{-12} of carbon by mass. As PC is obtained from petroleum, which has been kept underground for millions of years, its ^{14}C content is much smaller, $\sim 3\times 10^{-18}$ of carbon by mass (the residual activity could be due to contamination from atmospheric carbon or nuclear processes underground [99, 100]). ^{14}C is chemically identical to ^{12}C, therefore the 40 Bq (100 ton)$^{-1}$ of background from ^{14}C cannot be removed from the scintillator by purification. This background dominates the detector's trigger rate and is the main source of event "pileup," where decays occur so close in time that they cannot be distinguished from one another (Section 3.2.2 of [11]). ^{14}C pileup has so far effectively set the low-energy limit of solar ν spectroscopy with Borexino at $\sim$0.3 MeV.

5.3.1 ^{12}C spallation

Cosmic rays may also produce radioactivity in the scintillator (Table 5.5), in particular from the spallation of ^{12}C nuclei, the dominant composite nuclear targets in the scintillator (Table 3.2)[3].

As the scintillator was exposed to the high muon flux at the surface for only 1–2 days [101], and was then purified underground [102], no significant background from ^{7}Be ($\tau_{1/2}$=53 d) was observed after detector filling. The activation of ^{10}Be is a much slower process due to its longer half-life ($\tau_{1/2}$=1.51$\times 10^{6}$ y) and, therefore, assuming no significant original ^{10}Be activity in the petroleum[4], we expect its decay rate at filling to be negligible. Still, there is a residual cosmic muon flux through Borexino (1.228$\pm$0.004 m^{-2}h^{-1} [104], $\bar{E}_\mu$=270$\pm$18 GeV [105]). As the spatial topology of muons (a track) is very different from radioactive decay, and they produce a very bright signal (they deposit $\sim$3 MeV cm^{-1} [106]), event selection cuts (Section 7.1) exclude unidentified muons with very high efficiency from the energy spectrum. Nevertheless, their

---

[3] The only possible nuclear transmutation of the ^{1}H nucleus (a single proton) is into a free neutron.

[4] The neutron energy threshold for ^{12}C(n,^{3}He)^{10}Be is $\sim$20 MeV [103], considerably larger than the energies of ns produced by radioactive decay in deep underground petroleum deposits. Therefore, ^{10}Be production in the petroleum should be dominated by cosmogenic neutrons, whose flux in the deposit should not be larger than in Borexino.

Isotope	Main production channel	Most probable visible process	$\frac{Q\ (E_\gamma)}{\text{MeV}}$	$\frac{\tau_{1/2}}{\text{s}}$	$\frac{\text{Visible decay rate}}{\text{day}^{-1}(100\,\text{ton})^{-1}}$
n	π^-+^{1}H, ^{12}C	^{1}H(n,γ)^{2}H	(2.22)	1.77×10^{-4}	90±10
^{12}N	^{12}C(p,n)	β^+	17.3	0.0110	0.06±0.01
^{13}B	^{13}C(n,p)	β^-	13.4	0.0174	*0.010±0.001*
^{12}B	^{12}C(n,p)	β^-	13.4	0.0202	1.41±0.04
^{8}He	^{12}C(π^-,$n3p$)	β^-	10.7	0.119	0.03±0.01
^{9}C	^{12}C(π^+,^{3}H)	β^+	16.5	0.127	0.10±0.03
^{9}Li	^{12}C(π^-,^{3}He)	$\beta^- n$	11.9	0.178	0.071±0.005
^{8}B	^{12}C(π^+,^{2}H^{2}H)	$\beta^+\alpha$	18.0	0.770	0.27±0.06
^{6}He	^{12}C(n,$2p^3$He)	β^-	3.51	0.807	*0.40±0.06*
^{8}Li	^{12}C(n,$p\alpha$)	$\beta^-\alpha$	16.0	1.21	0.40±0.07
^{11}Be	^{12}C(n,$2p$)	β^-	11.5	13.8	0.035±0.006
^{10}C	^{12}C(π^+,np)	$\beta^+\gamma$	3.65	19.3	0.54±0.04
^{11}C	^{12}C(γ,n)	β^+	1.98	1.22×10^3	28±5
^{7}Be	^{12}C(γ,$n\alpha$)	EC	(0.478)	4.60×10^6	*0.36±0.05*
^{10}Be	^{12}C(n,^{3}He)	β^-	0.556	4.77×10^{13}	$\ll$*1.5*

Table 5.5: Isotopes that are produced by cosmic ray muons and their hadronic showers in the active target and deposit energy. The second column gives the dominant production mechanism of the isotope, according to a FLUKA simulation (Table IV in [107]). The third column shows the main process by which the energy is deposited. For free ns this is capture on ^{1}H, while for the other isotopes it is radioactive decay. The fourth column shows either the Q-value of the dominant process or the energy of the emitted γ-ray. The last column shows the rate of all visible nuclear processes (this is also the isotope production rate, except for ^{7}Be, which only emits a γ-ray in 10.5% of decays, and ^{10}Be, whose production rate is only an upper limit on its decay rate, as its half-life is too long for equilibrium between production and decay rates to be achieved within the lifetime of the experiment). These values were extrapolated from the results of KamLAND [107], using the method proposed and validated in Section 4.2.4 of [90]. If no production yield was measured by KamLAND, we rely on their simulation results, and give the rates in italics. The extrapolation from measured rates are reliable within ~10%, while those from simulated yields may be off by a factor of 2–3. We note that the predicted n production rate is also consistent with the measured value of 89±4 day^{-1}(100 ton)$^{-1}$ [108].

interactions with nuclei in the active target produce radioactive isotopes (Table 5.5).

Most of these isotopes are relative short-lived ($\tau_{1/2}$<1 s) and have large Q-values (>10 MeV), leading to low differential count rates in the solar ν energy region that can be suppressed by discarding decays that occur a short period of time after muons cross the SSS.

We note the important role that free ns play in the production of these isotopes,

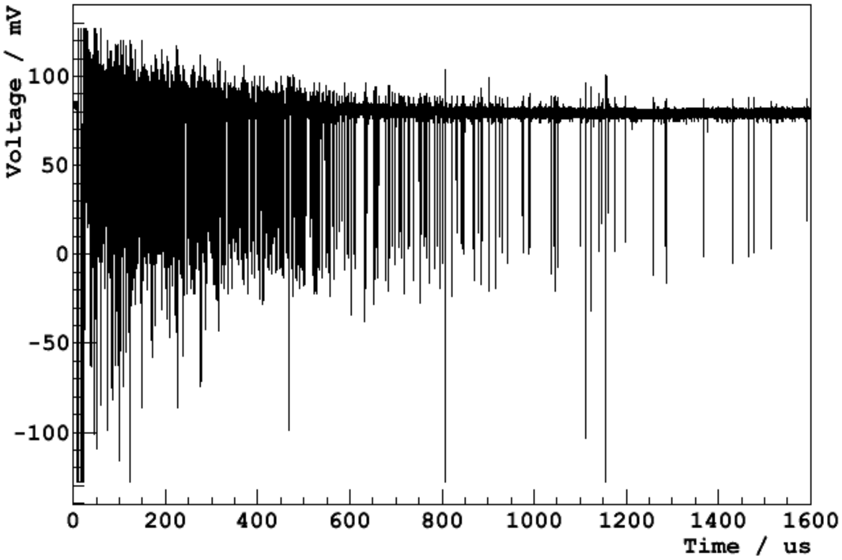

Figure 5.5: Digitized waveform by the 1-channel system (Section 3.5.1) of a muon and the subsequent captures of the ∼1375 ns it produced in the active target. The light signal produced by the muon is the first, large pulse on the far left of the window. Each spike below the baseline corresponds to the light from a γ-ray emitted by the excited nucleus after n-capture. Both captures on ^{1}H (E_γ=2.22 MeV), and ^{12}C (E_γ=4.95 MeV), which occur 0.9% of the time, can be seen. The characteristic $\tau_{1/2}$=177 μs of the process is evident from the decrease in the n-capture rate with increasing time after the muon.

often being either a reactant or a product in the production mechanism (Table 5.5). We have observed that a small fraction of the highest energy muons contribute significantly to n production (Section VI.B in [66], e.g. Figure 5.5), suggesting a correlation between cosmogenic signals, which may lead to production time distributions (e.g. Figure 20 in [109]) that deviate significantly from those of a Poisson process.

In the context of ns, cosmogenic isotope production has been argued to be distributed uniformly in space within the active target (Section V of [66]). This has been confirmed for the case of ^{11}C decays within 3 m of the center of the detector (Section 5.3.1 of [109]).

Decays from cosmogenic ^{11}C are problematic for *pep* and CNO solar ν spectroscopy, as the rate is ∼10 times higher than that of electron recoils from these νs, and its energy spectrum (Figure 5.1) overlaps with the end-point, a crucial feature, of the signal's spectrum. Furthermore, its half-life ($\tau_{1/2}$=20.4 min) is much longer than the average time between muons through the SSS (∼20 s), and therefore it is not possible to identify ^{11}C decays by relying on the time of muons alone. Strong correlation between ^{11}C and n production was first proposed in [110], and more detailed studies [111] showed that in interactions that produce 95% of ^{11}C, at least one n is also found in the final state. Thus, by relying on the identification of cosmogenic neutron captures in the scintillator, it is possible to suppress this background (Section 7.3).

Chapter 6

Event Reconstruction

The time profile of the charge output by the individual PMTs contains all the necessary information to reconstruct the time, position and energy of particle interactions in the detector.

A software package is used to interpret the raw data and run the algorithms to obtain the physical properties of the particle interactions. There are two sets of algorithms for event reconstruction, with independent event processing chains: *Echidna* and *MOE*[1]. Many steps in the event processing are very similar between the two, though there are certain important features that are unique to each set.

6.1 Hit reconstruction

In Section 3.5, we discussed the channel information that is stored in the raw data after every detector trigger. The first step in event reconstruction is to read the integrated charge and the time, relative to the trigger gate, of the firing of the channel discriminator, i.e. the PMT hit. This process is detailed in Section A.1 of [74] and in [112]. The hits corresponding to service triggers (Table 3.4) are used to evaluate the performance of the channel in time and charge measurement (Figure 3.8) and its

---

[1] This is the succesor of *Mach4*.

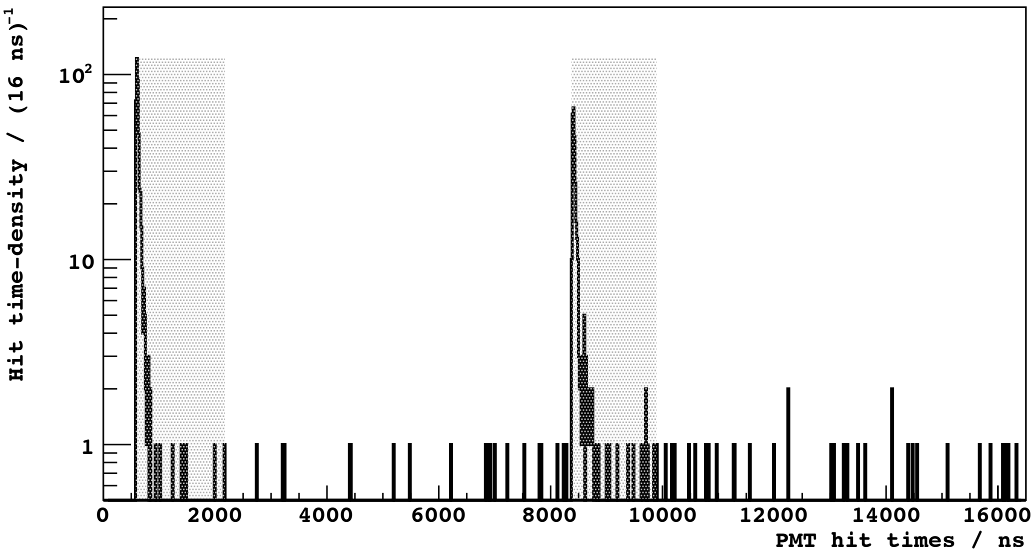

Figure 6.1: Decoded PMT hit times in the 16.5 μs ID trigger gate. Two scintillation pulses from the ^{214}BiPo decay sequence (Section 5.1.2) can be seen. The shaded gray regions are the identified clusters. Figure 6.2 shows the spatial distribution of the hit PMTs in the first cluster. The hits that do not belong to the clusters are most probably dark noise.

dark noise level. Hits that occur within a non-service trigger gate from channels that are regarded to have reliable timing information and low dark noise (Figure 3.8) are ordered in time and handed over to the clustering algorithm.

6.2 Clustering

Clustering is the process by which scintillation pulses in the active target are identified. The process relies on finding a cluster of hits in time within the trigger gate. The algorithm scans the trigger gate chronologically and identifies the regions where the time-density of hits is greater than some threshold. The cluster is this region plus some additional time after its end-point to assure that as many hits as possible that belong to the scintillation pulse are included. Figure 6.1 shows clustered events in a trigger gate.

Generally, it is required for there to be at least 20 hits in a cluster. In *MOE*, the length of the cluster is dependent on the total number of hits in it, with a length ranging from $\sim$0.7 μs to 2–3 μs. The value of the hit time-density threshold for clustering depends on the estimated dark noise rate in the trigger gate, which is different depending on the trigger type (Section 4.2 of [11]). If two interactions are too close in time ($<$0.25 μs apart) the algorithm cannot cluster them separately, leading to a single cluster with two scintillation pulses, i.e. pileup.

6.3 Position reconstruction

Once a cluster has been identified, we can consider the time of the hits and the position of the hit PMTs to reconstruct the position of the interaction. This is done by the "LNGS implementation" in *Echidna* of a time-of-flight subtraction algorithm [113].

Suppose that the interaction occurred at some position $\mathbf{r}_*$ and time t_* in the active target. For every hit time t_i, we may subtract the interaction time and the time it took light to travel from that point to the corresponding PMT, positioned at $\mathbf{r}_i$, to obtain the emission time of the detected photon relative to the interaction time:

$$t'_i = t_i - n_r \frac{|\mathbf{r}_i - \mathbf{r}_*|}{c} - t_* \tag{6.1}$$

We have assumed that light travels in a straight line from the interaction point to the light detector and that n_r is the effective index of refraction of the scintillator.

If we know the profile of the scintillation light, i.e. its probability density function relative to the interaction time, $P(t)$, we can compute the likelihood of the event occurring at $\mathbf{r}_*$ and t_*:

$$\mathcal{L}(\mathbf{r}_*, t_*) = \prod_{i=1}^{N_{\mathrm{hit}}} P(t'_i) \tag{6.2}$$

By finding the values for $\mathbf{r}_*$ and t_* for which $\mathcal{L}$ is maximum, we obtain, under the assumption that the hits are statistically independent, the most likely coordinates of

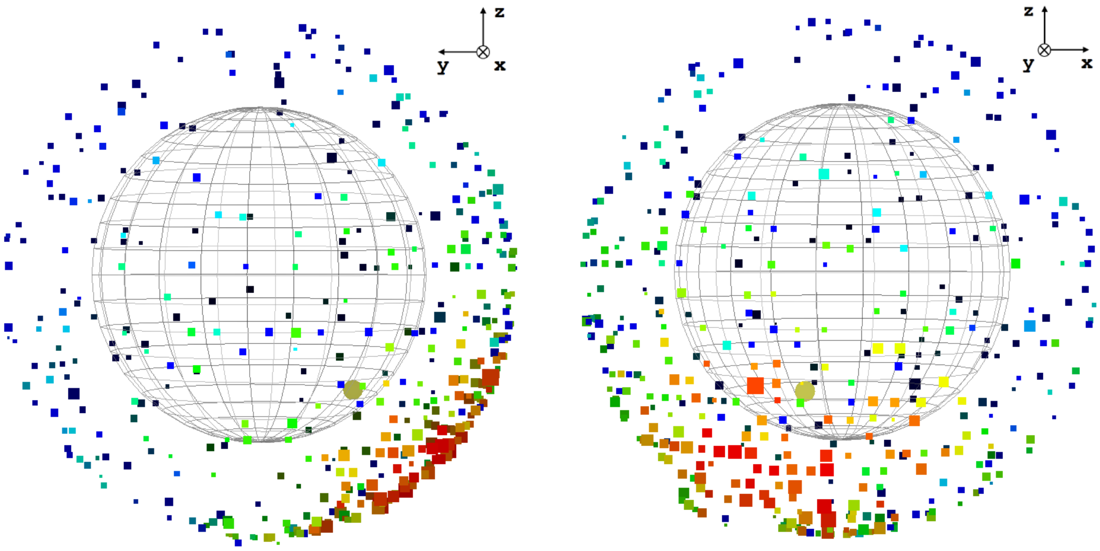

Figure 6.2: Distribution of the hits in the first cluster shown in Figure 6.1. The left image is the ID when viewed in the $\hat{\mathbf{x}}$ direction, while the right image is when viewed in the $\hat{\mathbf{y}}$ direction. The squares show the positions of the hit PMTs. The size of the square corresponds to the amount of charge output by the PMT. Red squares represent the earliest hits, while blue squares the latest. The yellow circle is the reconstructed position of the ^{214}Bi decay: (-1.24 m,-2.29 m,-2.75 m). The IV is shown for reference. Note that the earliest hits and the largest density of hit PMTs occur near the event position.

the interaction[2].

The fact that the electronics only record the time of the first pe produced by a PMT introduces an energy bias in the algorithm, as a channel's hit time probability distribution from a particular interaction position is dependent on the output number of pe: the larger the number of pe, the earlier, on average, the time of the hit. To tackle this problem, we have adopted in the computation of the likelihood (Equation 6.2) $P(t)$ distributions that depend on the charge of the hit (Figure 4.10 in [11], [114]).

n_r has been set to 1.68, by matching the reconstructed position of radioactive sources placed within the active target with the measured position by the camera system (Section 3.6). This value is significantly different than the measured refractive

---

[2] This can be regarded as an unbinned maximum likelihood fit to the scintillator's time profile, with $\mathbf{r}_*$ and t_* as the free parameters.

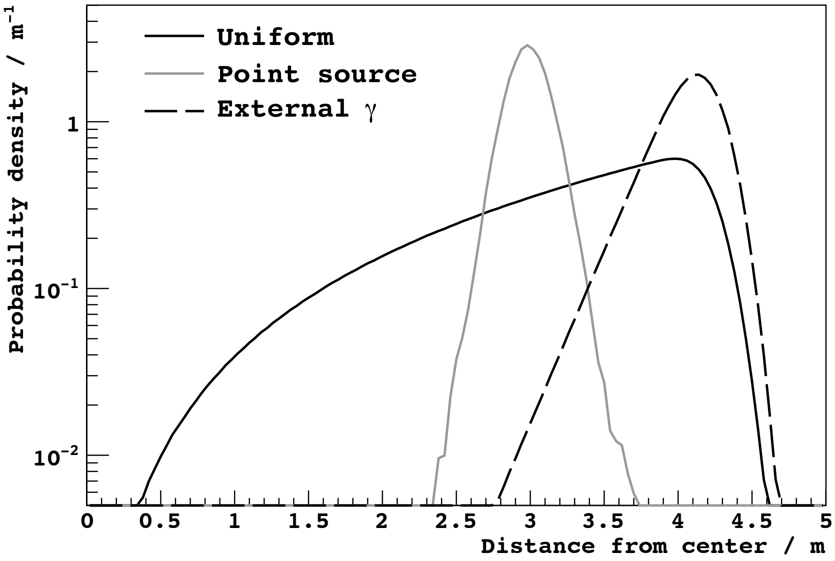

Figure 6.3: Reconstructed distance from the center of the detector by the time-of-flight subtraction algorithm for different event distributions. The point source corresponds to the acquired data when a ^{222}Rn source was placed at (0.05 m,-0.02 m,3.01 m) in the active target. The mean value of the distribution is within a few cm of the true source position, while the width of the distribution (∼14 cm) is the resolution of the algorithm (Figure 4.15 in [11], [114]). The uniform species (e.g. electron recoils from solar νs and cosmogenic isotope decays) and external γ-ray distributions are simulated, considering the algorithm resolution and a spherical active target of 4.25 m in radius. An attenuation length of 24 cm is assumed for the external γ-rays, which is evident on the left side of the distribution.

index of the scintillator and buffer fluids (Table 3.1). c/n_r has been found to be similar to the group velocity of scintillation light in the ID, which is smaller than its phase velocity due to the wavelength dependence of the refractive index [115].

After this tuning, the dominant bias in the time-of-flight subtraction algorithm is in the measurement of the **z** coordinate of an event [114, 115], for which it returns a value that is generally smaller (lower) than the position measured by the cameras. For radioactive sources placed ∼3 m from the center of the IV, this bias is -3±1 cm (Figure 8 in [114]).

Figure 6.3 shows some characteristic spatial distributions of radioactive species found in Borexino, as obtained by the position reconstruction algorithm.

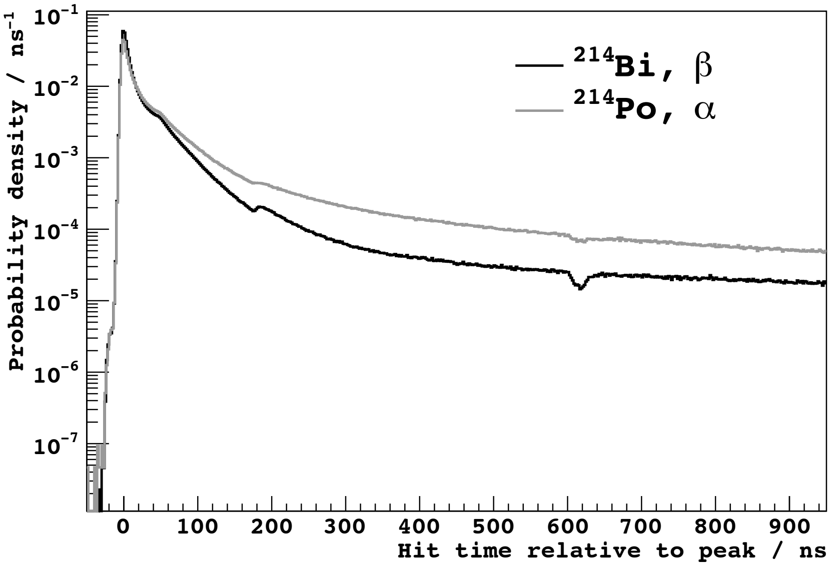

Figure 6.4: Average hit emission-time profiles, relative to the cluster peak, of ^{214}BiPo events less than 4 m from the center of the detector, selected by their correlation in reconstructed space and time (<0.6 m and 20–500 μs apart). Differences in the scintillation decay time between αs and βs are the basis for particle identification. The bump at 50 ns is due to light reflection on the SSS, while the one at 180 ns is due to the single channel dead time (Section 3.5). The dip at 615 ns arises from an over estimate in the number of hits originating from cable reflection (Section 2.2 of [112]).

6.4 Particle Identification

In the event processing chain, the array of the best-fit emission times of the hits is kept and certain characteristic parameters are calculated, in order to understand the nature of the interaction. The emission times are aligned relative to the "peak time", i.e. the point in the emission time array with the highest time-density of hits. Figure 6.4 shows the average emission time profile of scintillation clusters in the ^{214}BiPo decay sequence (Table 5.3).

6.4.1 α or e?

The differences between the scintillation time profiles of the particles are due to differences in the energy loss per unit path length (dE/dx) of the particle in the scintillator (Figure 6.8). With larger dE/dx the particle is more ionizing, leading to a larger fraction of scintillation photons that originate from excited molecules that arise from ion recombination. This process favors the production of excited molecules in a state that is likely to lose energy through a slower radiative process than the predominant state of the molecules produced by direct excitation [116].

To describe the αness (or $e$ness) of the interacting particle causing a clustered event, a Gatti parameter [117] can be constructed from the histogram of the hit emission-times:

$$G \equiv \frac{1}{N_{\text{hit}}} \sum_{i=0}^{N_{\text{bin}}} n_i \times w_i \tag{6.3}$$

The sum is over the product of the bin contents (n_i) and a weight,

$$w_i \equiv \frac{a_i - b_i}{a_i + b_i} \tag{6.4}$$

computed for the corresponding bin from the α and e emission-time reference histograms (Figure 6.4), whose bins we label a_i and b_i, respectively.

Figure 6.5 shows the G distributions of events in the ^{214}BiPo decay sequence. Positive G values correspond to α-like events (0.5% of ^{214}Po clusters have $G<0$), while negative values correspond to e-like events (0.1% of ^{214}Bi clusters have $G>0$).

6.4.2 e^+ or e^-?

As dE/dx between electrons and positrons is very similar, we do not expect any differences in the time profile of the photons arising from the deposition of the particle's kinetic energy. Nevertheless, differences in the time profile do exist due to the scintillation photons produced by the two annihilation 0.511 MeV γ-rays, following the formation of positronium [118], after the e^+ has deposited its kinetic energy.

Positronium (Ps) may be formed in either one of two states: para-positronium (pPs), where the e^- and the e^+ have antiparallel spins (S=0), or ortho-positronium

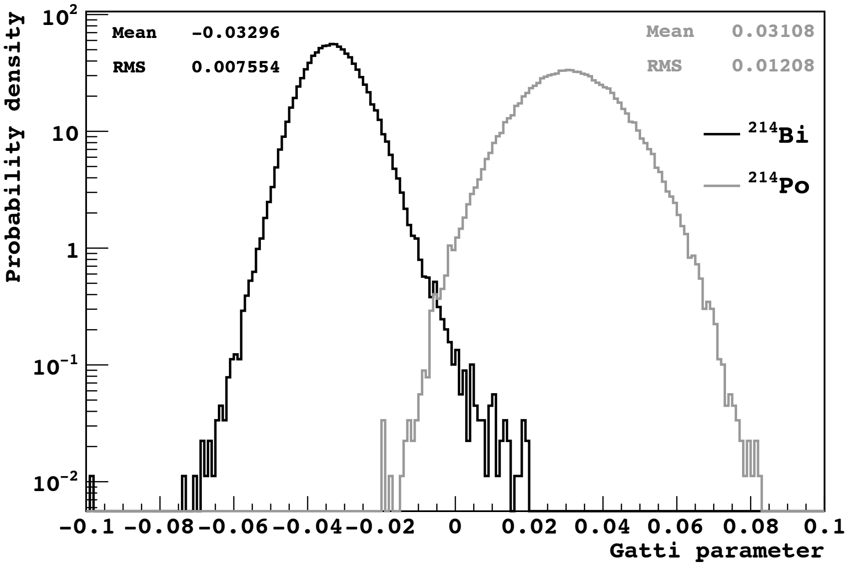

Figure 6.5: Gatti parameter (G) distributions of ^{214}Bi (e) and ^{214}Po (α) clusters, computed using Equation 6.3 and the reference time profiles shown in Figure 6.4. There is a selection cut of G<0.02 for ^{214}Bi clusters and G>-0.02 for ^{214}Po clusters.

(oPs), where the spins are parallel (S=1) [119]. pPs has a sub-ns half-life, while the oPs lives for a few nanoseconds in the scintillator before the e^+ annihilates with a bulk electron [120,121]. The delay between the scintillation pulse from the deposition of the e^+'s kinetic energy and the light from the annihilation γ-rays (Figure 6.6), as well as the topology of the back-to-back γ-rays' energy deposition, leads to slight differences in the average time profiles of the light produced by e^- and e^+ (Figure 10 in [5]). A fit to the time profile of the β^+ decay of ^{11}C with Monte Carlo-generated oPs and pPs time profiles (Figure 11 in [5]) suggest that ∼53% of the β^+ decays in the scintillator form oPs, with a half-life of ∼2 ns.

To develop a particle identification parameter to discriminate between e^- and e^+ (PS-BDT), we have used a Boosted Decision Tree (BDT) algorithm from *ROOT*'s Toolkit for Multivariate Analysis (TMVA) [122,123]. The method relies on optimizing a series of sequential cuts on a set of cluster variables to best separate a sample of known signal (e^-) events from a sample of known background (e^+) events.

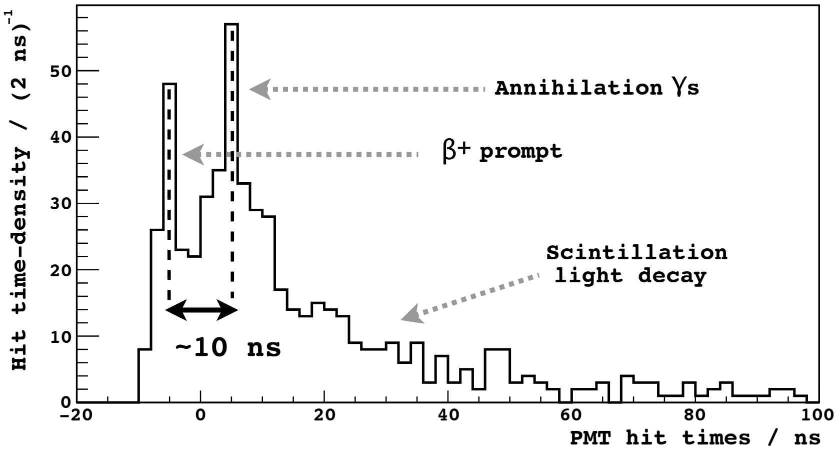

Figure 6.6: Hit emission-time profile of a β^+ decay, where the e^+ deposits its kinetic energy (first peak) and then forms ortho-positronium. The oPs exists for ∼10 ns before the e^+ annihilates with a bulk electron to produce γ-rays (second peak). Only half of β^+ decays produce oPs, whose half-life is ∼2 ns. Therefore, ∼1% of decays have a time separation between the energy deposits that is at least this long. In most decays the peaks overlap in time. The PS-BDT value (Figure 6.7) of this cluster is -0.44.

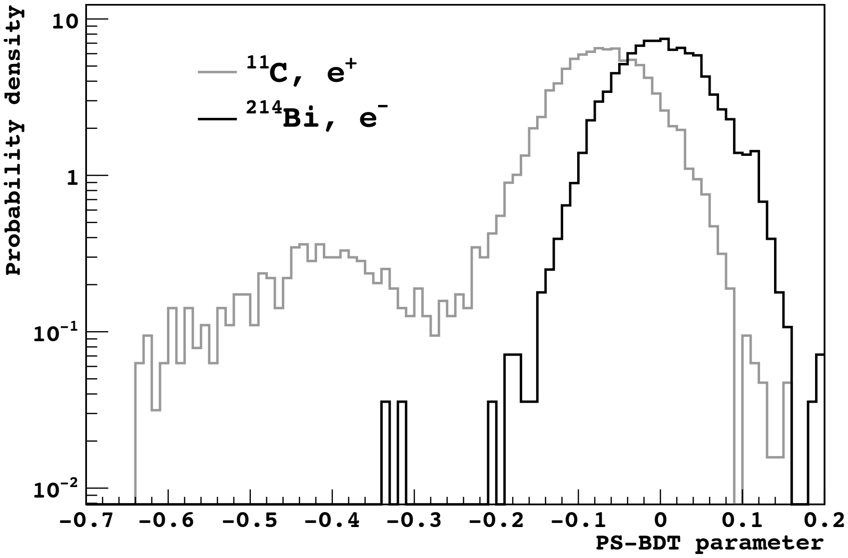

Figure 6.7: PS-BDT distributions of ^{11}C and low-energy (<1.8 MeV) ^{214}Bi events. The shift in the main peak position arises from differences in the topology of the energy depositions, due to the presence of two back-to-back γ-rays in β^+ decays. The tail toward negative PS-BDT values in the β^+ distribution is due to the formation of oPs. Generally, the larger the separation between the prompt and the delayed energy deposition (Figure 6.6), the more negative the value. The bump in the tail may arise from a sudden change in the discrimination efficiency of one of the considered variables once the energy depositions can be clearly distinguished in the hit-emission time profile.

The signal sample are ^{214}Bi decays with $E<1.8\,\mathrm{MeV}$, where the energy is predominantly deposited by the β^- (Figure 5.3). The background sample are β^+ decays of ^{11}C, selected by their space and time correlation with cosmogenic ns (Section 7.3). In both cases the selection criteria is independent on the scintillation time profile of the decay.

The cluster variables considered to construct the PS-BDT parameter include properties of the hit emission-time profiles (e.g. moments of the profiles and Gatti parameters), properties of the spatial distribution of the hits, and the uncertainties returned by the position reconstruction algorithm. A detailed description of the variables considered, and the characterization of the signal and background samples and the PS-BDT parameter may be found in Section 6.3 of [5]. Figure 6.7 shows the PS-BDT distributions of e^- and e^+.

6.5 Energy reconstruction

In Chapter 8 we will extract the solar ν interaction rates from the spectrum of the charge (q) cluster variable[3] of scintillation events. This is the addition of the charge, normalized by the channel's single photoelectron mean, of all hits in the cluster from channels whose charge measurement is considered to be reliable (Figure 3.8). The expected dark noise is subtracted from the total and the total is then multiplied by 2000 and divided by the number of considered channels.

To relate q to the energy of the clustered event, we need to find the relationship between i) q and the total number of photons emitted by the scintillator in the event and ii) the total number of photons emitted and the deposited energy in the active target.

A reasonable assumption is that the probability (a_i) that a scintillation photon emitted in the active target produces a photoelectron in a particular (ith) PMT is

---

[3] This is the `npe_no_avg_corrected` variable output by *MOE*.

only dependent on the coordinates $(\mathbf{r}, t)$ of the interaction[4]. As this probability is small ($a_i<10^{-4}$) and the number of photons emitted in an event is large ($N_\gamma>10^3$), the number of produced photoelectrons by a PMT can be well approximated by a Poisson distribution. As such, the probability that a channel registers at least one hit from a scintillation event (h_i) is

$$h_i = 1 - \exp\left[-a_i(\mathbf{r}, t)N_\gamma(E)\right] \tag{6.5}$$

For a particular radioactive point-source, h_i can be estimated by computing in what fraction of the clusters the channel registers at least one hit. Then, we can estimate the average number of photoelectrons per event (μ_i) detected by the channel:

$$\mu_i \equiv a_i(\mathbf{r}, t)N_\gamma(E) = -\ln\left[1 - h_i\right] \tag{6.6}$$

Using this expression, we have computed μ_i for every live channel for ^{85}Sr (0.514 MeV), ^{65}Zn (1.12 MeV) and ^{60}Co (1.17 MeV + 1.33 MeV) γ-ray sources[5]. These were placed at the center of the active target and at (0 m,0 m,±3 m) in June 2009. For every source and position, we normalized by the average of μ_i over all channels, i.e.

$$\frac{\mu_i}{\langle\mu_i\rangle} = \frac{a_i(\mathbf{r}, t)}{\langle a_i(\mathbf{r}, t)\rangle} \tag{6.7}$$

and showed that, for every channel, this quantity is independent of the energy of the source (the emitted number of photons) which is consistent with the model presented in Equation 6.5 (Slides 4–6 of [124]). A similar study comparing 2.22 MeV γ-rays from an ^{241}Am-^{9}Be n source between January, June and July 2009 demon-

---

[4] This is the assumption that the events are point-like, the photon emissions are directionally uncorrelated, and the directional profile of the scintillation light is independent of the physical properties of the interacting particle.

[5] At these energies, γ-rays have attenuation lengths (λ) of 10–20 cm. The closest PMT to any of the considered source positions is 3.5 m away, for which differences between the light collected from a point source at $\mathbf{r}$ and a diffuse source centered at $\mathbf{r}$ with λ=20 cm is <0.05%.

strated time variations of $a_i(\mathbf{r}, t)$ of at most 1% (Slides 7–9 of [124]). The spatial dependence of $a_i(\mathbf{r}, t)$ is expected, as a PMT subtends a different solid angle depending on the source position. Differences between PMTs are also due to the presence of the light concentrator and variations in quantum efficiency, channel threshold, etc. $a_i(\mathbf{r}, t)/\langle a_i(\mathbf{r}, t)\rangle$ distributions for different source positions are shown in Slide 16 of [124].

We may define N_{pe} as the average number of photoelectrons measured by 2000 channels[6] from a mono-energetic source at a particular position and time in the active target, which may be computed from the measured h_i:

$$N_{\text{pe}} \equiv 2000 \times \langle \mu_i \rangle = 2000 \times \langle a_i(\mathbf{r}, t)\rangle N_\gamma(E) \tag{6.8}$$

N_γ may be expressed in terms of the dominant contribution from scintillation photons and a small contribution from Cherenkov light[7]:

$$N_\gamma(E) = N_{\gamma\ \text{scint}}(E) + N_{\gamma\ \text{che}}(E) = L_\gamma \times E \times Q(E) + N_{\gamma\ \text{che}}(E) \tag{6.9}$$

As the scintillator response is, to first order, linear, we have summarized any non-linearity by a multiplicative unitless quenching term ($Q(E)$). Finally, we may conveniently express the estimated number of photoelectrons as

$$N_{\text{pe}} = L_{\text{pe}}(\mathbf{r}, t) \times E \times Q(E) + N_{\text{che}}(E, \mathbf{r}, t) \tag{6.10}$$

where the position and time dependence of the scintillation light is contained in the photoelectron yield L_{pe}.

In addition to the γ-ray sources ^{85}Sr, ^{65}Zn and ^{60}Co, and the 2.22 MeV n capture

---

[6] With the same spatial distribution as the considered channels.

[7] Most of the emitted Cherenkov light will be absorbed by the scintillator and re-emitted isotropically at longer wavelengths (Table 3.1).

γ-ray, we have also measured N_{pe} for ^{203}Hg (0.279 MeV), ^{54}Mn (0.835 MeV) and ^{40}K (1.46 MeV) γ-ray sources. These were all deployed in the active target in June 2009.

6.5.1 Quenching model

Birks quenching model [125] is based on the assumption that the number of excited scintillating molecules and the number of ionized molecules produced per unit path length by an interacting particle is proportional to dE/dx. Additionally, it considers the possibility that the excited molecules may interact with the ionized ("damaged") molecules and lose their energy non-radiatively [126]. For large dE/dx, the local concentration of excited and ionized molecules along the particle path is larger, making interactions between them more likely and consequently decreasing the light output per deposited dE.

In this model, the quenching term in Equation 6.10 may be expressed as

$$Q(E, kB) = \frac{1}{E}\int_0^E \frac{dE'}{1 + kB\,\frac{dE}{dx}(E')} \tag{6.11}$$

where dE/dx is a function of the remaining kinetic energy of the particle along its path (E') and depends on the particle type (Figure 6.8). E is the total energy deposited, i.e. the initial kinetic energy of the particle. kB is a constant that depends on the material of the target and cannot be estimated from first principles.

For the case of γ-rays, the energy is not directly deposited by the primary particle but by a sequence of electron recoils produced mostly from Compton scattering (Figure 5.4). Thus, we may compute an average quenching factor

$$Q_\gamma(E_\gamma, kB) = \frac{1}{E_\gamma}\left\langle \sum_j E_j \times Q_e(E_j, kB) \right\rangle \tag{6.12}$$

where the average is over a large sample of Monte Carlo-generated γ-ray events,

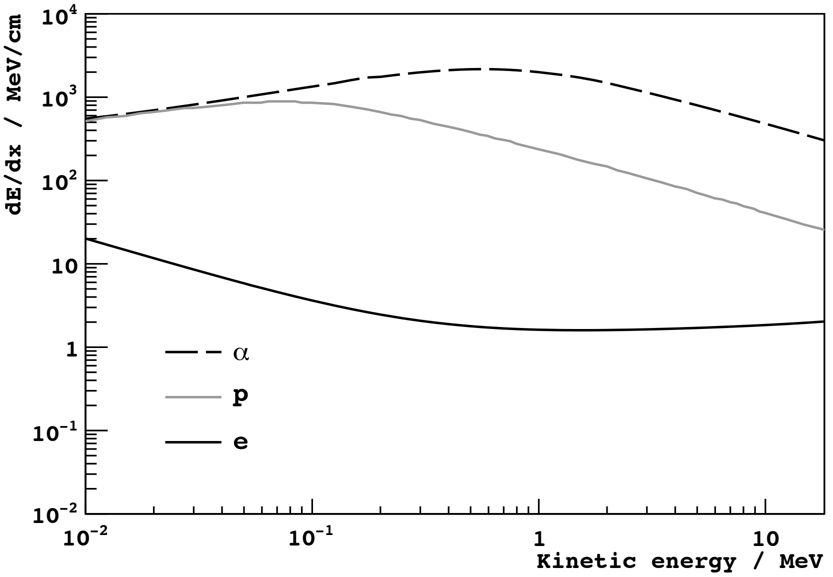

Figure 6.8: Energy loss per unit path length of organic scintillator as a function of kinetic energy for different charged particles. The values are those for toluene obtained from [127] and scaled to PC's mass density. In this work we generally assume dE/dx for e^+ to be the same as for e^-, although small differences exist [128].

for each of which we have added the corresponding quenched energy of every (jth) recoil electron (Section 3.1.2 of [90][8]). The computation was performed for a wide range of kB values using [129]. Uncertainties in dE/dx for low energy electron recoils (<10 keV) [130, 131] were found to have a negligible effect on Q_γ.

6.5.2 γ-ray calibration

To calibrate the energy scale of Borexino's scintillator, we can perform a fit to the measured N_{pe} (Equation 6.8) for the different γ-ray lines using Equation 6.10. For this, we have fixed the contribution from Cherenkov light to that obtained from Borexino's full Monte Carlo simulation, *g4bx* (Figure 4 in [90])[9], and left the photoelectron yield

---

[8] The procedure outlined in this reference is the one adopted in this analysis, although the final results are different as the quenching function in [90] was extracted from a fit to q directly, which was later found to include non-linearities introduced by the electronics (Section 4.2 of [89]). Thus, we adopt the energy variable definition and the energy scale calibration results from Section 4 of [89].

[9] As the Cherenkov contribution to the total number of photoelectrons is <1% in the energy region relevant to this analysis, our result should be insensitive to the small uncertainties of the Monte Carlo.

(L_{pe}) and kB as free parameters. The results are shown in Figure 6.9.

Comparisons between N_{pe} for γ-ray lines at different positions suggest that our result for kB is position independent (Figure 9 in [89]). These parameters also correctly predict N_{pe} for the γ-ray line from the decay of ^{60}Co (Table 8 in [89]).

Ideally, the cluster charge variable (q), which we use as our energy estimator, should be the same as number of photoelectrons measured in the cluster. Unfortunately, this variable is susceptible to electronics effects, e.g. bad channel normalization, single channel dead time, PMT after-pulses, integrator saturation, etc. Therefore, we chose to characterize q by considering the mean of its distribution ($\langle q \rangle$) for γ-ray lines for which we have measured N_{pe} (Section 4.2 of [89]). Generally, $\langle q \rangle$ is 4–5% larger than N_{pe} (Figure 11 in [89]), although the precise relationship is dependent on both its magnitude and the source position.

We can approximate the relationship between $\langle q \rangle$ and N_{pe} as

$$\frac{\langle q \rangle}{N_{\mathrm{pe}}} = 1 + a + bN_{\mathrm{pe}} \tag{6.13}$$

where the resulting values are a=0.05 and b=$-1.25 \times 10^{-5}\,\mathrm{pe}^{-1}$ for sources at the center of the active target (Figure 10 in [89]). The non-zero value for b demonstrates a non-linearity in the energy scale introduced by the electronics in the measurement of q.

With a model to obtain N_{pe} from the particle's kinetic energy and $\langle q \rangle$ from N_{pe}, we can relate our estimator (q) to the energy of the particle:

$$\langle q \rangle = L_{\mathrm{pe}}(\mathbf{r}, t) \times Q_{\mathrm{eff}}(E, \mathbf{r}, t) \times E \tag{6.14}$$

Q_{eff} is an “effective” quenching factor that includes, in addition to the non-linearity of the scintillation process, the non-linearities introduced by Cherenkov radiation and the electronics. Due to the latter, this term is now slightly dependent on the

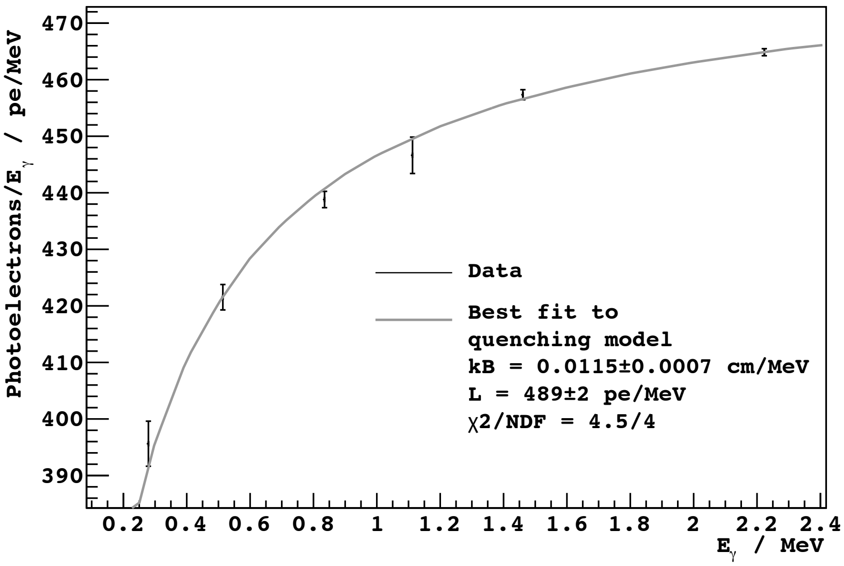

Figure 6.9: Result of a fit to the measured $N_{\rm pe}$ with Equation 6.10. The γ-ray lines considered are those from the decays of ^{203}Hg, ^{85}Sr, ^{54}Mn, ^{65}Zn and ^{40}K, and the 2.22 MeV γ-ray from n capture. The measured kB is related to the physical properties of Borexino's scintillator, while $L_{\rm pe}$ corresponds to its value at the center of the detector in June 2009.

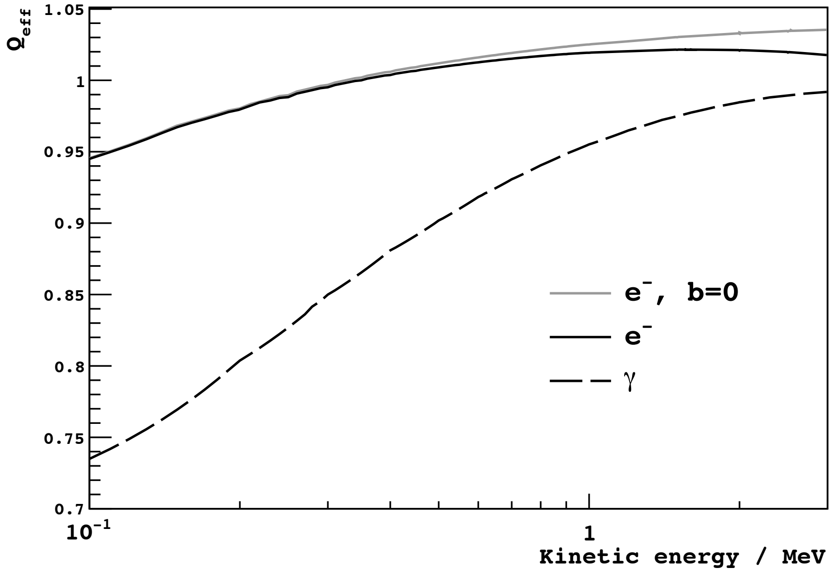

Figure 6.10: Effective quenching factor (Equation 6.14) for electrons (or positrons) and γ-rays. The black lines show the measured value at the center of the active target. The gray line is $Q_{\rm eff}$ for the case where the non-linearity in q due to the electronics is ignored (b=0 in Equation 6.13). Coincidentally, this is very similar to the form of $Q_{\rm eff}$ at (0 m,0 m,3 m) (Figure 11 in [89]).

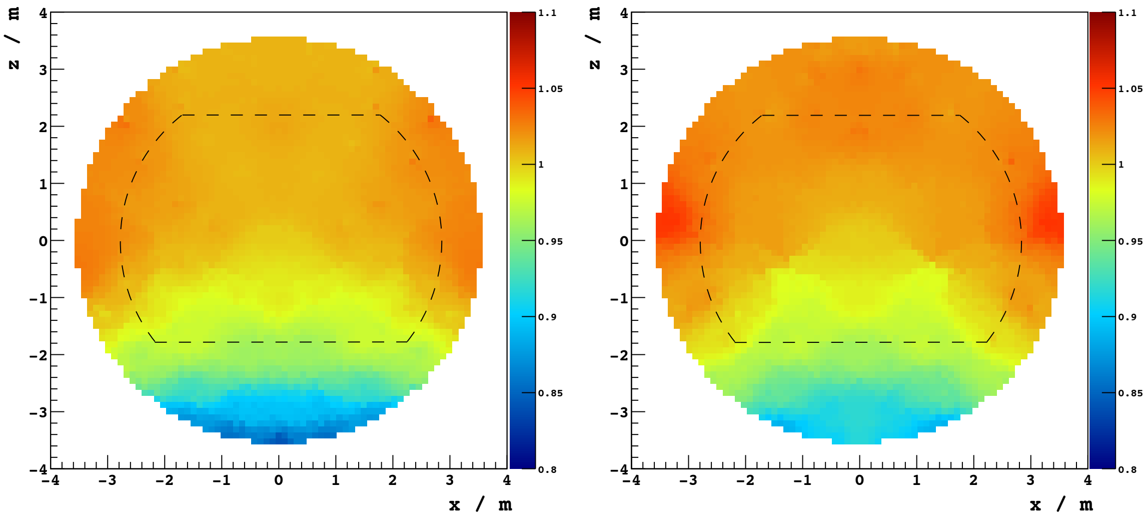

Figure 6.11: L_{pe} values relative to the center within the active target (color axis), as determined from the α decay of ^{214}Po in source calibration data. Values between source positions are determined using an inverse-distance weighted interpolation assuming azimuthal symmetry. The cross-section of the FV (Section 7.2) is shown with a dashed line. Left: Jan-Feb 2009 calibration campaign (Runs 9458 - 9615). Right: June 2009 calibration campaign (Runs 10301 - 10391). This is Figure 5.13 in [11].

coordinates of the event. Figure 6.10 shows Q_{eff} for electrons and γ-rays.

The position dependence of L_{pe}, which is independent of the particle type, can be mapped using ^{222}Rn source calibration data (Figure 6.11). The time dependence of L_{pe} throughout the history of the detector is hard to track, although studies on $\langle q \rangle$ of ^{210}Po contamination in the active target (Figure 5.14 in [11]) suggest possible changes in L_{pe} associated with the filling of the detector with pure PC.

6.5.3 α energy scale

As the solar ν signal is extracted from the spectrum of β-like events, the requirements in the precision of the calibration of the energy scale of α particles is not particularly stringent.

It has been found that the energy response of highly-ionizing nuclear recoils in liquid scintillators (e.g. p, α and ^{12}C) [132, 133] is not well described by Birk's model

(Equation 6.11). For the case of Borexino, a linear fit to $\langle q \rangle$ as a function of energy for α lines from ^{222}Rn source calibration and radioactive contamination in the active target was found to be an adequate description of the energy scale (Section 3.1.3 in [90]). The latest result from an updated analysis (Section 5.2.4 in [11]) yields

$$\langle q \rangle = 89.31\,\frac{\mathrm{pe}}{\mathrm{MeV}} \times E_\alpha - 264.67\,\mathrm{pe} \tag{6.15}$$

where this result applies to a uniform source distribution within 3 m of the center of the active target and for α particle kinetic energies (E_α) in the 5–9 MeV range.

6.6 Muon track reconstruction

For events that coincide with the MTB trigger (Table 3.4) or that correspond to bright signals in the inner detector, the reconstruction of a muon track is attempted. Similarly to the position reconstruction of point-like events (Section 6.3), the procedure relies on finding the muon track which is most likely to produce the observed pattern of the hit times, considering that in the ID light is produced isotropically at every point along the muon track[10]. In the *Echidna* framework, both the hit information from the OD and ID is used (Section 4.1 of [51]), while in *MOE* only the ID information is considered (Section 5.1 of [109] and Section 4.6 of [11]).

Generally, the resolution on the direction of the muon track (i.e. the angle between the reconstructed track and the true track) is 2°–3°, and the resolution on the impact parameter about the center of the active target is 30–40 cm (Table 4 in [51]), with no observable systematic bias (Figure 11 in [109]). Figure 6.12 shows an example of the hit pattern produced by a muon and the corresponding reconstructed track.

---

[10] The inclusion of Cherenkov light has no effect on the algorithm, as the Cherenkov light coincides with the wavefront of the scintillation light in the forward direction.

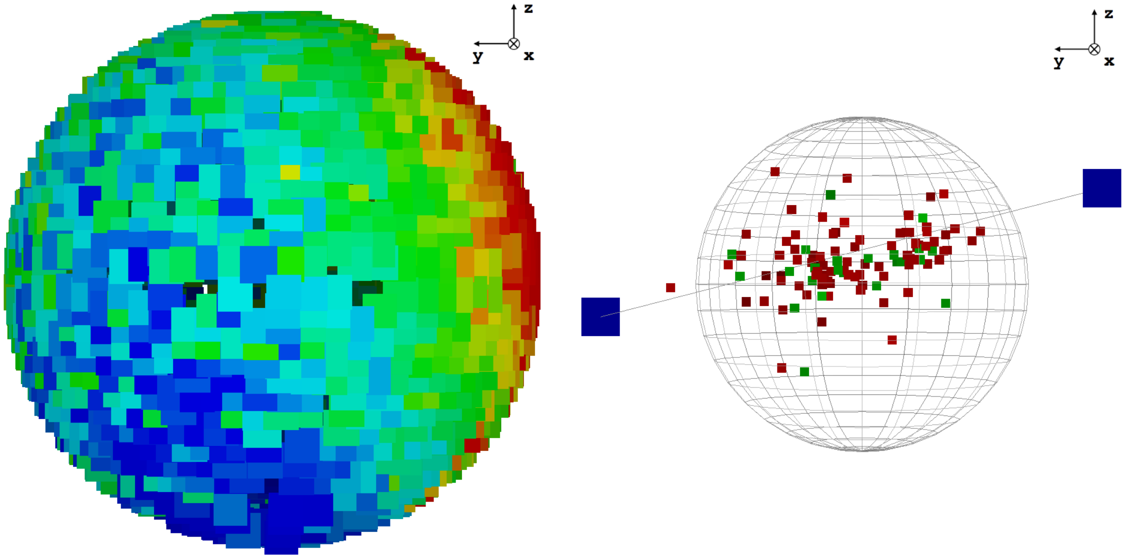

Figure 6.12: Left: Distribution of the hits from a muon event. Almost every live PMT in the detector (squares) registers at least one hit. Red squares represent the earliest hits, while blue squares the latest. Right: The blue squares are the muon entry and exit points on the SSS, as reconstructed by *MOE*. The entry point is on the right of the figure, coinciding with the cluster of early hits on the SSS. The red squares are the reconstructed position of n capture γ-rays less than 2 ms after the muon, while the green squares are the reconstructed positions of events in the ^{11}C energy region (1–2 MeV, Figure 5.1) less than 2 h after the muon. The IV is shown for reference.

Chapter 7

Event Selection

For this analysis we will consider a subset of the validated data used for the published result on the ^{7}Be ν interaction rate (Section 1 of [89]). We have excluded Period 1, for which the extended data acquisition window after trigger 128 (Table 3.4), essential for detecting cosmogenic ns, had not been implemented.

Table 7.1 shows the dates and corresponding live time for the data periods. For reference, the version of the processed data used in this analysis is labeled `cycle12m97`.

Period	Start week	End week	Start run	End run	Live time / days
2	13 Jan 2008	01 Jun 2008	6898	7937	127.292
3	08 Jun 2008	05 Oct 2008	7938	8791	99.082
4	05 Oct 2008	11 Jan 2009	8910	9451	73.728
5	08 Feb 2009	14 Jun 2009	9713	10297	84.041
5a	28 Jun 2009	12 Jul 2009	10497	10545	9.017
6	26 Jul 2009	25 Oct 2009	10750	11517	74.005
7	01 Nov 2009	24 Jan 2010	11518	12400	72.648
8	14 Feb 2010	2 May 2010	12489	12940	68.463
Total	13 Jan 2008	2 May 2010	6898	12940	608.276

Table 7.1: Division of data into different periods. The live time presented in the last column is before any analysis cuts.

7.1 Selecting solar ν candidate events

To extract the solar ν signal from the event q spectrum (Chapter 8), it is necessary that only backgrounds whose spectra have been characterized are found in the final sample of events. Section 2.3 of [89] shows the list (1–14)[1] of the data selection criteria before ^{11}C suppression (Section 7.3). These cuts may be grouped according to the events that they are meant to reject:

- Events that are not caused by scintillation light in the active target (e.g. electronic noise). This includes noise in the trigger following a cosmic muon (1), high-frequency noise that leads to multiple clusters within a single trigger gate (5, 12), events where most of the hits are recorded by a single DAQ rack (7, Section 4.7.1 of [11]), and events where the spatial distribution of the hits (10, 11, Section 4.7.2 of [11]) or the output-charge distribution of the working channels (13, 14) is inconsistent with isotropic scintillation light.
- Scintillation events that are not point-like (i.e. cosmic muons) (1). We consider coinciding signals in the OD and the hit time distribution in the ID.
- Cosmogenic isotope decays (Table 5.5) less than 0.3 s after a muon (1, 4).
- Decay sequences (Table 5.3) that are less than 2 ms apart (3, 5).

Of these, the time veto after every identified muon leads to the largest loss of live time (1.8%, Table 5 of [89]). Other minor live time corrections and a study of the probability that a valid solar ν candidate is misidentified by these criteria can be found in Sections 2.5 of [89] and Section 6.2.3.1 of [11], respectively.

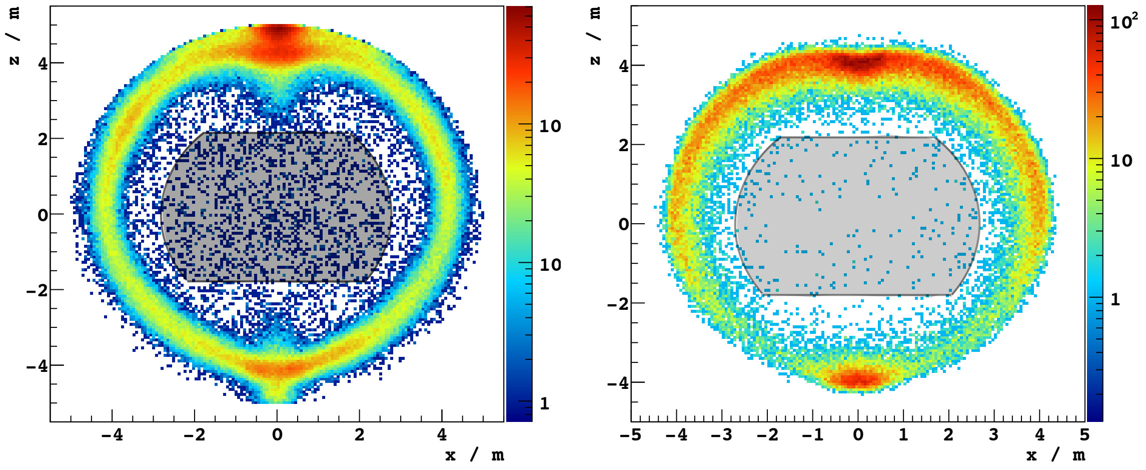

Figure 7.1: Spatial density distributions (color axis) of events with reconstructed position -1 m<y<1 m in two different energy regions. The cross-section of the FV is shown for reference. Left: Events with 120 pe<q<145 pe where an excess of events away from the end caps (z=±4.25 m) toward the center of the detector is evident. These are presumably decays from radioactive material in the end caps that are degraded in energy due to a shadowing effect. As the light traveling toward the end cap is lost (or partially reflected) the position reconstruction is biased inward, leading to a source of background whose spectral shape is hard to model and, therefore, needs to be excluded from the FV. Right: Events with 900 pe<q<1500 pe. These are mostly γ-rays from the peripheral structure. Note the decreasing density toward the center of the active target. Compare to the corresponding distribution in Figure 6.3.

7.2 Fiducial volume definition

Criteria 8 and 9 are spatial cuts to select decays inside the FV, the largest possible region in the active target where:

- γ-ray background from the PMTs, SSS and nylon vessels is significantly reduced by self-shielding.
- The performance of the ^{11}C suppression (Section 7.3) is best (distance from center of the detector, r<2.8 m).
- The contribution from events whose position is misreconstructed due to shadowing by the vessel end caps is negligible (z<2.2 m).

---

[1] Criteria 15 and 16 are not applied in this analysis.

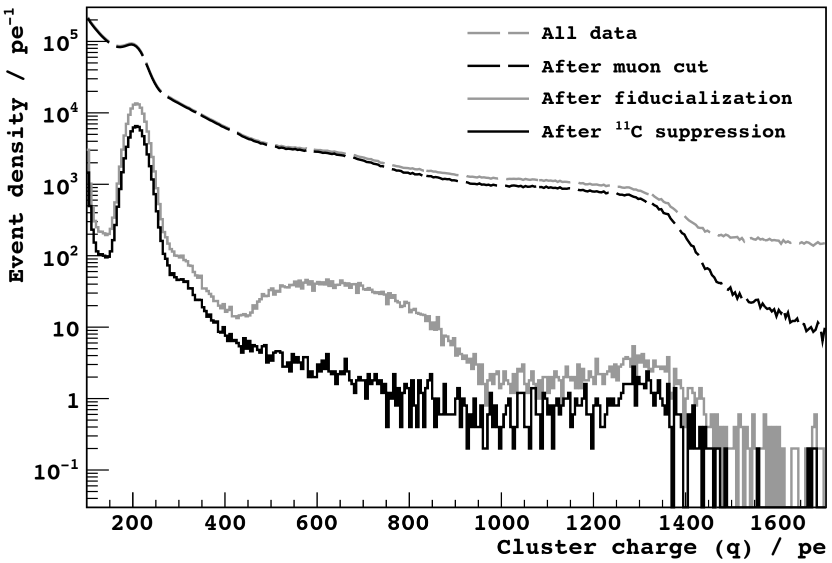

Figure 7.2: Borexino's charge spectrum after the sequence of event selection cuts. The cuts shown are the only ones to have a visually evident effect on the spectral shape. The dashed black line is after cosmic muons and events less than 0.3 s after them are removed. As the muon and short-lived cosmogenic isotope signals are bright (Table 5.5), the change in the spectral shape is mostly at large q. Selecting events within the FV (gray solid line) removes external γ-ray background, which dominates the entire spectrum. The solid black line shows the spectrum after ^{11}C background is suppressed by relying on its correlation in space and time with cosmogenic ns (Section 7.3). The prominent peak at ~210 pe is due to the α decay of ^{210}Po contamination in the target, which will be removed from the spectrum by a statistical technique (Section 8.1).

- L_{pe} is constant enough throughout the volume such that the charge resolution can be adequately modeled by the empirical approximation given in Equation 8.2 (z>-1.8 m).

Figure 7.1 shows the spatial distribution of events in two q ranges, to illustrate the first and third considerations above. L_{pe} variations within the FV are ±5% (Figure 6.11), leading to a contribution to the total variance in the detector's charge response that is <10% (Section 4.2.2 of [5]).

The scintillator volume within this region is $81.3^{+0.9}_{-0.5}\,\mathrm{m}^3$, corresponding to a mass of $71.5^{+0.8}_{-0.4}$ ton. The uncertainty has been obtained as in [115].

7.3 ^{11}C suppression

As discussed in Section 5.3.1, there is a three-fold coincidence (TFC) between the signals from muons, cosmogenic ns and ^{11}C decays in the active target (Figure 6.12). In the context of underground organic scintillator detectors, this correlation was first studied in CTF [134].

We have performed time and space vetoes following the detection of cosmogenic ns to preferentially reject regions of the active target that are more likely to contain ^{11}C decays, leading to a lower ^{11}C decay rate. The geometry of the veto is dependent on several factors:

- If a γ-ray from n capture is identified and its reconstructed position is considered to be reliable[2], all events occurring within 1 m and 2 h of the reconstructed coordinates are rejected.
- Moreover, events occurring within 1 m and 2 h of the closest point on the parent muon track from the reconstructed γ-ray position are also rejected.
- If at least one of the identified γ-rays does not have reliably reconstructed coordinates, all events for 2 h that are less than 0.8 m from the parent muon track are rejected.
- If tens of capture γ-rays are identified following a single muon, all events occurring in the detector for 2 h are rejected.

The explicit definitions and details of these conditions can be found is Section 4.3 of [5]. These are based in an extensive initial study performed in Sections 6 and 7 of [109].

---

[2] Although the algorithm to cluster and reconstruct the γ-ray coordinates is the same as for any other event (Sections 6.2 and 6.3, respectively), the algorithm's performance is considerably different than for non-cosmogenic events, due to the electronic noise and board saturation following the muon. In Section III and Section V of [66], n capture γ-ray identification and position reconstruction are characterized, respectively.

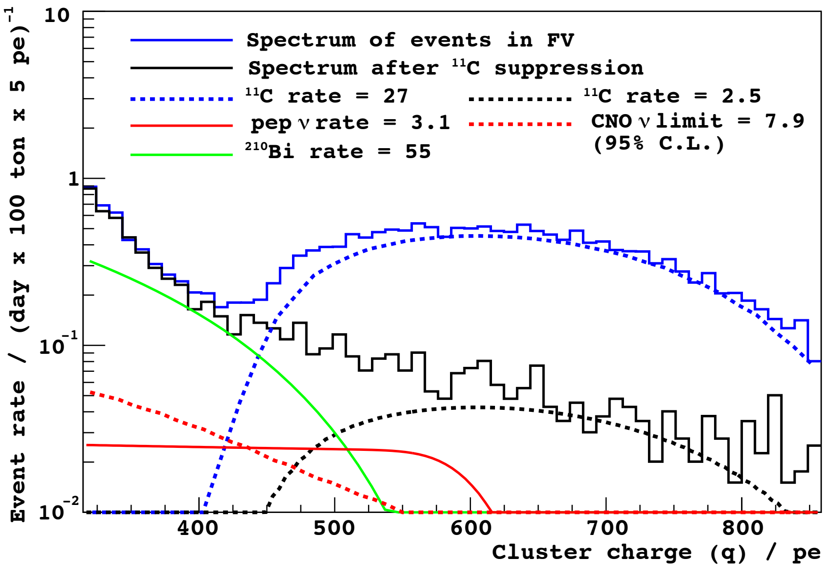

Figure 7.3: The effect of ^{11}C suppression on the charge spectrum in the region near the shoulder of the e^- recoil spectrum from *pep* ν. The data spectra (solid black and blue lines) have been normalized by the exposure. For reference, the spectra of the dominant species in the region, convolved with the detector's charge response (Section 8.2.1), are shown at characteristic values [1] (in units of day^{-1}(100 ton)$^{-1}$).

The loss of exposure from these vetoes is estimated by generating uniformly distributed fake events throughout the data set and counting what fraction of them are rejected. The reduction in the ^{11}C decay rate can be estimated from the count rate in the 600–700 pe range, where mostly ^{11}C decays are expected.

The residual exposure and ^{11}C rate for different veto configurations and FVs were calculated. The final configuration was chosen based on a Monte Carlo study of the expected statistical uncertainty in the extracted *pep* ν signal as a function of these parameters (Figure 5 in [5]). The effect of this procedure on the cluster q spectrum, along with the other event selection cuts, is shown in Figure 7.2

As the veto criteria are uncorrelated to the energy of the ^{11}C decays and the rate of solar ν interactions, no systematic uncertainties are introduced by this procedure.

The final veto criteria lead to a sample of events with a ^{11}C rate <10% of the original (Figure 7.3) and a residual exposure of 48%, corresponding to 20410^{+220}_{-150} day×ton.

The rejected events (22370^{+250}_{-170} day×ton of exposure) are also kept to generate a "^{11}C-enhanced" spectrum, which is also considered for the signal extraction (Chapter 8).

Chapter 8

Signal Extraction

From the sample of interactions with an enhanced solar ν signal (Chapter 7) whose physical properties are well characterized (Chapter 6), we may extract the interaction rates of the solar ν species.

8.1 α subtraction

In order to simplify the signal extraction, we have removed the contribution from α decays to the energy spectrum so that it is not necessary to consider them in the fit. Due to the prominence of ^{210}Po decays in the spectrum (Figure 7.2), a selection cut on the Gatti parameter (Section 6.4.1) is not sufficient.

For this purpose we have developed a statistical technique, where for candidate events within a particular q range (bin), we perform a series of fits to the distribution of the Gatti parameter (G) to two Gaussian functions[1]. As a first step we leave the means, variances and integrals of the Gaussians free in the fit (Figure 8.1). Unfortunately, we have found that the best-fit parameters are biased (i.e. different from the

---

[1] Note that in Figure 6.5 the G distribution of es is skewed. This is mostly due to the broad range of energies of ^{214}Bi decays and the dependence of G on the event energy (Figure 6.6 in [11]). The bias in estimating the number of events from a Gaussian fit to a non-Gaussian G distribution was found to be negligible in Section 6.4.1.1 of [11].

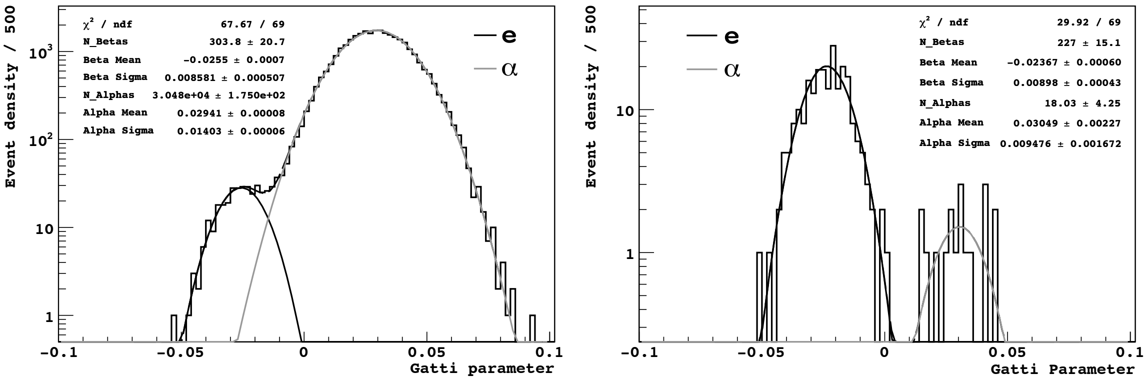

Figure 8.1: G distributions of events that satisfy all selection criteria (Chapter 7) in two q ranges: 200–205 pe (left) and 290–295 pe (right). The distributions have been fit to the addition of two Gaussian functions, the best-fit values for the means, variances and integrals of the Gaussians are shown in the legends.

true values of the distributions) when the fraction of es in the G distribution is <0.3 and that the bias in the integral decreases if the mean of the Gaussian is fixed to its true value (Figure 6.12 in [11]). Therefore, for q regions where the e fraction is <0.3, we fix the mean of the Gaussians to the result obtained from a linear interpolation between regions where the fit is expected to perform well (Figure 6.7 in [11]). Finally, we perform a Monte Carlo study to evaluate any remaining bias in the integrals of the best-fit functions, assuming the interpolated means and variances and the returned numbers of αs and es in the previous step. More details may be found in Section 6.4 of [11].

From the integrals of the best-fit distributions and the estimated bias, we obtain the number of αs and es (and the uncertainties) in the corresponding bin. This procedure is repeated in 5 pe bins below 400 pe[2]. The content of the bin is then updated with the number of es to obtain the e recoil spectrum (Figure 8.2).

---

[2] The implementation of the multivariate fit (Section 8.4) formally requires that the bin contents remain unchanged for the q ranges where the PS-BDT and spatial distributions are considered. In any case, the only αs with energies beyond this point (E_α>7.4 MeV) are those from the decays of ^{212}Po and ^{214}Po, which should be effectively removed by the selection cuts (Section 7.1) due to their coincidence in time with ^{212}Bi and ^{214}Bi, respectively (Table 5.3). Figure 6.8 in [11] shows the negligible effect of the procedure for q>400 pe.

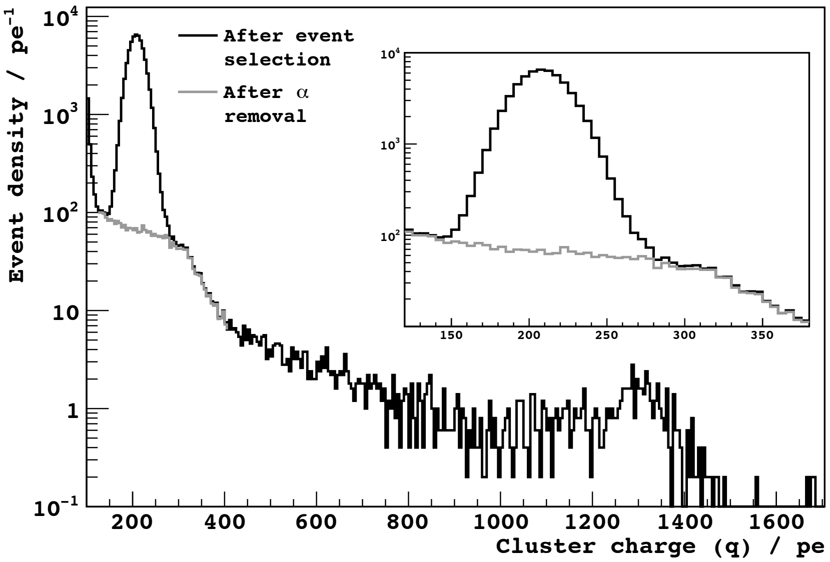

Figure 8.2: Charge spectrum of events that pass all selection cuts before and after the expected contribution from α decays in every bin is removed by the statistical procedure outlined in Section 8.1. The resulting e recoil spectrum is the one considered for the extraction of the solar ν signal.

8.2 Probability density functions

To best disentangle the solar ν signal from radioactive backgrounds we will perform a fit to the distributions of the candidate events in three parameter spaces: i) the cluster charge, related to the kinetic energy of the e recoils (Section 6.5), ii) the reconstructed distance from the center of the active target (Section 6.3), and iii) the e^-/e^+ discrimination (PS-BDT) parameter (Section 6.4.2). For this, we need to construct accurate probability density functions (PDFs) for each parameter space.

8.2.1 Cluster charge distributions

Following Equation 6.14, the mean of the response from a mono-energetic line for the full exposure is

$$\langle q\rangle(E) = \langle L_{\mathrm{pe}}\rangle \times Q_{\mathrm{eff}}(E,0,0) \times E \qquad (8.1)$$

where L_{pe} is simply averaged over the exposure and we will ignore that Q_{eff} is slightly dependent on the event coordinates (Figure 6.10)[3].

As shown in Section 6.5, the produced number of photoelectrons by a PMT for a mono-energetic source at a particular point in the active target is very well approximated by a Poisson distribution. Yet the distribution of the measured charge variable (q) of a mono-energetic source distributed throughout the fiducial exposure will deviate from this for various reasons:

- The charge output by the individual PMTs are not discrete values proportional to the number of photoelectrons, but a continuous "photoelectron response" distribution.
- q is normalized to 2000 channels, a value generally higher than the number of live channels (Figure 3.8), which also changes for every DAQ run.
- The photoelectron yield (L_{pe}) is not constant in either space or time.

All of these factors smear (i.e. increase the higher order moments of) a Poisson distribution with mean $\langle q\rangle$. To model the response of the detector to a mono-energetic source of energy E, we have opted to use an empirical formula, qualitatively similar to a Poisson distribution, with additional parameters (a and b) to match well the higher order central moments of the true response:

$$R(q,E) = \frac{1}{\sqrt{2\pi}\sqrt{\langle q\rangle(E)/a + b\,q}} \exp\left(-\frac{(q-\langle q\rangle(E)+b)^2}{2(\langle q\rangle(E)/a + b\,q)}\right) \tag{8.2}$$

By construction, the mean of this distribution is $\langle q\rangle$. Figure 5.6 in [11] shows that this function (with a and b as free parameters) matches well the energy response of Borexino's full Monte Carlo (*g4bx*), which, even though not identical to the detector's true response, it is similar enough to suggest the adequacy of the approximation.

---

[3] The effect of using a different Q_{eff} when fitting the q spectrum has been found to have a <1% effect on the extracted decay rate of the ^{7}Be ν signal and dominant backgrounds (Table 6.22 in [11], and [135]).

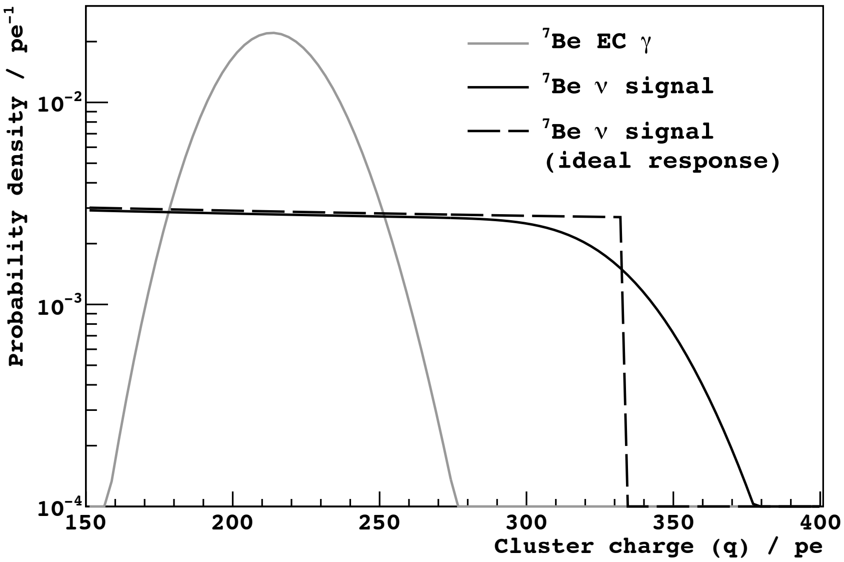

Figure 8.3: Charge (q) PDFs of the mono-energetic 0.48 MeV γ-ray from the EC decay of ^{7}Be (Table 5.5) and the e recoils from 0.86 MeV ^{7}Be νs assuming Borexino's measured energy response (black line) and an ideal response (dashed line). The spectrum from a mono-energetic line is Equation 8.2, while the e recoil spectrum from solar νs is Equation 8.3, where $P(E)$ is the energy spectrum (Figure 4.3). The ideal response is the case where $q \propto E$, i.e. $S(q) = P(L_{\text{pe}} E)$, shown to emphasize the spectral differences introduced by the detector resolution.

To quantify the effects listed above, in Section 5.5 of [11] the variance (v) and third central moment of the distribution are given in terms of the average channel normalization and in terms of the central moments of the photoelectron response and L_{pe} distributions. We expect a ∼40% larger variance than that of the Poisson distribution with the same $\langle q \rangle$ (Equation 5.134 in [11]). These expressions were particularly useful for the L_{pe} considerations taken in the definition of the FV (Section 7.2).

Using Equations 8.1 and 8.2 we can construct the q spectrum (S) of every species from the spectrum of the deposited energy (P):

$$S(q) = \int_{0}^{E_{\max}} P(E) \times R(q,E)\, dE \tag{8.3}$$

Figure 8.3 shows the effect of the detector resolution on the energy spectrum of e recoils from ^{7}Be νs.

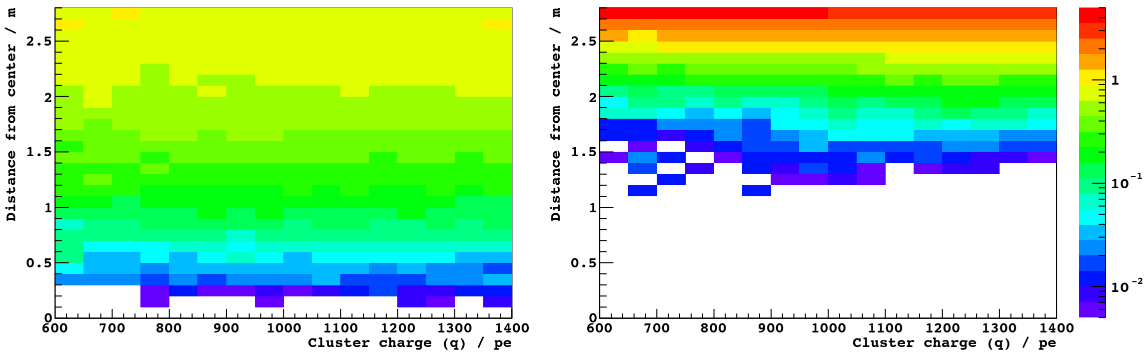

Figure 8.4: PDFs, in 14 q bins, of the reconstructed distance from the center of the active target in the FV for both uniformly distributed events (left) and γ-rays originating from the SSS (right). Each PDF was constructed with $>10^5$ *g4bx*-generated events. The color axis is the probability density in units of m^{-1}.

For the solar ν signals and radioactivity in the active target, we start from the species' known energy spectra (Table 8.1). For external γ-ray sources, we rely on the *g4bx* output from γ-rays generated on the SSS, which has been validated (Section 4.1.3 of [136]) with the use of the external ^{228}Th source (Section 3.7). In these cases, we consider the spectrum of the deposited γ-ray energy for simulated events whose coordinates are reconstructed within the FV, and proceed as for any other γ-ray source.

8.2.2 Spatial distributions

The simulated events of ^{208}Tl γ-rays from the SSS were also used to construct the PDF of the reconstructed distance from the center of the active target for external background. We have also simulated electron recoils uniformly distributed in the active target and, after all selections cuts and fiducialization, used them to construct the PDF for the solar ν signal and radioactivity in the scintillator. The external and uniformly distributed species are the only ones considered in this parameter space, and their PDFs are q dependent (Figure 8.4).

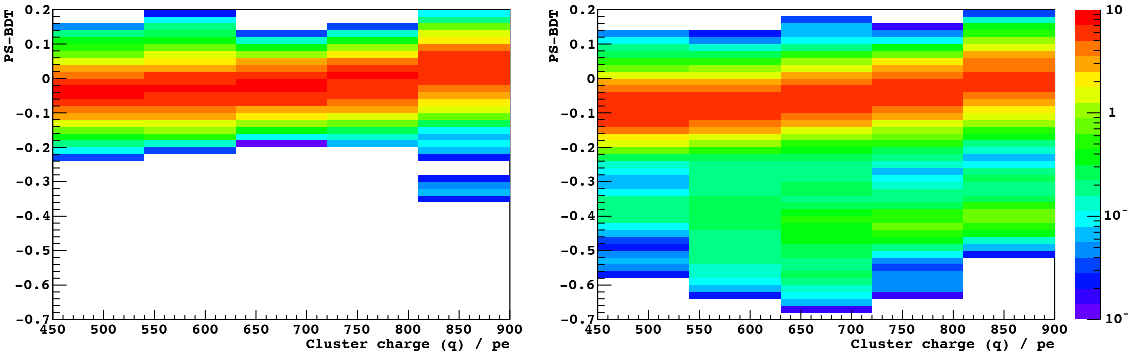

Figure 8.5: PDFs, in 6 q bins, of the e^-/e^+ discrimination parameter (PS-BDT). The e^- PDF (left) was constructed from ^{214}Bi decays, while the e^+ PDF (right) was constructed from ^{11}C decays selected by their space and time correlation with cosmogenic ns. The color axis is the probability density.

8.2.3 PS-BDT parameter distributions

Likewise, we construct two energy-dependent PDFs for the PS-BDT distributions of e^- and e^+. Even though *g4bx* can model very accurately the response of the detector in terms of energy and position reconstruction, the slight details in the scintillation time profile that lead to discrimination between e^- and e^+ are not precisely reproduced, making it impossible to reliably simulate all pulse shape parameters used in the computation of the PS-BDT. Thus, we have relied on data to construct these PDFs.

The PDFs were built with ^{214}Bi (e^-) and ^{11}C (e^+) events that were not used for the construction of the PS-BDT parameter (Section 6.4.2) so as to avoid any statistical bias. The total number of events available for each PDF is $\sim 10^3$. To artificially increase the number of events and create "smoother" PDFs, we have simulated 200 Gaussian-distributed events for every data event, using the PS-BDT value of the data event as the mean and 0.02 (i.e. the bin width of the PS-BDT PDFs) as the standard deviation. The resulting PDFs, as a function of q, are shown in Figure 8.5.

8.3 Fit configuration

To perform the multivariate fit to estimate the signal and background rates, we have included every e species (i.e. e recoils from solar νs or β decays) whose expected differential rate is not less than 5% of the total expected differential rate of e recoils from solar ν interactions (Table 8.1).

The excluded species shown in Table 8.1 are those from each background classification that have the highest interaction rates. Any other radioactive isotope from the ^{232}Th decay chain has a decay rate at most as large as ^{228}Ac, while those from the ^{235}U decay chain have decay rates that are considerably lower (Table 3 of [5]). The decay rate of the alkali metal ^{137}Cs is expected to be considerably smaller than the decay rate of ^{40}K. Except for cosmogenic ^{8}B, whose decay rate in Borexino is similar to ^{8}Li, most of the other cosmogenic species (Table 5.5) are either too short-lived (and therefore excluded by the 0.3 s after-muon cut) or their production rate is too low to lead to any significant residual decay rate (Table 4 of [5]). Untagged muons that pass the selection cuts are $<3\times10^{-4}$ day^{-1}(100 ton)$^{-1}$.

We have fixed the expected decay rate of ^{214}Pb to the measured ^{214}BiPo coincidence rate, under the assumption of secular equilibrium (Figure 5.2). The *pp* and ^{8}B ν interaction rates are fixed at the SSM + LMA-MSW predicted values. The systematic uncertainties associated with fixing the rates of these species will be evaluated in Section 9.2.

Species	$\frac{E_{\mathrm{min}}}{\mathrm{MeV}}$	$\frac{E_{\mathrm{max}}}{\mathrm{MeV}}$	Spectrum source	Particle type	Spatial distribution	Residual Differential Rate day^{-1}(100 ton)$^{-1}$ (500 pe)$^{-1}$		In the fit?
						at 330 pe	at 610 pe	
pp ν	0	0.261	e recoils [83] from	–	–	0	0	Fixed to 133
^{7}Be ν	0	0.665	ν spectra [137]	e^-	–	38±3	0	Free
pep ν	0	1.22	assuming P_{ee}	e^-	Uniform	2.18±0.03	1.37±0.02	Free
CNO νs	0	1.52	from [26, 138]	e^-	Uniform	3.5±0.5	0.45±0.07	Free
^{8}B ν	0	14.5	(Chapter 4)	e^-	Uniform	0.07±0.01	0.07±0.01	Fixed to 0.46
^{85}Kr	0	0.687	[139]	e^-	–	3.5±0.6	0	Free
^{214}Pb	0	1.02	[139]	e^-	–	2.36±0.09	0	Fixed to 1.95
^{210}Bi	0	1.16	[140]	e^-	–	>23	>0.04	Free
^{40}K	0	1.50	[141]	e^-	Uniform	–	–	Free
^{228}Ac	0.058	2.13	–	–	–	<0.08	<0.08	No
^{234m}Pa	0	2.27	[139]	e^-	Uniform	0.43±0.04	0.30±0.03	Free
^{7}Be	0.478	0.478	–	–	–	0	0	No
^{11}C	1.02	1.98	[139]	e^+	Uniform	0	47±8	Free x2
^{6}He	0	3.51	[139]	e^-	Uniform	0.10±0.02	0.15±0.02	Free x2
^{10}C	1.74	3.65	[139]	e^+	Uniform	0	0	Free x2
^{8}Li	*3*	16.0	–	–	–	0.011±0.002	0.011±0.002	No
Ext ^{40}K	0	1.46	[142, 143]	e^-	External	∼0.1	∼0.8	Free
Ext ^{60}Co	0	2.51	–	–	–	<0.02	<0.04	No
Ext ^{214}Bi	0	3.27	[142, 143]	e^-	External	∼0.2	∼2	Free
Ext ^{208}Tl	0	2.61	[142, 143]	e^-	External	∼0.08	∼0.8	Free

Table 8.1: Dominant e species in Borexino. The second and third columns give the energy range of the species. The fourth column gives the reference from where the energy spectrum was obtained. The fifth and sixth columns are the particle classification in the PS-BDT and spatial distribution parameter spaces, respectively. The expected differential rate is after all selection cuts before ^{11}C suppression (Section 7.3). The last column states whether the species interaction rate is a free parameter in the fit (or two, as is the case for species whose rates are expected to be different in the ^{11}C-suppressed and ^{11}C-enhanced q spectra), fixed to a particular value (in units of day^{-1}(100 ton)$^{-1}$) or excluded from the fit.

8.3.1 Free parameters

The interaction rates of the species are free parameters in the fit and are constrained to positive values. We consider both the q spectrum of events after ^{11}C suppression and the q spectrum of the events that were excluded by it (Section 7.3). Thus, the rates of species produced by ^{12}C spallation in the active target, whose production may be correlated with n production (Section 5.3.1), are independent free parameters in each q spectrum.

As we lack information to accurately monitor the space and time dependence of L_{pe} throughout the exposure, we introduce two free parameters: $\langle L_{\mathrm{pe}} \rangle_u$ for uniformly distributed species and $\langle L_{\mathrm{pe}} \rangle_e$ for external background. Likewise, as we do not have a perfect model of the detector's energy response, and therefore some resolution effects may remain unaccounted, a and b (Equation 8.2) are left free. The spectral feature that is most sensitive to the quenching factor (Q_{eff}) is the starting point (offset) of the ^{11}C spectrum[4]; therefore it is also a free parameter.

8.3.2 Species classification

The spatial and PS-BDT distributions of the final candidates (i.e. those that remain after ^{11}C suppression) will be considered. To construct the total PDFs in these parameter spaces given the event rates and spectra of the signal and background species, we need to assign to each species its "type" in the parameter space (i.e. uniform or external spatial distribution, and e^- or e^+ PS-BDT profile). This classification is shown in Table 8.1.

---

[4] The ^{11}C starting point also has additional uncertainties, as the e^+ annihilation in our model always assumes two 0.511 MeV γ-rays after thermalization, even though "in flight" annihilation is known to happen in a few % of the cases [144], which distorts the q spectrum due to non-linear quenching.

8.3.3 Fit range

For the extraction of the species interaction rates we will consider the q spectrum of events in the range 160–1640 pe. The lower bound is set to exclude ^{14}C pileup events (Figure 3.6 of [11]), whose q spectrum is not well known. The upper bound is set to include the full spectrum of ^{208}Tl, to better constrain the external background parameters.

The q range for which to consider the PS-BDT distributions is the range of ^{11}C decays (400–900 pe), which are used to construct the PDFs (Section 8.2.3). We will not consider the spatial distribution of events with $q<580$ pe, as it includes ^{210}Bi decays, whose spatial distribution is unknown (Section 5.1.3).

8.4 Likelihood computation

We use the method of maximum likelihood (Section 33.1.2 of [26]) for the estimation of the signal and background rates from the event distributions. We compute the likelihood (L) that the data is described by hypotheses of model parameters ($\mathbf{p}$) (i.e. the rates of the different signal and background species and the energy response parameters (Section 8.3.1)).

For every hypothesis we construct the corresponding total q PDF by adding the individual PDFs of the considered species (Section 8.2.1). The likelihood that the binned q data is described by the model is

$$L_q(\mathbf{p}) = \prod_{i=1}^{n} \begin{cases} \exp\left[-\frac{(k_i-\lambda_i(\mathbf{p}))^2}{2\sigma_i^2}\right] & \text{for} \quad q < 400 \\ \frac{a\lambda_i(\mathbf{p})^{k_i} e^{-a\lambda_i(\mathbf{p})}}{k_i!} & \text{for} \quad q > 400 \end{cases} \tag{8.4}$$

where k_i (σ_i) is the content (uncertainty) of the i^{th} data bin, n is the total number of bins considered, and λ_i is the mean value of the bin content predicted by the model (i.e. from the PDF). For $q<400$, where the bin uncertainty has been altered by the statistical α subtraction (Section 8.1), we use the Gaussian approximation to the likelihood, while for q>400, we use the standard Poisson likelihood.

Next we produce the spatial and PS-BDT distributions of the data in multiple q ranges. Using the PDFs of the particular q range (e.g. Figures 8.4 and 8.5), we construct the total hypothesis PDF according to the species event rates in the q range and their classification in the parameter space (Section 8.3.2). The likelihood for one q range in one parameter space is

$$L_p(\mathbf{p}) = \prod_{j=1}^{m} \begin{cases} \frac{a\lambda_j(\mathbf{p})^{k_j} e^{-a\lambda_j(\mathbf{p})}}{k_j!} & \text{for} \quad \lambda_j > 0 \\ \left(\frac{N}{N_{PDF}+m}\right)^{k_j} & \text{for} \quad \lambda_j = 0 \end{cases} \tag{8.5}$$

$$N = a\sum_{j=1}^{m} \lambda_j(\mathbf{p}) \tag{8.6}$$

where j labels the bins in the spatial or PS-BDT distributions (total number m). a is a scaling parameter such that the integral of the hypothesis PDF is the same as the number of events in the data distribution (N). We have redefined the likelihood of a bin where λ_j=0 in order to avoid L_p being zeroed due to an empty bin that arises from the limited statistics (N_{PDF} events) used in the construction of the PDF instead of a true zero expectation value.

The total likelihood is

$$L_T(\mathbf{p}) = \prod_{i=1}^{m_q} L_q(\mathbf{p}) \times \prod_{j=1}^{m_p} L_p(\mathbf{p}) \tag{8.7}$$

where the first product is over the q spectra (^{11}C-suppressed and ^{11}C-enhanced) and the second is over the spatial and PS-BDT distributions in every q range.

The method for computing $-\ln L_T(\mathbf{p})$ is passed to the minimization program *MINUIT* [145]. The minimum value of $-\ln L_T$ will correspond to the maximum likelihood, and is considered the "best-fit" $\mathbf{p}$.

8.5 Fit procedure

A single signal extraction to all event distributions with all parameters simultaneously free was found to be prohibitively slow, mostly due to the generation of new q PDFs in every fit iteration. Thus, we opted to perform a series of fits:

- A fit to the ^{11}C-enhanced q spectra before α subtraction (Section 8.1) to obtain the energy response parameters[5].
- A fit to all parameter spaces and q spectra after α subtraction, with all energy scale parameters except $\langle L_{\mathrm{pe}} \rangle_u$ fixed to the values from the previous fit.
- A fit to all parameter spaces and q spectra after α subtraction, with the energy response parameters fixed to the values obtained in the previous two fits.

The statistical uncertainties given for the interaction rates are those from the third fit. The uncertainties in the interaction rates associated with the uncertainties in the energy response parameters obtained from the first two fits will be treated as a systematic uncertainty (Section 9.2).

In some cases, we will perform the fit again multiple times with the interaction rates fixed to different values and use the log-likelihood ratio test (Section 8.2.3.3 of [146]) to compute the confidence levels (C.L.). Formally, that a particular set of parameter values (i.e. $\{p_i, p_j, \ldots\}$) correspond to the $x\%$ C.L. should be interpreted as

"If $\{p_i, p_j, \ldots\}$ are the true parameter values, then the probability that, when the parameters are fixed to $\{p_i, p_j, \ldots\}$, the increase (Δ) of $-\ln L$ from its best-fit (minimum) value is smaller than what is obtained is $x\%$."

---

[5] The presence of the mono-energetic line from ^{210}Po allows us to estimate the energy resolution parameters (a and b) to higher precision. A fit that also considers the α-lines simply requires their inclusion in the q PDF, as in Section 6.7.1 of [89].

For this computation we will assume that $-2\Delta \ln L$ follows a χ^2 distribution with the number of degrees of freedom equal to the number of fixed parameters[6]. The standard uncertainty returned by *MINUIT* for a parameter p_i are those corresponding to the increase in p_i from the best-fit value that leads to $-2\Delta \ln L$=1, which is the 68% C.L. upper limit (or "1-σ" uncertainty in the Gaussian approximation).

---

[6] In Section 9.2 of [5] we have performed a Monte Carlo study to validate this assumption for one fixed parameter, as well as confirming the reliability of the best-fit values returned by *MINUIT*.

Chapter 9

Results

We apply the methodology outlined in Chapter 8 to extract the interaction rates of the species included in the fit (Table 8.1).

9.1 Fit results

Table 9.1 shows the best values of all parameters estimated from the "standard" fit (Table 9.2). Figure 9.1 shows the q spectrum of the data and the q PDFs corresponding to the best-fit results. Likewise, Figure 9.2 and 9.3 show the spatial and PS-BDT parameter distributions of the final candidates, added over the considered q ranges, along with the best-fit PDFs.

The best-fit (minimum) $-\ln L$ is 1648. By performing the signal extraction on Monte Carlo-generated event distributions drawn from the best-fit PDFs, we conclude that, assuming our best-fit result as true, the probability of obtaining $-\ln L$ at least as extreme as this (i.e. the p-value) is 0.3 (Figure 27 in [5]).

Figure 9.4 shows the $-2\Delta \ln L$ contour as a function of the *pep* and CNO ν interaction rates. A similar contour as a function of the ^{210}Bi decay rate and CNO νs interaction rate, to illustrate the anti-correlation of these species, is shown in Figure 26 of [5].

Component		Fit result		Expected value	Source
a		1.112±0.043		∼1.15	Section 5.5 of [11]
b		0.624±0.035		∼0.53	Section 5.5 of [11]
$\langle L_{\mathrm{pe}}\rangle_u$		500±2 pe/MeV		492±2 pe/MeV	Section 4.3 of [89]
$\langle L_{\mathrm{pe}}\rangle_e$		$(1.0228\pm0.0096)\times\langle L_{\mathrm{pe}}\rangle_u$		$>\langle L_{\mathrm{pe}}\rangle_u$	Figure 6.11
^{11}C offset		$(0.9022\pm0.0096\,\mathrm{MeV})\times\langle L_{\mathrm{pe}}\rangle_u$		$(0.921\pm0.006\,\mathrm{MeV})\times\langle L_{\mathrm{pe}}\rangle_u$	Figure 6.10
		$\mathrm{day}^{-1}(100\,\mathrm{ton})^{-1}$		$\mathrm{day}^{-1}(100\,\mathrm{ton})^{-1}$	
^{7}Be ν (0.862 MeV)		48.2±1.9		47.6±3.4 (43.4±3.1)	Table 4.1
pep		3.36±0.57		2.80±0.04 (2.86±0.04)	Table 4.1
CNO νs		<13 (20)		5.4±0.8 (3.8±0.6)	Table 4.1
^{85}Kr		19.9±1.8		30.4±5.5	Section 5.2
^{210}Bi		53.9±2.6		>37	Figure 6.25 in [11]
^{40}K		<0.4 (0.7)		–	–
^{234m}Pa		<0.5 (0.8)		0.60±0.06	Table 5.2
^{11}C	49.91±0.65	2.48±0.16	27.3±0.3	28±5	Table 5.5
^{6}He	1.2±1.1	<0.3 (0.5)	<2	0.31±0.05	Table 5.5
^{10}C	0.92±0.45	0.18±0.07	0.57±0.27	0.53±0.04	Table 5.5
Ext ^{40}K		0.21±0.10		∼0.5	Table 5.4
Ext ^{214}Bi		0.68±0.12		∼10	Table 5.4
Ext ^{208}Tl		1.63±0.11		∼10	Table 5.4

Table 9.1: Best-fit values for all components extracted from the q, spatial and PS-BDT distributions of the data. Upper limits correspond to 95% (99%) C.L. and are given for species whose best-fit value is zero. The expected values have been compiled from the sources given in the last column. The energy response components at the beginning of the table have been defined in Section 8.2.1. All of these but $\langle L_{\mathrm{pe}}\rangle_u$ were obtained from a fit to the ^{11}C-enhanced q spectrum before α subtraction. The values for $\langle L_{\mathrm{pe}}\rangle_u$ and the species interaction rates were obtained considering all parameter spaces and q spectra (Section 8.5). The expected rates of the solar ν species are those predicted by the High (Low) Z SSM. The absence of the solar ν signal (i.e. *pep* and CNO νs interaction rates are 0) is disfavored at 99.99997% C.L., while the absence of the *pep* ν signal alone is disfavored at 98% C.L. (Figure 9.4). For the cosmogenic species we present the extracted interaction rates from the ^{11}C-enhanced spectrum, ^{11}C-suppressed spectrum and the average, respectively.

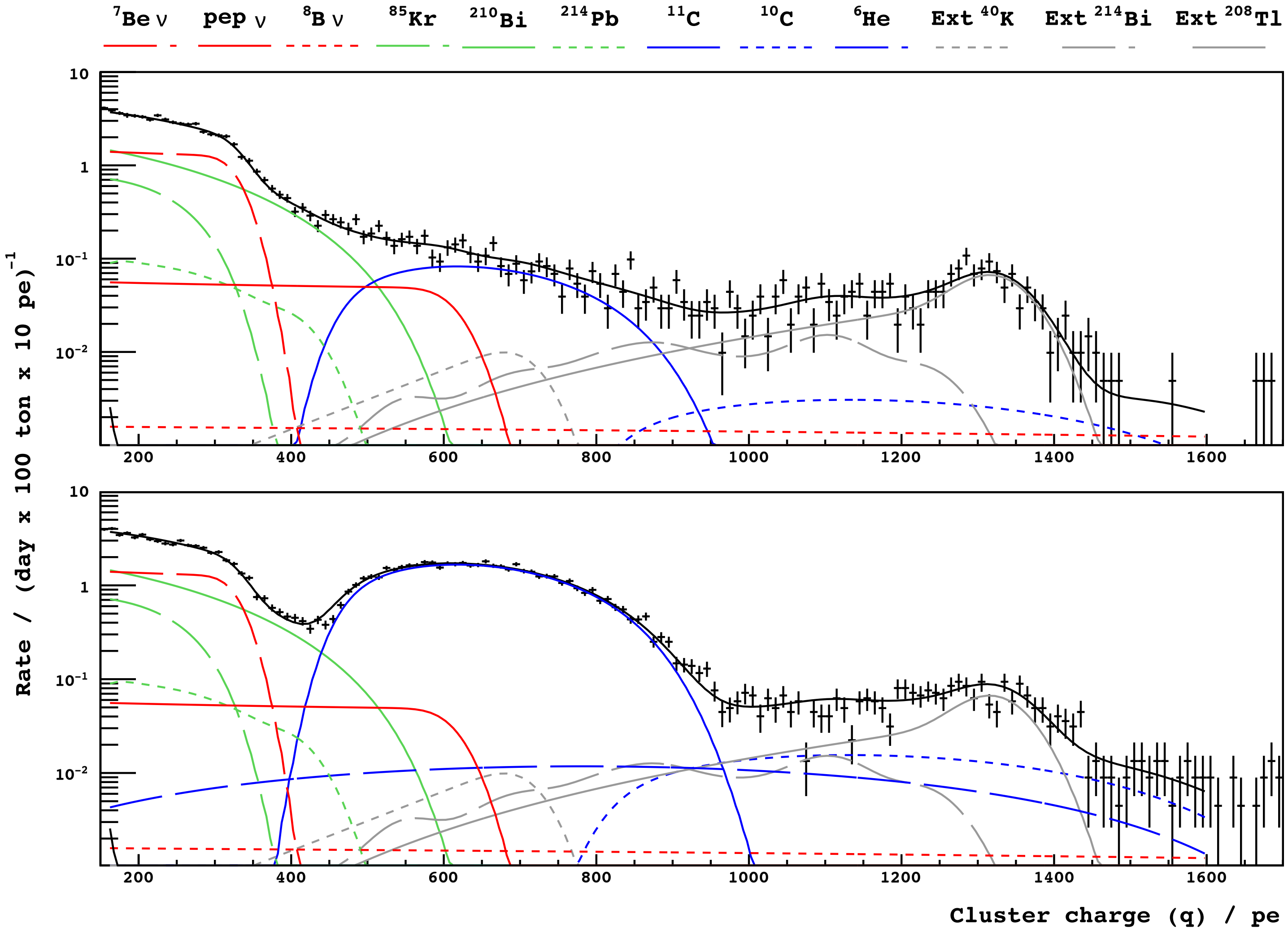

Figure 9.1: ^{11}C-supressed (top) and ^{11}C-enhanced (bottom) q spectra and the best-fit PDFs of the signal and background species.

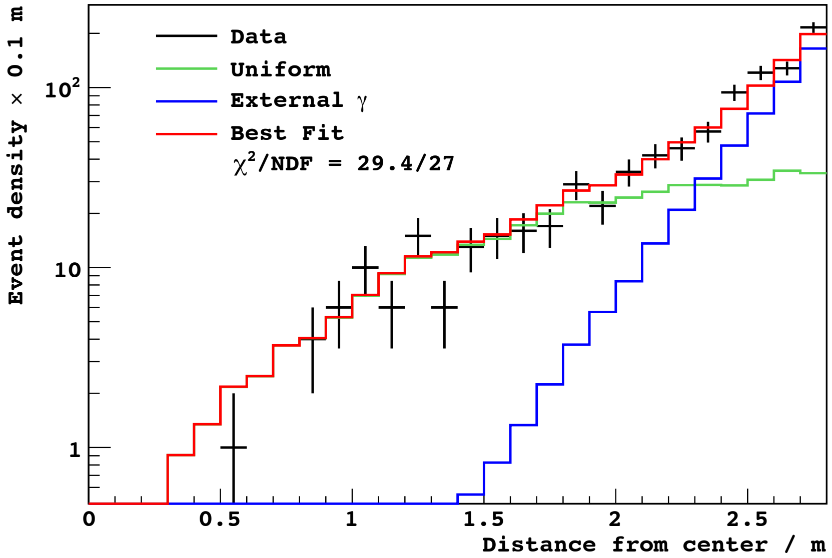

Figure 9.2: Distance from center of the active target of events in the ^{11}C-suppressed spectrum with 600<q<1400. For the q range of each set of PDFs (Figure 8.4), we integrate the contribution of uniform and external background species at their best-fit values (Figure 9.1), and construct the corresponding best-fit PDFs in this parameter space. The presented distributions are those corresponding to the addition of the resulting best-fit PDFs over all q ranges. The χ^2/NDF between the data and the best-fit total PDF is shown to illustrate the goodness of the fit, even though this is not the minimized test statistic.

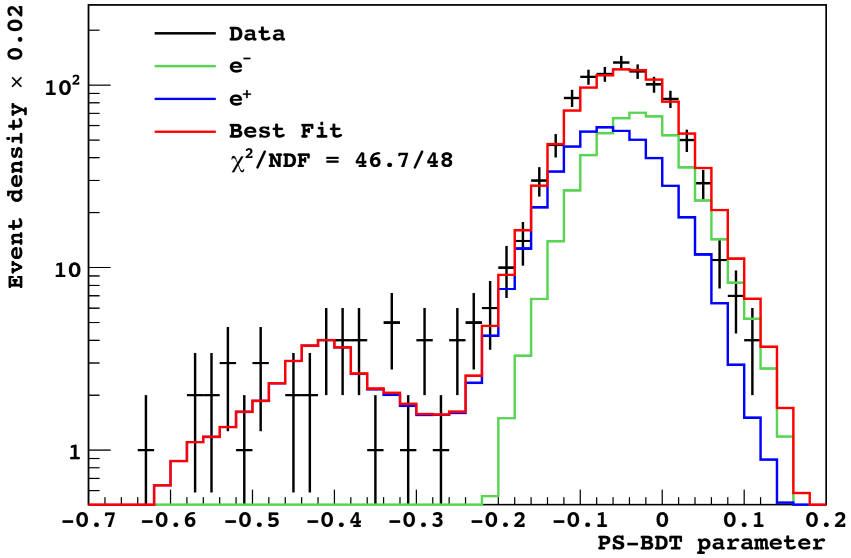

Figure 9.3: PS-BDT parameter distribution of the events in the ^{11}C-suppressed spectrum with 450<q<900. As in Figure 9.2, we construct the total best-fit PDFs from Figure 8.5, considering the rates of e^- and e^+ species in the corresponding q ranges.

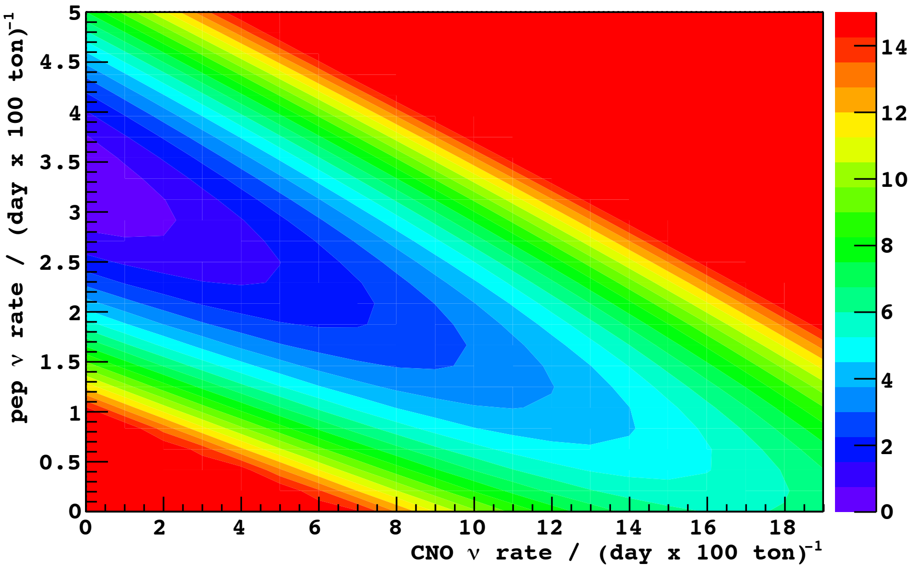

Figure 9.4: $-2\Delta \ln L$ contour (color axis), obtained from likelihood-ratio tests between the best-fit result and the result when the *pep* and CNO νs interaction rates fixed to the given values (all other species left free). We interpret this as a $\Delta\chi^2$ contour. Regions with $\Delta\chi^2 > 15$ are red.

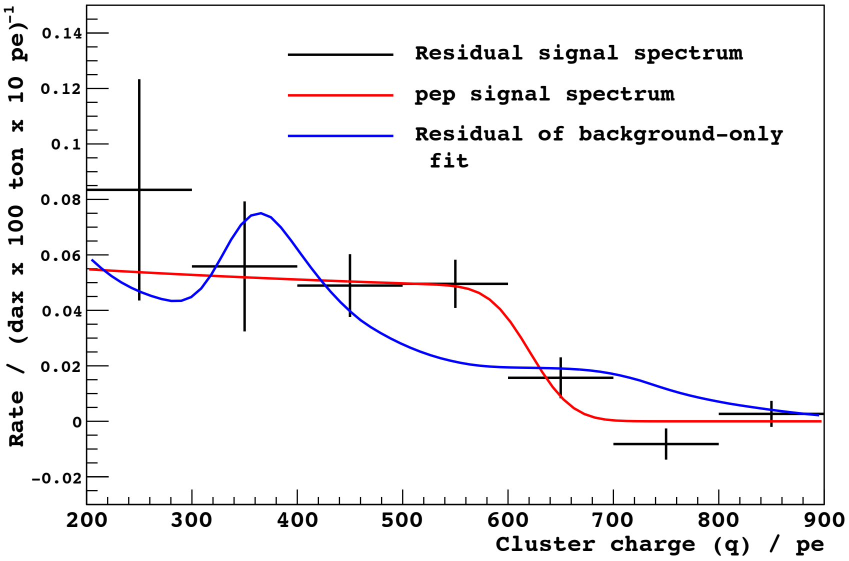

Figure 9.5: Residuals after the best-fit values of all species except the signal from *pep* and CNO solar νs are subtracted from the data energy spectrum (black). The e^- recoil spectrum from *pep* νs is shown in red. The blue line gives the difference with respect to the best-fit when no signal from *pep* or CNO solar νs is included.

Figure 9.5 shows the difference between the best-fit to data with and without the contribution from the signal of *pep* and CNO νs. Excluding the signal spectra leads to a $10\,\mathrm{day}^{-1}(100\,\mathrm{ton})^{-1}$ increase in the ^{210}Bi decay rate and a $\sim 1\,\mathrm{day}^{-1}(100\,\mathrm{ton})^{-1}$ contribution from ^{234m}Pa. The background-only hypothesis does not provide a good fit to the *pep* shoulder region.

As the *pep* solar ν interaction rate is precisely predicted by the SSM (Table 4.1), we may also compute the upper limits to the less well-known CNO ν interaction rate under the assumption that the SSM + LMA-MSW prediction of the *pep* interaction rate is true. From Figure 9.4 we obtain the 95% (99%) C.L. upper limit for the CNO νs interaction rate under this assumption to be <7.6 (10.0) $\mathrm{day}^{-1}(100\,\mathrm{ton})^{-1}$.

9.2 Systematic uncertainties

Table 9.3 summarizes the contributions to the uncertainty in the central value of the *pep* ν interaction rate and the increase in the CNO νs interaction rate upper limit by different systematic sources.

9.2.1 Energy response

We have done a scan of $\langle L_{\mathrm{pe}}\rangle_u$ about the best fit central value of 500 pe/MeV, noting the change in minimized $-\ln L$. We have kept the effective light yield of the external background species (in pe/MeV) and the offset of the ^{11}C spectrum (in pe) to their best-fit values[1]. The 1σ uncertainty in the light yield for uniform species is determined to be ± 2 pe/MeV and the associated uncertainty in the *pep* interaction rate is 1.7%.

Ignoring the difference between $\langle L_{\mathrm{pe}}\rangle$ for uniform and external background species (i.e. setting $\langle L_{\mathrm{pe}}\rangle_e = \langle L_{\mathrm{pe}}\rangle_u$), as well as slight distortions in the external background

---

[1] In this case they are not a constant fraction of $\langle L_{\mathrm{pe}}\rangle_u$, as to get a result closer to what we would expect if all energy scale parameters were free (i.e. the free parameters corresponding to $\langle L_{\mathrm{pe}}\rangle_e$ and the ^{11}C offset would be set according to the determining spectral features of the ^{11}C offset and the ^{208}Tl full-energy peak, respectively).

spectra lead to changes in the extracted *pep* ν interaction rate <1% (Section 9.4.7 of [5]).

Additionally, to evaluate the effect of the energy resolution in the *pep* interaction rate, we performed a fit with the resolution parameters set to $+2\sigma$ of the result obtained from the fit to the ^{11}C-enhanced spectrum before α subtraction (Table 9.1). The *pep* ν interaction rate increased by 0.3%.

9.2.2 Fit configuration

We have chosen a set of parameters to perform the signal extraction. Although we have justified this choice in Section 8.3, small deviations of the parameter values that are still consistent with these considerations, can lead to different results in the extracted interaction rates.

In Table 9.2 we summarize the chosen fit configuration parameters, and give other values considered. We have performed 248 fits with randomly chosen parameters from this table. All configuration options (except the ^{214}Pb rate, which is drawn from a Gaussian distribution) have equal probability to occur. We obtain a distribution of the extracted *pep* ν interaction rate, whose mean is 2.4% lower than the one from the standard fit, and an RMS that is 4.9% of the mean value.

In all these fits the best value for the CNO ν interaction rate is zero. For the case where the *pep* ν interaction rate is fixed to the SSM value, the energy scale and fit configuration uncertainties lead to a distribution of CNO central values that include results where the interaction rate is >0 and whose $\Delta\chi^2$ profiles are distributed with an RMS of $\sim$1.2 day^{-1}(100 ton)$^{-1}$ (Table 13 in [5]). Assuming that the $\Delta\chi^2$ of the CNO νs interaction rate is that of a Gaussian with mean zero (Figure 23 in [5]), the uncertainty in the fit configuration leads to a 0.36 day^{-1}(100 ton)$^{-1}$ increase in the upper limits.

Configuration parameter	Standard value	Other considered
q bin width	10	5
Fit q_{min}	160	165, 170
Fit q_{max}	1600	1560-1640
Spatial		
q range width	50	40, 70
q start	600	580-620
q end	1400	1380-1440
PS-BDT		
q range width	90	100, 120
q start	450	400
q end	900	880-900
PDF smoothing events	200	180-220
^{214}Pb rate	1.95	1.95±0.07

Table 9.2: Standard values of the fit configuration parameters and the values to which they were changed to evaluate the systematic uncertainty associated with them (Section 9.2.2). The fit to the q spectra with the standard parameters is shown in Figure 9.1. The spatial and PS-BDT configuration parameters describe the q ranges considered for the construction of the PDFs in these parameter spaces (Figures 8.4 and 8.5 show the PDFs constructed under the standard values). The "smoothing" parameter describes the factor by which the entries in the PDFs was increased following the procedure described in Section 8.2.3. To consider the uncertainty associated with fixing ^{214}Pb to its expected central value, we also perform fits with the ^{214}Pb rate fixed to values drawn from a Gaussian distribution whose σ is the uncertainty in the ^{214}Pb rate.

9.2.3 γ-rays in the PS-BDT distributions

Even though γ-rays are considered e^- species in the PS-BDT parameter space, their distributions may be different than those from recoil e^- due to the diffuse spatial topology of the energy deposits. Considering the PS-BDT parameter space with $q<700$ pe ($\sim$1.4 MeV) excludes most of the γ-rays from the e^- fitting PDF (Figure 5.3) and the candidate event distributions. Under this condition, the fit returns a *pep* ν interaction rate that is 2.7% higher than the standard result.

9.2.4 Statistical uncertainties in PS-BDT PDFs

Due to the low number of events used to construct the PS-BDT PDFs (Section 8.2.3), there may be significant differences between those used in the fit and the true e^- and e^+ PDFs.

We have performed 100 fits starting from e^- and e^+ PDFs whose bin content has been changed according to Poisson statistics, using the original bin content as the expected value. The generated PDFs are among them as different as the data is from the true PDFs. From the resulting distribution of the *pep* ν interaction rates, we obtain a 5% uncertainty (1-σ) due to the use of the approximate PDF.

9.2.5 Exclusion of period 8

Data period 8 (Table 7.1), which accounts for ∼10% of the exposure, has been excluded from other analyses due to anomalous fit results supposedly due to changes in the electronics firmware and the filling of the detector with pure PC, whose optical properties are different than the scintillator (Section 6.8.1.1 of [11]). Performing a fit to the data excluding period 8 leads to a decrease in the ^{7}Be ν rate of 4% to $46\pm2\,\text{day}^{-1}(100\,\text{ton})^{-1}$, similar to what is observed in the dedicated ^{7}Be ν analysis (Table 6.17 of [11]). The effect on the *pep* ν interaction rate is smaller, with a 1% increase.

9.2.6 SSM uncertainties of the fixed solar ν species

In our fit, the *pp* and ^{8}B ν signals are fixed to the SSM predicted rates (Table 8.1). T_{max} of e recoils from *pp* ν (Table 4.1) is lower than q_{min} ($160\,\text{pe} \approx 0.35\,\text{MeV}$), and it offers an almost negligible contribution in the considered q range (the neglected black line in the bottom left of Figure 9.1 is the expected *pp* neutrino signal). Fixing the ^{8}B ν signal to $\pm2\sigma_{\text{SSM}}$ changes the central value for the *pep* ν interaction rate by $\mp1\%$.

Source	Δ *pep* mean /%	Contribution to *pep* σ / %	Δ CNO limit day^{-1}(100 ton)$^{-1}$
Fiducial exposure	-0.3	0.9	–
Energy response	0	1.7	} 0.36
Fit configuration	-2.4	4.9	
γ-rays in PS-BDT distributions	+1.4	2.3	–
Few statistics in PS-BDT PDFs	0	5	–
Exclusion of minor backgrounds	-1.2	2.0	–
Total systematic uncertainty	-2.5	7.9	0.70

Table 9.3: Systematic uncertainties and their contribution to the *pep* ν signal uncertainty and the CNO ν signal upper limit (95% C.L.) for the case where the *pep* ν signal is fixed to the SSM + LMA-MSW predicted value. For the evaluation of the uncertainty in the *pep* ν signal associated with the presence of γ-rays in the PS-BDT distributions and the exclusion of minor backgrounds, we have taken the results from the corresponding checks (Section 9.2.3 and 9.2.7, respectively) as a 1-σ uncertainty. Uncertainties have been symmetrized following the prescription given in Equation 27 of [147]. To obtain the total increase in the CNO ν limit, we have assumed that the contribution by the sources that have not been evaluated is the same as for those that have been (this is the case for the *pep* ν signal).

9.2.7 Exclusion of other background species

^{228}Ac and ^{212}Pb (another β^- ^{232}Th daughter, Q=0.57 MeV) are the species that were not included in the fit that have the highest expected interaction rates (Table 8.1), at the level of the ^{8}B ν signal. The best value for ^{228}Ac when included in the fit is zero, and its inclusion does not affect the returned central value or uncertainty of the *pep* ν signal. Fixing ^{228}Ac at its expected upper limit, leads to a 2.3% decrease in the *pep* ν interaction rate.

9.3 Implications

Using the best estimates of the *pep* and CNO solar ν interaction rates, we can compute the solar ν fluxes (Table 9.4), under the standard LMA-MSW solution of solar neutrino oscillations (Section 2.2.1). These results are consistent with the expectations of the SSMs.

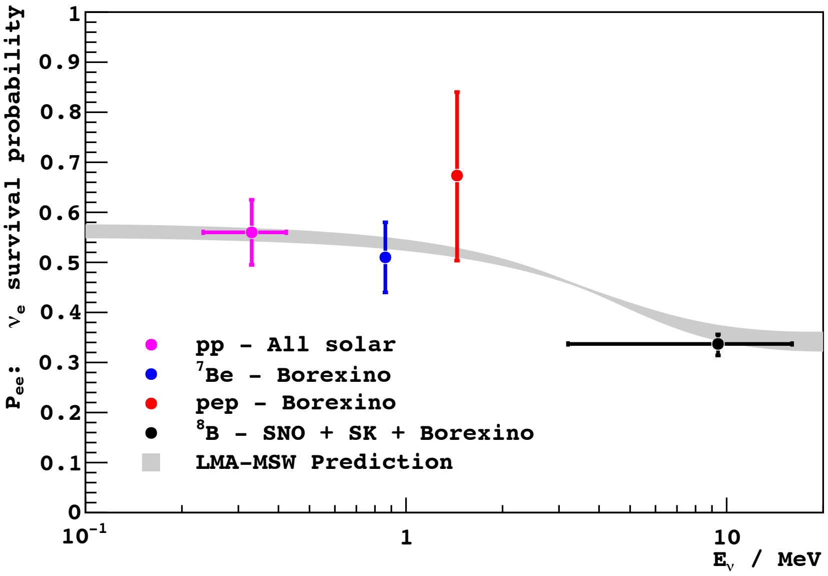

Figure 9.6: P_{ee} value obtained from the measured *pep* ν interaction rate (Table 9.4). Values from other solar ν interaction rate measurements [33] are shown for completeness.

ν	Interaction rate	Solar-ν flux	Data/SSM ratio	
	$\text{day}^{-1}(100\,\text{ton})^{-1}$	$10^8\,\text{cm}^{-2}\,\text{s}^{-1}$	High Z	Low Z
pep	$3.28 \pm 0.56_{\text{stat}} \pm 0.26_{\text{syst}}$	1.7 ± 0.3	1.2 ± 0.2	1.2±0.2
CNO	< 8.3 ($< 7.6_{\text{stat only}}$)	< 7.9	< 1.5	< 2.1

Table 9.4: The *pep* and CNO solar ν interaction rates. To obtain the ν fluxes we have assumed the LMA-MSW solution to solar ν oscillations. For the CNO ν upper limit (95% C.L.), we have fixed the *pep* ν interaction rate at the SSM prediction. In the results in the last two columns, both statistical and systematic uncertainties are considered. The last column gives the ratio between our measurement and the SSMs (Table 2.2).

Under the assumption of no ν flavor oscillations, the expected *pep* ν interaction rate given the SSM flux is 4.47±0.05 $\text{day}^{-1}(100\,\text{ton})^{-1}$. Our result corresponds to P_{ee}=0.67±0.17 and disfavors the no oscillation hypothesis at 97% C.L. Figure 9.6 shows this result alongside the best estimates of P_{ee} from other solar ν interaction rate measurements.

Chapter 10

Conclusion

The results given in Table 9.1 are generally in agreement with expectations. The discrepancies in the q resolution and $\langle L_{\mathrm{pe}} \rangle$ were expected due to our ignorance of certain details of the detector. The result for the ^{11}C offset, as a fraction of $\langle L_{\mathrm{pe}} \rangle_u$, is $<2\,\sigma$ from the prediction of our quenching model (Section 6.5), suggesting the adequacy of our approximation that the start of the ^{11}C spectrum is the quenched energy of two 0.511 MeV γ-rays.

The measured interaction rates of the cosmogenic isotopes are in agreement with the extrapolated values from KamLAND data (Table 5.5), further confirming the scaling rule proposed in [90]. The measured ^{10}C interaction rate is consistent with the one obtained from a time-after-muon analysis carried out in the context of the ^{8}B ν analysis ($0.62 \pm 0.11\,\mathrm{day}^{-1}(100\,\mathrm{ton})^{-1}$ [90]).

The results for the interaction rates from the external γ-rays in the active target are $\sim$10 times lower than expected. Both Figures 9.1 and 9.2 show that our measured values are in good agreement with the data, and suggest that the expected values are overestimated. This may be best explained by experimental conservatism in the estimation of the radioactive contamination of the peripheral materials.

The obtained upper limit on ^{40}K is the best estimate of its contamination in the active target. At $<5\times10^{-11}\,\mathrm{Bq\,kg^{-1}}$, the ^{40}K contamination in Borexino is at most $\sim10^{-13}$ of the decay rate in the Earth's crust. Yet another demonstration of Borexino's success in the reduction of radioactive backgrounds.

Although there is a $<2\,\sigma$ discrepancy between the measured ^{85}Kr value and the expected value from the rate of ^{85}Kr-^{85m}Rb coincidences, our result is considerably lower ($\sim$6–9 $\mathrm{day^{-1}(100\,ton)^{-1}}$) than the one obtained in the ^{7}Be ν analysis (Table 6.15 in [11]). This is partly due to the inclusion of period 8 in our analysis and the fact that our central value corresponds to a CNO νs interaction rate of zero, while in the ^{7}Be ν analysis this value was fixed at the High Z SSM prediction. Performing our fit without period 8 leads to a ^{85}Kr value that is $2.5\,\mathrm{day^{-1}(100\,ton)^{-1}}$ higher, while fixing the CNO νs interaction rate at the High Z SSM value increases the ^{85}Kr decay rate by $1.5\,\mathrm{day^{-1}(100\,ton)^{-1}}$. We also note that the fiducial volumes of the two analyses are not exactly the same, and therefore there is only some statistical correlation between the results. Therefore, even though the discrepancy is not entirely understood, the difference might lie in the fit configuration and choice of fiducial exposure. Regardless, our value for the ^{7}Be ν interaction rate excluding period 8 ($46\pm2\,\mathrm{day^{-1}(100\,ton)^{-1}}$) is consistent with that measured by the dedicated ^{7}Be ν analysis, providing further support to the published ^{7}Be ν interaction rate result [33].

Our fit result confirms that we have been able to decrease the ^{11}C decay rate in our set of final candidate events to $9.1\pm0.6\%$ of the original rate. This has allowed us to measure, for the first time, the signal from *pep* solar νs and to place the strongest limit on the interaction rate of CNO solar νs (Table 9.4). Although our results do not have the sufficient precision to place any significant constraints on ν oscillation or standard solar models, the successful detection of a $\sim1\,\mathrm{MeV}$ e^- scattering solar ν signal at a level of $\sim2\,\mathrm{day^{-1}(100\,ton)^{-1}\,MeV^{-1}}$ ($\sim2\times10^{-8}\,\mathrm{day^{-1}kg^{-1}keV^{-1}}$) is a testament to the potential of low background detectors.

Bibliography

[1] G. Bellini et al. First evidence of pep solar neutrinos by direct detection in Borexino. *Phys.Rev.Lett.*, 108:051302, 2012.

[2] Marilyn Manson. *A Place in the Dirt.* Holy Wood. Interscope Records, 2000.

[3] Thomas Kuhn. *The structure of scientific revolutions.* University of Chicago Press, 1962.

[4] S. Davini. *Measurement of the pep and CNO solar neutrino interaction rates in Borexino.* PhD thesis, University of Genoa, 2012.

[5] pep Working Group. Measurement of the pep and CNO neutrino interaction rates in Borexino. Internal Borexino Report, April 2012.

[6] Borexino Collaboration. BOREXINO: Restricted Access Area. `https://borex.lngs.infn.it/`, June 2012.

[7] H.A. Bethe. Energy production in stars. *Phys.Rev.*, 55:434–456, 1939.

[8] Carlo Giunti and Chung W. Kim. *Fundamentals of Neutrino Physics and Astrophysics.* Oxford University Press, 2007.

[9] A.M. Serenelli, W.C. Haxton, and C. Peña-Caray. SOLAR MODELS WITH ACCRETION. I. APPLICATION TO THE SOLAR ABUNDANCE PROBLEM. *arXiv:1104.1639*, 2011.

[10] E.G. Adelberger, A.B. Balantekin, D. Bemmerer, C.A. Bertulani, J.-W. Chen, et al. Solar fusion cross sections II: the pp chain and CNO cycles. *Rev.Mod.Phys.*, 83:195, 2011.

[11] R.N. Saldanha. *Precision Measurement of the ^{7}Be Solar Neutrino Interaction Rate in Borexino*. PhD thesis, Princeton University, January 2012.

[12] F. Reines and C.L. Cowan. Detection of the free neutrino. *Phys.Rev.*, 92:830–831, 1953.

[13] Steven Weinberg. A Model of Leptons. *Phys.Rev.Lett.*, 19:1264–1266, 1967.

[14] John N. Bahcall. *Neutrino Astrophysics*. Cambridge University Press, 1989.

[15] L.C. Stonehill, J.A. Formaggio, and R.G.H. Robertson. Solar neutrinos from CNO electron capture. *Phys.Rev.*, C69:015801, 2004.

[16] Martin Asplund, Nicolas Grevesse, A. Jacques Sauval, and Pat Scott. The chemical composition of the Sun. *Ann.Rev.Astron.Astrophys.*, 47:481–522, 2009.

[17] S. Basu. The Solar Metallicity Problem: What is the Solution? In M. Dikpati, T. Arentoft, I. González Hernández, C. Lindsey, and F. Hill, editors, *Solar-Stellar Dynamos as Revealed by Helio- and Asteroseismology: GONG 2008/SOHO 21*, volume 416 of *Astronomical Society of the Pacific Conference Series*, page 193, December 2009.

[18] N. Grevesse and A. J. Sauval. Standard Solar Composition. *SpaceSci.Rev.*, 85:161–174, May 1998.

[19] John N. Bahcall, Aldo M. Serenelli, and Sarbani Basu. 10,000 standard solar models: a Monte Carlo simulation. *Astrophys.J.Suppl.*, 165:400–431, 2006.

[20] E. Komatsu et al. Seven-Year Wilkinson Microwave Anisotropy Probe (WMAP) Observations: Cosmological Interpretation. *Astrophys.J.Suppl.*, 192:18, 2011.

[21] Samoil M. Bilenky and B. Pontecorvo. Lepton Mixing and Neutrino Oscillations. *Phys. Rept.*, 41:225–261, 1978.

[22] John N. Bahcall and Steven C. Frautschi. Lepton non-conservation and solar neutrinos. *Phys.Lett.*, B29:623–625, 1969.

[23] S. P. Mikheyev and A. Y. Smirnov. Resonance enhancement of oscillations in matter and solar neutrino spectroscopy. *Yadernaya Fizika*, 42:1441–1448, 1985.

[24] L. Wolfenstein. Neutrino Oscillations in Matter. *Phys.Rev.*, D17:2369–2374, 1978.

[25] Samoil M. Bilenky. *Introduction to the Physics of Massive and Mixed Neutrinos, Lect. Notes Phys. 817.* Springer, Berlin Heidelberg, 2010.

[26] K. Nakamura et al. Review of particle physics. *J.Phys.G*, G37:075021, 2010.

[27] F.P. An et al. Observation of electron-antineutrino disappearance at Daya Bay. *Phys.Rev.Lett.*, 108:171803, 2012.

[28] John N. Bahcall and Carlos Pena-Garay. Solar models and solar neutrino oscillations. *New J.Phys.*, 6:63, 2004.

[29] Alexander Friedland, Cecilia Lunardini, and Carlos Pena-Garay. Solar neutrinos as probes of neutrino matter interactions. *Phys.Lett.*, B594:347, 2004.

[30] B. Aharmim et al. Combined Analysis of all Three Phases of Solar Neutrino Data from the Sudbury Neutrino Observatory. *arXiv:1109.0763*, 2011.

[31] K. Abe et al. Solar neutrino results in Super-Kamiokande-III. *Phys.Rev.D*, 83:052010, 2011.

[32] S. Abe et al. Precision Measurement of Neutrino Oscillation Parameters with KamLAND. *Phys.Rev.Lett.*, 100:221803, 2008.

[33] G. Bellini, J. Benziger, D. Bick, S. Bonetti, G. Bonfini, et al. Precision measurement of the ^{7}Be solar neutrino interaction rate in Borexino. *Phys.Rev.Lett.*, 107:141302, 2011.

[34] P.C. de Holanda and A. Yu. Smirnov. Homestake result, sterile neutrinos and low-energy solar neutrino experiments. *Phys.Rev.*, D69:113002, 2004.

[35] S. Davidson, C. Pena-Garay, N. Rius, and A. Santamaria. Present and future bounds on nonstandard neutrino interactions. *JHEP*, 0303:011, 2003.

[36] G. Alimonti et al. The Borexino detector at the Laboratori Nazionali del Gran Sasso. *Nucl.Instrum.Meth.*, A600:568–593, 2009.

[37] P.A. Cerenkov. Visible radiation produced by electrons moving in a medium with velocities exceeding that of light. *Phys.Rev.*, 52:378–379, 1937.

[38] G. Alimonti et al. The liquid handling systems for the Borexino solar neutrino detector. *Nucl.Instrum.Meth.*, A609:58–78, 2009.

[39] J. Benziger, L. Cadonati, F. Calaprice, M. Chen, A. Corsi, et al. The Scintillator Purification System for the Borexino Solar Neutrino Detector. *Nucl.Instrum.Meth.*, A587:277–291, 2008.

[40] Michael Leung. *The Borexino Solar Neutrino Experiment: Scintillator purification and surface contamination.* PhD thesis, Princeton University, 2006.

[41] Michael C. Johnson. *Purification and Study of Light Propagation in a Large Liquid Scintillator Detector.* PhD thesis, Princeton University, 1998.

[42] F. Elisei, F. Masetti, U. Mazzucato, F. Gatti, G. Testera, et al. Measurements of liquid scintillator properties for the Borexino detector. *Nucl.Instrum.Meth.*, A400:53–68, 1997.

[43] G. Alimonti et al. Light propagation in a large volume liquid scintillator. *Nucl.Instrum.Meth.*, A440:360–371, 2000.

[44] K.B. McCarty. *The Borexino Nylon Film and the Third Counting Test Facility.* PhD thesis, Princeton University, June 2006.

[45] A. Chavarria. The catastrophic leak. `https://argus.princeton.edu/groups/borex/wiki/6f4c0/The\_Catastrophic\_Leak.html`, September 2008.

[46] J. Maneira. On the need for a quencher in the Borexino buffer. Internal Borexino Report, September 2000.

[47] B. Caccianiga and M. Giammarchi. Measurement of the index of refraction of pure PC, PC+PPO and PC+DMP with a prism. Private communication, 1997.

[48] M. Chen, F. Elisei, F. Masetti, U. Mazzucato, C. Salvo, et al. Quenching of undesired fluorescence in a liquid scintillator particle detector. *Nucl.Instrum.Meth.*, A420:189–201, 1999.

[49] S. Manecki. Volumes and leak rates. Internal Borexino Report, March 2010.

[50] G. Bellini, J. Benziger, S. Bonetti, M.Buizza Avanzini, B. Caccianiga, et al. Observation of Geo-Neutrinos. *Phys.Lett.*, B687:299–304, 2010.

[51] G. Bellini et al. Muon and Cosmogenic Neutron Detection in Borexino. *JINST*, 6:P05005, 2011.

[52] J. Maneira. *Calibration and Monitoring for the Borexino Solar Neutrino Experiment.* PhD thesis, University of Lisbon, November 2001.

[53] J. Benziger, L. Cadonati, F. Calaprice, E. de Haas, R. Fernholz, et al. The Nylon Scintillator Containment Vessels for the Borexino Solar Neutrino Experiment. *Nucl.Instrum.Meth.*, A582:509–534, 2007.

[54] J. Benziger, L. Cadonati, F. Calaprice, M. Chen, A. Corsi, et al. The fluid-filling system for the Borexino solar neutrino detector. *Nucl.Instrum.Meth.*, A608:464–474, 2009.

[55] L. Oberauer, C. Grieb, F. von Feilitzsch, and I. Manno. Light concentrators for Borexino and CTF. *Nucl.Instrum.Meth.*, A530:453–462, 2004.

[56] O.Yu. Smirnov, P. Lombardi, and G. Ranucci. Precision measurements of timing characteristics of the 8" ETL9351 series photomultiplier. *Instrum.Exp.Tech.*, 47:69–79, 2004.

[57] A. Ianni, P. Lombardi, G. Ranucci, and O. Smirnov. The Measurements of 2200 ETL9351 type photomultipliers for the Borexino experiment with the photomultiplier testing facility at LNGS. *Nucl.Instrum.Meth.*, A537:683–697, 2005.

[58] C. Arpesella et al. Measurements of extremely low radioactivity levels in BOREXINO. *Astropart.Phys.*, 18:1–25, 2002.

[59] L. Cadonati and J. Maneira. External background from the light guides. Internal Borexino Report, November 2000.

[60] V. Lagomarsino and G. Testera. The front end electronics of the Borexino experiment: description and results of the tests performed on 14 crates (2352 channels). Internal Borexino Report, March 2000.

[61] V. Lagomarsino and G. Testera. A gateless charge integrator for Borexino energy measurement. *Nucl.Instrum.Meth.*, A430:435–446, 1999.

[62] D. D'Angelo. *Towards the detection of low energy solar neutrinos in Borexino: data readout, data reconstruction and background identification.* PhD thesis, Technical University Munich, February 2006.

[63] F. Gatti, P. Musico, A. Nostro, M. Pallavicini, A. Razeto, M. Ruscitti, S. Vitale, P. Ciparelli, L. Isabella, and F. Longoni. A multi-hit and multi-event acquisition board for the Borexino experiment. 2000.

[64] B. Caccianiga et al. A multiplexed optical-fiber system for the PMT calibration of the Borexino experiment. *Nucl. Instrum. Meth.*, A496:353–361, 2003.

[65] S. Davini. Sviluppo, installazione e test di un sistema per la rivelazione di neutroni da spallazione in Borexino. Senior Thesis, University of Genoa, 2008.

[66] A. Chavarria. Neutron detection in Borexino. First year experimental project, Princeton University, November 2008.

[67] A. Chavarria et al. The Borexino Supernova Alarm System. Internal Borexino Report, February 2009.

[68] S. Hardy. *Measuring the ^{7}Be Neutrino Flux From the Sun: Calibration of the Borexino Solar Neutrino Detector*. PhD thesis, Virginia Polytechnic Institute and State University, March 2010.

[69] Henning Back. *Internal Radioactive Source Calibration of the Borexino Solar Neutrino Experiment*. PhD thesis, Virginia Polytechnic Institute and State University, September 2004.

[70] A. Derbin, Y. Suvorov, and S. Zavatarelli. The study of the registered Charge and the Gatti parameter vs the ^{241}Am-^{9}Be neutron source position. Technical report, October 2009.

[71] W. Maneschg, L. Baudis, R. Dressler, K. Eberhardt, R. Eichler, et al. Production and characterization of a custom-made ^{228}Th source with reduced neutron source strength for the Borexino experiment. *Nucl.Instrum.Meth.*, A680:161–167, 2012.

[72] W. Maneschg. *Low-energy solar neutrino spectroscopy with Borexino: Towards the detection of the solar pep and CNO neutrino flux.* PhD thesis, Ruperto-Carola University of Heidelberg, May 2011.

[73] Borexino Collaboration. Detector operations webpage. `https://bxweb.lngs.infn.it/docs/operations/operations.htm`.

[74] B.M. Loer. *Towards a Depleted Argon Time Projection Chamber WIMP Search: DarkSide Prototype Analysis and Predicted Sensitivity.* PhD thesis, Princeton University, November 2011.

[75] C. Ghiano. *Measurement of the neutrino charged-current interaction rate on* ^{13}C *in Borexino.* PhD thesis, University of L'Aquila, 2012.

[76] A. Ianni, D. Montanino, and F.L. Villante. How to observe B-8 solar neutrinos in liquid scintillator detectors. *Phys.Lett.*, B627:38–48, 2005.

[77] H.H. Chen. Direct Approach to Resolve the Solar Neutrino Problem. *Phys.Rev.Lett.*, 55:1534–1536, 1985.

[78] L. Cadonati, F.P. Calaprice, and M.C. Chen. Supernova neutrino detection in borexino. *Astropart.Phys.*, 16:361–372, 2002.

[79] Basudeb Dasgupta and John F. Beacom. Reconstruction of supernova ν_μ, ν_τ, anti-ν_μ, and anti-ν_τ neutrino spectra at scintillator detectors. *Phys.Rev.*, D83:113006, 2011.

[80] A. Chavarria. Sensitivity of Borexino to Excited Dark Matter (XDM). Internal Borexino Report, May 2009.

[81] Gerard 't Hooft. Predictions for neutrino - electron cross-sections in Weinberg's model of weak interactions. *Phys.Lett.*, B37:195, 1971.

[82] G. Bellini et al. Absence of day–night asymmetry of 862 keV ^{7}Be solar neutrino rate in Borexino and MSW oscillation parameters. *Phys.Lett.*, B707:22–26, 2012.

[83] John N. Bahcall, Marc Kamionkowski, and Alberto Sirlin. Solar neutrinos: Radiative corrections in neutrino - electron scattering experiments. *Phys. Rev.*, D51:6146–6158, 1995.

[84] John N. Bahcall. CNO solar neutrino energy spectra. `http://www.sns.ias.edu/~jnb/SNdata/cnospectra.html`, Institute for Advanced Study, Princeton, NJ, March 2012.

[85] John N. Bahcall. Neutrino-electron scattering and solar neutrino experiments. *Rev.Mod.Phys.*, 59:505, 1987.

[86] H. Minakata and C. Peña-Caray. Solar Neutrino Observables Sensitive to Matter Effects. *arXiv:1009.4869*, 2010.

[87] B. Caccianiga, A. Chavarria, D. Korablev, A. Re, O. Smirnov, Y. Suvorov, and S. Zavatarelli. Updated report on backgrounds before/after the Water Extraction (WE) purification campaings. Internal Borexino Report, January 2011.

[88] Thomas Jefferson National Accelerator Facility - Office of Science Education. The Periodic Table of Elements. `http://education.jlab.org/itselemental/index.html`, April 2012.

[89] Mach4 and LNGS. ^{7}Be Analysis. Internal Borexino Report, June 2011.

[90] A. Chavarria. Borexino's events above 3 MeV and first detection of solar ^{8}B ν-e scattering in an organic liquid scintillator target. Advanced Project, Princeton University, December 2009.

[91] M.J. Berger, J.H. Hubbell, S.M. Seltzer, J. Chang, J.S. Coursey, R. Sukumar, D.S. Zucker, and K. Olsen. XCOM: Photon Cross Section Database (version 1.5). `http://physics.nist.gov/xcom`, March 2012.

[92] Chernobyl Forum Expert Group 'Environment'. Environmental Consequences of the Chernobyl Accident and their Remediation: Twenty Years of Experience. Radiological Assessment Reports Series, International Atomic Energy Agency, 2006.

[93] E. Bellotti, G. Di Carlo, D. Di Sabatino, N. Ferrari, M. Laubenstein, L. Pandola, and C. Tomei. γ-ray spectrometry of soil samples from the Provincia dell'Aquila (Central Italy). *Applied Radiation and Isotopes*, 65(7):858 – 865, 2007.

[94] M. Laubenstein. Private Communication, March 2012.

[95] L. Wilhelmová, M. Tomášek, and K. Stukheil. The measurement of low concentration of Kr-85 in atmospheric air samples. *Biological Trace Element Research*, 43(1):725–730, 1994.

[96] M. Hirota, K. Nemoto, A. Wada, and Y. Igarashi. Spatial and Temporal Variations of Atmospheric ^{85}Kr Observed During 1995-2001 in Japan: Estimation of Atmospheric ^{85}Kr Inventory in the Northern Hemisphere. *Journal of Radiation Research (Tokyo)*, 45:405–413, 2004.

[97] S. Hardy and S. Zavatarelli. The ^{85}Kr contamination through the delayed coincidence analysis. Borexino Collaboration Meeting Presentation, June 2010.

[98] G. Zuzel, H. Simgen, and G. Heusser. Ar and Kr concentrations in nitrogen as a measure of the 39Ar and 85Kr activities in connection with the solar neutrino experiment. *Applied Radiation and Isotopes*, 61(2-3):197–201, 2004.

[99] G. Alimonti et al. Measurement of the C-14 abundance in a low-background liquid scintillator. *Phys.Lett.*, B422:349–358, 1998.

[100] G. Bonvicini, N. Harris, and V. Paolone. The chemical history of ^{14}C in deep oilfields. *arXiv:hep-ex/0308025*, 2003.

[101] S. Bonetti and L. Miramonti. Search of the 478 keV gamma peak in CTF rom the deexcitation of ^{7}Be induced by cosmic neutrons on carbon during the pseudocumene transportation. Internal Borexino Report, July 2006.

[102] R.B. Vogelaar, J. Benziger, F.P. Calaprice, and N. Darnton. Removal of cosmogenic ^{7}Be from scintillators. *Nucl.Instrum.Meth.*, A372:59–62, 1996.

[103] D.R. Tilley, J.H. Kelley, J.L. Godwin, D.J. Millener, J.E. Purcell, C.G. Sheu, and H.R. Weller. Energy levels of light nuclei A = 8, 9, 10. *Nucl.Phys.*, A745:155–362, 2004.

[104] G. Bellini et al. Cosmic-muon flux and annual modulation in Borexino at 3800 m water-equivalent depth. *arXiv:1202.6403*, 2012.

[105] M. Ambrosio et al. Measurement of the residual energy of muons in the Gran Sasso underground laboratories. *Astropart.Phys.*, 19:313–328, 2003.

[106] Donald E. Groom, Nikolai V. Mokhov, and Sergei I. Striganov. Muon stopping power and range tables 10-MeV to 100-TeV. *Atom.Data Nucl.Data Tabl.*, 78:183–356, 2001.

[107] S. Abe et al. Production of Radioactive Isotopes through Cosmic Muon Spallation in KamLAND. *Phys.Rev.*, C81:025807, 2010.

[108] P. Mosteiro. Neutron captures in the analog neutron DAQ system - A summary. Internal Borexino Report, Princeton University, 2012.

[109] R. Saldanha. Reduction of ^{11}C background in Borexino. Advanced Project, Princeton University, January 2009.

[110] M. Deutsch. Proposal for a Cosmic Ray Detection System for the Borexino Solar Neutrino Experiment. Research Proposal to NSF, Massachussetts Institute of Technology, 1996.

[111] Cristiano Galbiati, Andrea Pocar, Davide Franco, Aldo Ianni, Laura Cadonati, et al. Cosmogenic C-11 production and sensitivity of organic scintillator detectors to pep and CNO neutrinos. *Phys.Rev.*, C71:055805, 2005.

[112] A. Razeto and B.M. Loer. Precalibration and Decoding. Internal Borexino Report, 2010.

[113] Cristiano Galbiati and Kevin McCarty. Time and space reconstruction in optical, non-imaging, scintillator-based particle detectors. *Nucl.Instrum.Meth.*, A568:700–709, 2006.

[114] B. Caccianiga and Y. Koshio. Position reconstruction and determination of the fiducial volume. Internal Borexino Report, October 2010.

[115] B. Caccianiga, Y. Koshio, and S. Manecki. Estimation of the FV systematic error. Internal Borexino Report, June 2011.

[116] T. A. King and R. Voltz. The time dependence of scintillation intensity in aromatic materials. *Proceedings of the Royal Society of London. Series A, Mathematical and Physical Sciences*, 289(1418):424–439, 1966.

[117] E. Gatti and F. de Martini. A New Linear Method of Discrimination between Elementary Particles in Scintillation Counters. *Nuclear Electronics*, 2:265–276, 1962.

[118] Martin Deutsch. Evidence for the Formation of Positronium in Gases. *Phys.Rev.*, 82:455–456, 1951.

[119] Martin Deutsch. Three-Quantum Decay of Positronium. *Phys.Rev.*, 83:866–867, 1951.

[120] Y. Kino et al. Positron annihilation in liquid scintillator for electron antineutrino detection. *Journal of Nuclear and Radiochemical Sciences*, 1(2):63–68, 2000.

[121] D. Franco, G. Consolati, and D. Trezzi. Positronium signature in organic liquid scintillators for neutrino experiments. *Phys.Rev.*, C83:015504, 2011.

[122] R. Brun and F. Rademakers. ROOT: An object oriented data analysis framework. *Nucl.Instrum.Meth.*, A389:81–86, 1997.

[123] A. Hoecker, P. Speckmayer, J. Stelzer, J. Therhaag, E. von Toerne, and H. Voss. TMVA 4: Toolkit for Multivariate Data Analysis with ROOT. *arXiv:physics/0703039*, 2009.

[124] A. Chavarria. Status of the energy scale calibration. Borexino Collaboration Meeting Presentation, June 2010.

[125] J.B. Birks. Scintillations from Organic Crystals: Specific Fluorescence and Relative Response to Different Radiations. *Proc. Phys. Soc. A*, 64:874–877, October 1951.

[126] F.D. Brooks. Development of organic scintillators. *Nuclear Instruments and Methods*, 162:477 – 505, 1979.

[127] M.J. Berger, J.S. Coursey, M.A. Zucker, and J Chang. ESTAR, PSTAR and ASTAR: Computer Programs for Calculating Stopping-Power and Range Tables for Electrons, Protons, and Helium Ions (version 1.2.3). `http://physics.nist.gov/Star`, June 2011.

[128] Stephen M. Seltzer and Martin J. Berger. Evaluation of the collision stopping power of elements and compounds for electrons and positrons. *The International Journal of Applied Radiation and Isotopes*, 33(11):1189 – 1218, 1982.

[129] J. M. Los Arcos and F. Ortiz. kB: a code to determine the ionization quenching function Q(E) as a function of the kB parameter. *Computer Physics Communications*, 103:83–94, June 1997.

[130] A Grau Malonda and A Grau Carles. The ionization quench factor in liquid-scintillation counting standardizations. *Applied Radiation and Isotopes*, 51(2):183 – 188, 1999.

[131] G. Garcia, F. Blanco, A. Grau Carles, and A. Grau Malonda. Inelastic scattering and stopping power of low-energy electrons (0.01–10 keV) in toluene. *Applied Radiation and Isotopes*, 60:481–485, 2004.

[132] S. Yoshida, T. Ebihara, T. Yano, A. Kozlov, T. Kishimoto, et al. Light output response of KamLAND liquid scintillator for protons and C-12 nuclei. *Nucl.Instrum.Meth.*, A622:574–582, 2010.

[133] B. Braizinha, J.H. Esterline, H.J. Karwowski, and W. Tornow. Determination of the proton and alpha-particle light-response functions for the KamLAND, BC-501A and BC-517H liquid scintillators. *Nucl.Instrum.Meth.*, A623:1046–1049, 2010.

[134] H. Back et al. CNO and pep neutrino spectroscopy in Borexino: Measurement of the deep underground production of cosmogenic ^{11}C in organic liquid scintillator. *Phys.Rev.*, C74:045805, 2006.

[135] A. Chavarria. Quenching systematics from fit to enhanced ^{11}C spectrum. Internal Borexino Report, November 2010.

[136] Margherita Buizza Avanzini. *The ^8B Solar Neutrino Analysis in Borexino and Simulations of Muon Interaction Products in Borexino and Double Chooz*. PhD thesis, University of Milan and University of Paris Diderot (Paris 7), 2012.

[137] John N. Bahcall. Software and data for solar neutrino research. `http://www.sns.ias.edu/~jnb/SNdata/sndata.html`, Institute for Advanced Study, Princeton, NJ, March 2012.

[138] P. C. de Holanda, Wei Liao, and A. Yu. Smirnov. Toward precision measurements in solar neutrinos. *Nucl. Phys.*, B702:307–332, 2004.

[139] S.Y.F. Chu, L.P. Ekstrom, and R.B. Firestone. Database WWW Table of Radioactive Isotopes. `http://nucleardata.nuclear.lu.se/nucleardata/toi/`, February 1999.

[140] H. Daniel. Das β-Spektrum Des RaE. *Nucl.Phys.*, 31:293–307, 1962.

[141] W. H. Kelly, G. B. Beard, and R. A. Peters. The beta decay of K40. *Nuclear Physics*, 11:492 – 498, 1959.

[142] S. Agostinelli et al. GEANT4: A Simulation toolkit. *Nucl.Instrum.Meth.*, A506:250–303, 2003.

[143] GEANT4 Collaboration. Section 40: Radioactive Decay. Physics Reference Manual v9.5.0, December 2011.

[144] Michael D. Harpen. Positronium: Review of symmetry, conserved quantities and decay for the radiological physicist. *Med.Phys.*, 31:57–61, 2004.

[145] F. James and M. Roos. Minuit: A System for Function Minimization and Analysis of the Parameter Errors and Correlations. *Comput.Phys.Commun.*, 10:343–367, 1975.

[146] NIST/SEMATECH. e-Handbook of Statistical Methods. `http://www.itl.nist.gov/div898/handbook/`, June 2012.

[147] G. D'Agostini. Asymmetric Uncertainties: Sources, Treatment and Potential Dangers. *arXiv:physics/0403086*, 2004.